A study of CP violation and measurement of the CKM angle γ in $B^0 \to DK^{*0}$ decays

Hannah Pullen

Balliol College

University of Oxford

A thesis submitted for the degree of

Doctor of Philosophy

Trinity 2020

Acknowledgements

I would firstly like to thank my supervisor, Guy Wilkinson, for his guidance and wisdom throughout the past 3.5 years. In addition, the timely completion of this work would not have been possible without the help and advice I have received from Malcolm John and Sneha Malde. I am also grateful to all of my colleagues and friends at Oxford and CERN. Special thanks go to Mikkel Bjørn, without whose excellent work two chapters of this thesis would not exist, and to Sue Geddes, Kim Proudfoot, and Jennifer Matthews for keeping the particle physics department running.

I would like to extend my gratitude to the Science and Technologies Facilities Council (STFC) for funding my studies. Finally, I would like to thank my family — Esther, Sam, Benny, Poppy and Izzy — and especially my parents, Rod and Sarah, for always supporting me.

Abstract

Two measurements of *CP* observables in $B^0 \to DK^{*0}$ decays are presented, where D represents a superposition of D^0 and $\overline{D}^0$ states. The measurements use samples of proton-proton collision data collected with the LHCb detector at centre-of-mass energies of 7, 8, and 13 TeV.

The first measurement uses $5\,\text{fb}^{-1}$ of data with the D meson reconstructed in the two-body final states $K^+\pi^-$, π^+K^-, K^+K^-, and $\pi^+\pi^-$, and, for the first time, in the four-body final states $K^+\pi^-\pi^+\pi^-$, $\pi^+K^-\pi^+\pi^-$, and $\pi^+\pi^-\pi^+\pi^-$. First observations of the decays $B^0 \to D(\pi^+K^-)K^{*0}$ and $B^0 \to D(\pi^+\pi^-\pi^+\pi^-)K^{*0}$ are obtained, and a set of observables comprising yield ratios and asymmetries is studied. The second measurement studies D-meson decays to the three-body final states $K^0_S\pi^+\pi^-$ and $K^0_S K^+K^-$ in a binned Dalitz plot analysis using $9\,\text{fb}^{-1}$ of data.

The *CP* observables from both measurements are interpreted together to determine the *CP*-violating weak phase $\gamma = (77\,^{+8}_{-9})^\circ$. This is the world's most precise determination using only B^0-meson decays and is in agreement with the prediction of the Standard Model. The world's best measurements of the hadronic parameters $r_{B^0} = 0.258\,^{+0.022}_{-0.023}$ and $\delta_{B^0} = (200 \pm 8)^\circ$ are also presented.

Contents

Chapter 1

Introduction

The Standard Model is our best current attempt to describe the fundamental particles that make up the universe. In this model, there are twelve elementary "matter" particles, each of which has an "antimatter" partner with the same mass but opposite charge. An antimatter particle would annihilate with its matter counterpart in a burst of radiation if they were to meet.

While the Standard Model has stood up to rigorous testing and can make predictions with remarkable accuracy, it has a few shortcomings. It doesn't include gravity, nor does it explain the large amount of "dark matter" in the universe, which cannot be described by the twelve known particles. Another mystery is the lack of antimatter in the universe. Equal amounts of matter and antimatter should have been produced after the Big Bang and then completely annihilated, leaving the universe filled with electromagnetic radiation and little else — this clearly contradicts the world we see every day!

Physical processes that violate a certain type of symmetry, called *CP* symmetry, can cause an imbalance in the amounts of matter and antimatter in the universe. *CP*-symmetry violation means that the laws of physics in a system change if we reverse the electric charges of the particles involved and invert their positions in space. This phenomenon has been seen in the interactions of some types of heavy particles. However, the asymmetry we have observed so far is not large enough to account for the matter-antimatter imbalance in the universe, which remains an unsolved problem.

Because of these mysteries and others, particle physicists are certain that the Standard Model is incomplete — some "New Physics" beyond this model must exist, perhaps in the form of new, unobserved particles. The fact that we haven't seen these particles yet means that they are probably very heavy, so they are not produced in low-energy interactions, and unstable, so they quickly decay into more-familiar particles.

We can search for new particles in two ways. Firstly, we can try to produce them and directly observe their decays. This is challenging, as they can only be produced in a collision with an energy larger than mc^2, where m is the mass of the new particle and c is the speed of light; for charged particles, which must be produced in pairs, an energy greater than $2mc^2$ is required. We are therefore limited by the energies of the collider experiments that we have built. Extensive searches have been performed using the world's highest-energy collider, the Large Hadron Collider (LHC), which collides pairs of protons at an energy of 13 TeV. Nothing new has been found since the Higgs boson in 2012, which was the final Standard Model particle to be discovered.

There is, however, a second approach: precision measurement. Even if new particles are too heavy for us to produce, their effects can be seen at lower energies. Some particle interactions only occur when the initial and final states exchange a "virtual" particle in a loop, which exists fleetingly during the interaction and can have a mass much larger than the energies of the interacting particles. In this way, heavy particles can be involved in the lower-energy processes that we are capable of producing with current technology. The existence of these New Physics interactions could cause physical quantities, such as particle decay rates, to have different values than the Standard Model predicts. If we were to precisely measure these quantities and find a deviation from the prediction, we would have clear evidence for New Physics and some clues about its nature.

One interesting quantity that we can measure is an angle called γ, which is related to the amount of CP violation in the interactions of heavy composite particles called "B mesons". To find the Standard Model's prediction, we measure γ using processes

that *do not* involve loops and thus obey the Standard Model to a high degree of certainty, even if New Physics exists. We call this value $\gamma_{\rm SM}$, and our current best measurement is $\gamma_{\rm SM} = (72.1\,^{+5.4}_{-5.7})^\circ$ [1]. We can also calculate γ indirectly from processes that *do* involve virtual particles and could be sensitive to New Physics; our best estimate of this value is $\gamma_{\rm NP} = (65.66\,^{+0.90}_{-2.65})^\circ$ [1].

A discrepancy of the form $\gamma_{\rm SM} \neq \gamma_{\rm NP}$ would disprove the Standard Model. Although there is a difference between our current measurements, it is around the same size as the uncertainty on the value of $\gamma_{\rm SM}$. A major goal in particle physics is to reduce this uncertainty by measuring $\gamma_{\rm SM}$ with more data than ever before using a range of different particle decays. The most precise measurements come from decays of charged B^+ mesons. We can further improve the precision by studying the less-common decay of a neutral B^0 meson to a neutral charm meson (D) and an excited neutral strange meson (K^{*0}). The D meson can decay to several different combinations of lighter particles, and the method for measuring γ depends on this final state.

This thesis presents two analyses of $B^0 \to DK^{*0}$ decays using two distinct sets of D-meson final states. Chapter 2 defines the physical quantities measured and their relationships with γ. The measurements use proton-proton collision data collected with the Large Hadron Collider Beauty (LHCb) detector, which is situated at one of the collision points of the LHC and is specifically designed for detecting B-meson decays. Chapter 3 outlines the structure of the LHCb detector and describes the features that make it ideal for the measurements in this thesis.

Chapters 4 and 5 describe a study of $B^0 \to DK^{*0}$ decays with the D meson decaying to combinations of two and four particles: $K^\pm\pi^\mp$, K^+K^-, $\pi^+\pi^-$, $K^\pm\pi^\mp\pi^+\pi^-$, and $\pi^+\pi^-\pi^+\pi^-$. This work has been published in Ref. [2]. A complementary analysis with the D meson decaying to combinations of three particles, $K^0_{\rm S}\pi^+\pi^-$ and $K^0_{\rm S}K^+K^-$, is presented in Chaps. 6 and 7. The two analyses are most powerful when combined; Chap. 8 presents determinations of γ using the analyses individually and in combination. The combined results give $\gamma_{\rm SM} = (77\,^{+8}_{-9})^\circ$. This is the world's most

precise determination of γ using only the decays of neutral B mesons and will make a valuable contribution to the world average.

Chapter 2

CP violation and γ measurements

2.1 The Standard Model

The goal of particle physics is to describe the fundamental particles that make up the universe and the interactions between them. Our current best description is called the Standard Model (SM), according to which all matter is made up of the twelve point-like fermions listed in Table 2.1. Particles in the SM interact by exchanging spin-1 particles called "gauge bosons", which are listed in Table 2.2. All of the interactions in the universe can be categorised into four fundamental forces: electromagnetism, the strong nuclear force, the weak nuclear force, and gravity.

The fundamental matter particles are categorised into "leptons" and "quarks". Quarks interact via all four fundamental forces, whereas leptons do not experience

Table 2.1: The three generations of fundamental fermions in the Standard Model. For each particle, the charge Q is given in units of $e = 1.6 \times 10^{-19}$ C and the mass is given in units of GeV/c^2.

	Leptons				**Quarks**			
	Particle		Q	Mass	Particle		Q	Mass
1	Electron	e^-	-1	0.0005	Down	d	$-1/3$	0.003
	Neutrino	ν_e	0	$< 10^{-9}$	Up	u	$+2/3$	0.005
2	Muon	μ^-	-1	0.106	Strange	s	$-1/3$	0.1
	Neutrino	ν_μ	0	$< 10^{-9}$	Charm	c	$+2/3$	1.3
3	Tau	τ^-	-1	1.78	Bottom	b	$-1/3$	4.5
	Neutrino	ν_τ	0	$< 10^{-9}$	Top	t	$+2/3$	174

Table 2.2: The force-carrying gauge bosons in the Standard Model. For each particle, the mass is given in units of GeV/c^2 and the strength relative to the strong force is shown for two particles 10^{-15} m apart, which is approximately the radius of a proton.

Particle		Force	Mass	Strength
Gluon	g	Strong	0	1
Photon	γ	Electromagnetism	0	10^{-3}
W boson	$W^{\pm}$	Weak	80.4	10^{-8}
Z boson	Z^0	Weak	91.2	10^{-8}

the strong force. These categories are further split into six "flavours". The lepton flavours include the familiar electron (e^-), which has an electromagnetic charge of $-e = -1.6 \times 10^{-19}$ C. Two heavier generations of charged leptons exist, which are identical to the electron except for their larger masses: the muon (μ^-) and the tau particle (τ^-). For each charged lepton, there is a corresponding neutrally charged, almost-massless particle called a "neutrino". The quarks are also distributed across three generations with increasing mass. Each generation contains two flavours of quark: one "up-type" quark with a charge of $+\frac{2}{3}e$, and one "down-type" quark with a charge of $-\frac{1}{3}e$.

For each particle listed in Table 2.1, there exists an "antiparticle" with the same mass but opposite additive quantum numbers, including charge. The antiparticle of a charged lepton is denoted by a change of sign, such as the positron (e^+), which is the antiparticle of the electron. The antiparticle of a neutrino or quark is denoted by a bar above the particle symbol, such as $\bar{\nu}_\mu$ and $\overline{b}$.

The electromagnetic force involves the transfer of a photon, which can interact with any electromagnetically charged particle. The strong force is mediated by gluons, which can only interact with quarks and other gluons. The strong-force equivalent to electromagnetic charge is a property called "colour", which can take one of three values. Only quarks and gluons have nonzero colour, hence leptons do not interact strongly.

The nature of the strong force means that quarks are never observed as free particles and are instead confined to combinations called "hadrons". These can be

fermions — usually three-quark combinations called "baryons", such the proton (uud) and neutron (udd). Hadrons can also be bosons — usually quark-antiquark combinations called "mesons", such as the B^0 meson ($\bar{b}u$). Five-quark fermions called "pentaquarks" and four-quark bosons called "tetraquarks" have also been observed [3, 4].

The weak nuclear force is responsible for phenomena such as the beta decays of radioactive nuclei. This force is mediated by three massive bosons — the charged $W^{\pm}$ bosons and neutral Z^0 boson — and couples to all twelve fundamental fermions. The charged weak force couples together pairs of fermions that differ by one unit of electrical charge, such as (e^-, ν_e) and (u, d), and is the only known force that can change the flavour of a fermion. Although weaker than the strong and electromagnetic forces, the weak force plays an important role in the decays of hadrons containing quarks of different flavours, such as B^0 mesons, which can only decay to a lighter final state via a flavour transition.

The fourth fundamental force, gravity, is not accounted for by the SM. Gravity is incredibly weak on the length scales considered in particles physics. Nevertheless, it has a significant effect on very massive objects such as stars and planets and is responsible for the large-scale structure of the universe.

The final piece of the SM is the Higgs boson, a massive spin-0 particle that was discovered in 2012 by the ATLAS and CMS experiments at the LHC [5, 6]. This boson exists as a consequence of the Higgs mechanism, which gives the fundamental fermions and weak gauge bosons mass.

While measurements made in particle physics have so far been consistent with the SM, there are several reasons to believe that it is not the complete picture, such as its lack of a description for gravity. The SM also fails to account for cosmological observations including dark matter, dark energy, and the matter-antimatter imbalance in the universe. A major goal of particle physics is to further test the SM and search for evidence of New Physics, either by directly observing new particles or by measuring their effects on physical quantities.

2.2 The CKM matrix

The weak force couples together pairs of weak quark eigenstates: (d', u'), (s', c'), and (b', t'). This coupling allows quarks to transition between flavours within the same generation. However, the weak eigenstates q' are not identical to the mass eigenstates q that make up the physically observable hadrons. The misalignment can be absorbed entirely into the down-type quarks without loss of generality, such that $(u', c', t') = (u, c, t)$. The two sets of down-type eigenstates are then related by the Cabibbo-Kobayashi-Maskawa matrix [7, 8], V_{CKM}:

$$\begin{pmatrix} d' \\ s' \\ b' \end{pmatrix} = V_{\mathrm{CKM}} \begin{pmatrix} d \\ s \\ b \end{pmatrix} \equiv \begin{pmatrix} V_{ud} & V_{us} & V_{ub} \\ V_{cd} & V_{cs} & V_{cb} \\ V_{td} & V_{ts} & V_{tb} \end{pmatrix} \begin{pmatrix} d \\ s \\ b \end{pmatrix}. \tag{2.1}$$

A down-type mass eigenstate is therefore a superposition of all three down-type weak eigenstates, and can transition to any of the three up-type eigenstates. This means that quarks can transition from one generation to another. The probability of a transition from quark i to quark j is proportional to $|V_{ij}|^2$.

The magnitudes of the elements of the CKM matrix have been measured [1] to be

$$\begin{pmatrix} |V_{ud}| & |V_{us}| & |V_{ub}| \\ |V_{cd}| & |V_{cs}| & |V_{cb}| \\ |V_{td}| & |V_{ts}| & |V_{tb}| \end{pmatrix} = \begin{pmatrix} 0.974 & 0.225 & 0.004 \\ 0.225 & 0.974 & 0.042 \\ 0.009 & 0.041 & 0.999 \end{pmatrix}, \tag{2.2}$$

where the uncertainties, not shown, are $\mathcal{O}(10^{-3})$ or smaller. The diagonal elements are close to unity while the off-diagonal elements are small, indicating that quarks are most likely to transition within the same generation.

The CKM matrix describes the transitions of quarks, while the corresponding transitions of antiquarks are described by its complex conjugate, $V_{\mathrm{CKM}}^{\dagger}$. As these matrices may contain complex elements, $V_{\mathrm{CKM}}^{\dagger}$ is not necessarily identical to V_{CKM}. This provides a mechanism for the decay rates of particles and antiparticles to be different, a phenomenon known as "*CP* violation".

Although the CKM matrix is a 3×3 complex matrix, it can be described by just four real parameters, one of which must relate to a complex phase responsible

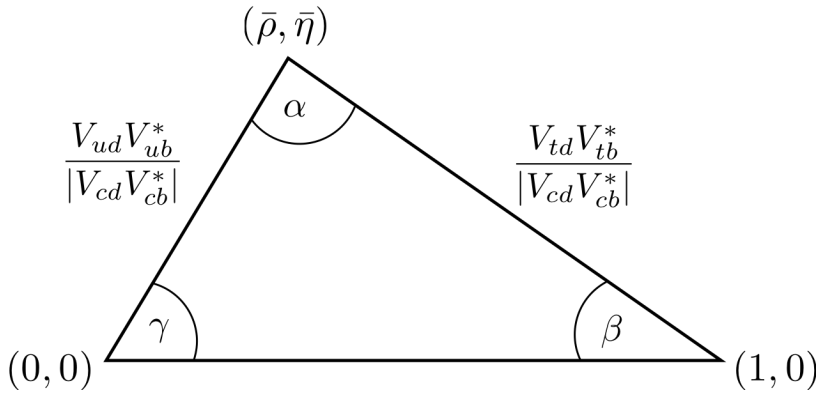

Figure 2.1: The Unitarity Triangle.

for *CP* violation. One choice of parameters is the Wolfenstein Parametrisation [9], which highlights the hierarchical structure of the elements. Each element is expanded in terms of the small parameter $\lambda = |V_{us}| \approx 0.22$ and three additional independent parameters, A, ρ, and η:

$$V_{\text{CKM}} = \begin{pmatrix} 1 - \frac{\lambda^2}{2} & \lambda & A\lambda^3(\rho - i\eta) \\ -\lambda & 1 - \frac{\lambda^2}{2} & A\lambda^2 \\ A\lambda^3(1 - \rho - i\eta) & -A\lambda^2 & 1 \end{pmatrix} + \mathcal{O}(\lambda^4). \tag{2.3}$$

Charged weak interactions are the only source of flavour-changing in the SM. This implies that the CKM matrix must be unitary, *i.e.* $V_{\text{CKM}}V_{\text{CKM}}^\dagger = \mathbb{I}$. Multiplying the matrix defined in Eq. 2.1 by its complex conjugate, we see that the unitarity condition implies nine relationships between the matrix elements, including

$$V_{ud}V_{ub}^* + V_{cd}V_{cb}^* + V_{td}V_{tb}^* = 0, \tag{2.4}$$

which can be rearranged to

$$\frac{V_{ud}V_{ub}^*}{|V_{cd}V_{cb}^*|} + 1 + \frac{V_{td}V_{tb}^*}{|V_{cd}V_{cb}^*|} = 0. \tag{2.5}$$

Each term is a complex number corresponding to a vector in the plane of $(\bar{\rho}, \bar{\eta})$, where $\bar{\rho} = \rho(1 - \lambda^2/2)$ and $\bar{\eta} = \eta(1 - \lambda^2/2)$. As the terms on the left-hand side sum to zero, they define a closed triangle in the Argand plane known as the "Unitarity Triangle", a schematic of which is shown in Fig. 2.1.

The internal angles of the triangle are labelled α, β and γ (also referred to as ϕ_2, ϕ_1 and ϕ_3), and are defined by

$$\beta = \phi_1 = \arg\left(-\frac{V_{cd}V_{cb}^*}{V_{td}V_{tb}^*}\right), \tag{2.6}$$

$$\alpha = \phi_2 = \arg\left(-\frac{V_{td}V_{tb}^*}{V_{ud}V_{ub}^*}\right), \tag{2.7}$$

$$\gamma = \phi_3 = \arg\left(-\frac{V_{ud}V_{ub}^*}{V_{cd}V_{cb}^*}\right). \tag{2.8}$$

The angles β and γ are related to the CKM elements V_{td} and V_{ub} to $\mathcal{O}(\lambda^5)$ via

$$V_{td} = |V_{td}|e^{-i\beta}, \tag{2.9}$$

$$V_{ub} = |V_{ub}|e^{-i\gamma}, \tag{2.10}$$

while α can be obtained through the relation

$$\alpha + \beta + \gamma = 180^\circ. \tag{2.11}$$

Measuring the angles and side-lengths of the Unitarity Triangle and checking them for consistency is an important test of the unitarity of V_{CKM}, and therefore of the SM.

2.3 *CP* violation

After the universe came into existence during the Big Bang, matter and antimatter should have been produced in equal quantities. However, it is apparent today that our observable universe consists mostly of matter. If any large regions of antimatter were to exist, they would emit a huge number of photons at the boundary with our matter-dominated region. As this has not been observed by astrophysicists, we conclude that the universe is dominated by matter. For a matter-antimatter asymmetry to arise from an initially symmetric state, Andrei Sakharov proposed that three conditions must be met [10]:

(i) Baryon number violation;

(ii) Violation of charge (C) symmetry and charge-parity (CP) symmetry;

(iii) Departure from thermal equilibrium.

Charge symmetry is defined by its operator $\hat{C}$, which transforms particles into their antiparticles. The parity operator $\hat{P}$ reverses the directions of the spatial axes. The combined *CP* symmetry is violated if a system changes under the application of both operators. The electromagnetic and strong forces both conserve C and P symmetry, so the weak interaction is the only area of the SM in which *CP* violation can occur.

The SM allows for baryon number violation, satisfying condition (i). Condition (iii) was satisfied as the early universe expanded and cooled. The only observed *CP* violation in the SM is in the quark sector via the complex phase of the CKM matrix, which enters the transition amplitudes of some processes. The physically observable quantity in these processes is the partial decay width, Γ. This is proportional to the square of the amplitude, and therefore only depends on the *CP*-violating phase if multiple interfering amplitudes are added together before squaring. There are three different ways in which *CP* violation can occur:

1. **Direct** *CP* violation, where the partial decay width is different for some process and its complex conjugate, *i.e.* $\Gamma(X \to Y) \neq \Gamma(\overline{X} \to \overline{Y})$;

2. *CP* violation in the **mixing** of neutral mesons, such as B^0–$\overline{B}^0$;

3. *CP* violation in the **interference** between decays to a final state f with and without mixing, such as $B^0 \to f$ and $B^0 \to \overline{B}^0 \to f$.

The first observation of *CP* violation was in the decays of neutral kaons, initially through mixing [11] and later directly [12]. In the B-meson sector, *CP* violation was first seen through interference in the decays of B^0 mesons [13, 14]. Direct *CP* violation has since been observed in decays of B^0 mesons [15, 16], B^+ mesons [17–19] and B_s^0 mesons [20]. The first observation of direct *CP* violation in the decays of charm mesons has recently been reported [21].

The size of the *CP* asymmetry seen in the quark sector is several orders of magnitude smaller than the asymmetry needed to produce the observed matter-antimatter

imbalance in the universe. The imbalance may eventually be explained by *CP* violation in the neutrino sector, where hints of a neutrino-antineutrino asymmetry have been observed [22], or in the interactions of undiscovered particles. Nevertheless, precise measurements of *CP* violation in the quark sector are an important test of the SM.

2.4 Using *CP* violation to probe the Standard Model

We can constrain the side-lengths, internal angles, and apex position of the Unitarity Triangle defined in Eq. 2.5 by studying various *CP*-violating processes. Figure 2.2 shows the current status of these measurements, with the favoured regions for different parameters indicated by coloured bands. By performing many complementary measurements, we can overconstrain the triangle and check for inconsistencies that would prove that the SM is incomplete. The measurements include:

- *CP* violation in the mixing of neutral kaons, which constrains a parameter ε_K related to the apex position;
- The oscillation frequencies Δm_d and Δm_s of B^0–$\overline{B}^0$ and B_s^0–$\overline{B}_s^0$ meson mixing, respectively, which constrain the length of the longest side;
- The amplitude of the time-dependent *CP* asymmetry in $B^0 \to J/\psi\, K_{\rm S}^0$ decays due to interference, which constrains $\sin(2\beta)$;
- Branching fractions of B-meson decays to final states that do not contain a charm quark, which constrain $|V_{ub}|$;
- Direct *CP* violation in $B^+ \to DK^+$ and similar decays, which constrains γ.

These processes can be divided into two categories: those involving tree-level decay amplitudes, and those involving suppressed amplitudes called "loops". In a tree-level decay, such as $B^+ \to DK^+$, the initial particle decays directly to the final state with no intermediate loops containing virtual particles. These processes are robust against

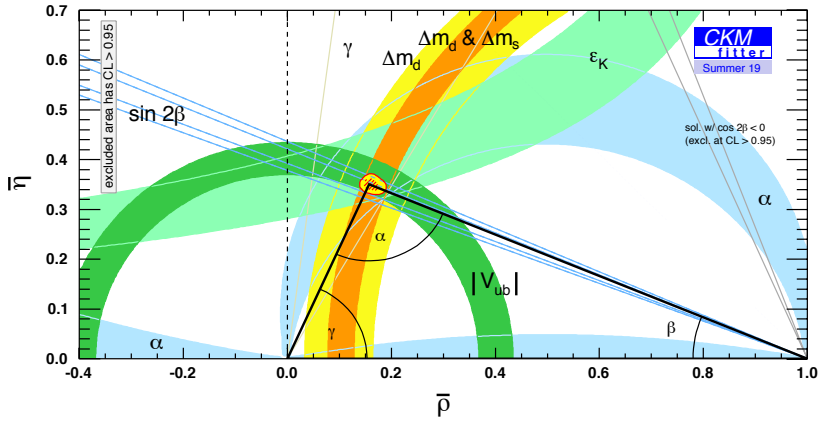

Figure 2.2: Global constraints on the Unitarity Triangle, reproduced from Ref. [1].

New Physics, as any amplitudes involving new particles would be negligible compared with the SM amplitude. Figure 2.3 shows the constraints on the Unitarity Triangle from tree-level measurements alone. The only angle that can be directly measured from tree-level decays is γ, which is therefore an important "standard candle" of the SM. The direct measurement is currently determined to be

$$\gamma_{\mathrm{SM}} = (72.1\,^{+5.4}_{-5.7})^{\circ}$$

from an average of measurements [1], the most precise ones coming from the LHCb experiment. The large uncertainty is due to the limited statistics of tree-level decays that have been measured so far.

Processes involving loops, such as neutral-meson mixing, involve virtual particles that can have masses larger than the energies of the interacting particles. Amplitudes involving undiscovered heavy particles could therefore contribute significantly to the overall amplitude of the process. Figure 2.4 shows the constraints on the Unitarity Triangle from loop-level measurements only. These constraints are used to determine an indirect measurement of γ, which is sensitive to New Physics. The current average value [1] is

$$\gamma_{\mathrm{NP}} = (65.66\,^{+0.90}_{-2.65})^{\circ},$$

which can be compared with the direct measurement to check for consistency with

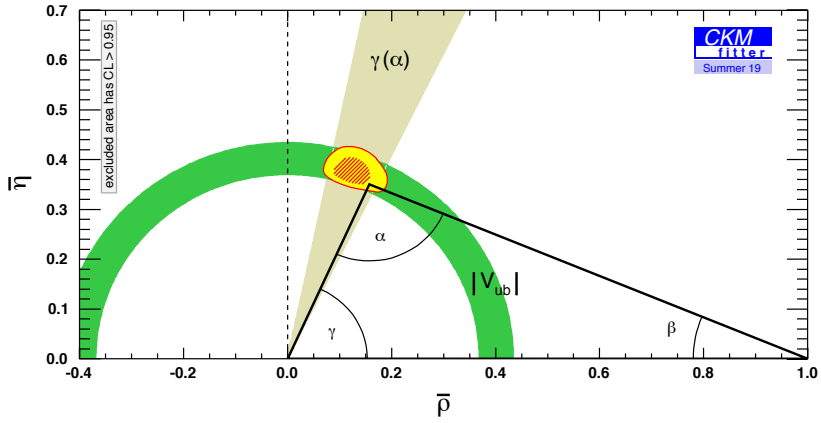

Figure 2.3: Constraints on the Unitarity Triangle using tree-level measurements only, reproduced from Ref. [1].

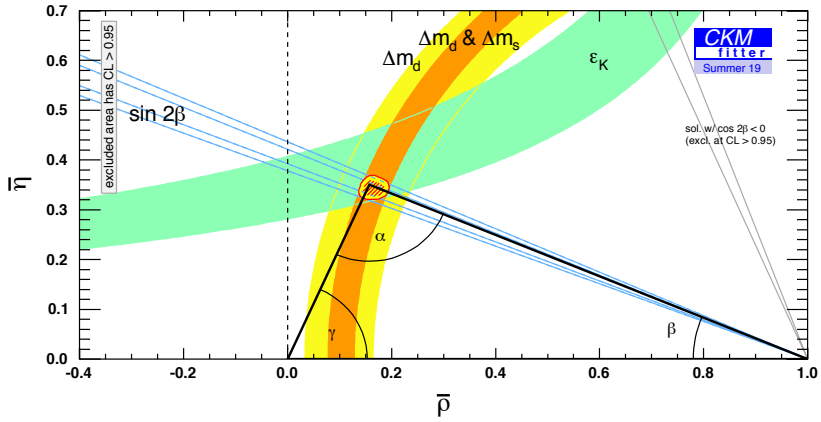

Figure 2.4: Constraints on the Unitarity Triangle using loop-level measurements only, reproduced from Ref. [1].

the SM prediction. The direct and indirect determinations are currently compatible, but the test is limited by the large uncertainty on the direct measurement. It is clear that this precision must be improved to enable a more sensitive comparison to be made.

The world-average direct measurement of γ is dominated by the LHCb experiment, which finds $\gamma = (74.0\,^{+5.0}_{-5.8})^\circ$ from studies of various B-meson decays [23,24]. Figure 2.5 shows the confidence regions of the LHCb γ measurements with different species of B meson. The combined result is dominated by measurements involving B^+ mesons, in particular the decay $B^+ \to DK^+$. The equivalent neutral-B-meson decay $B^0 \to DK^{*0}$

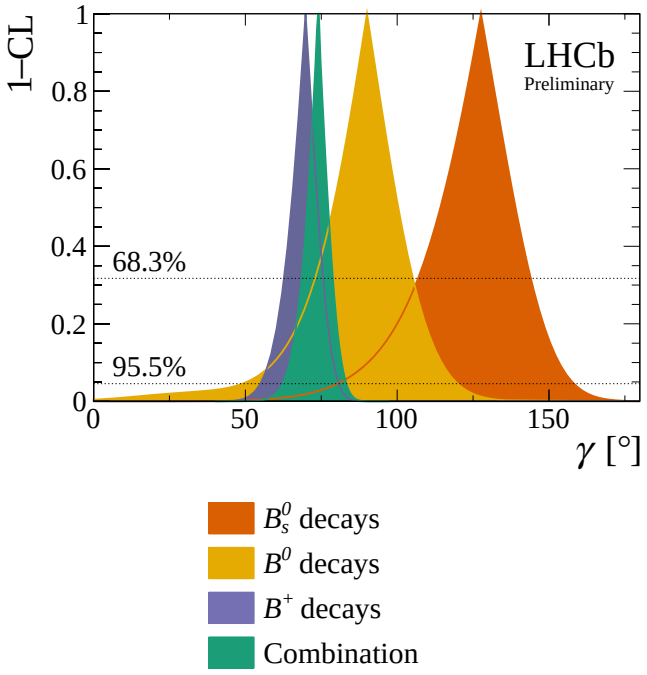

Figure 2.5: $1-\mathrm{CL}$ plots of γ measured with B-meson decays split by initial B-meson flavour: B_s^0 mesons (orange), B^0 mesons (yellow), B^+ mesons (blue), and the full combination (green), reproduced from Ref. [24].

currently has lower statistical precision, but is in fact more sensitive to γ than $B^+ \to DK^+$ as it contains a larger amount of interference through which γ can be measured. Measurements of the decays of B^0 mesons provide an important cross-check of the B^+-meson results and contribute to the overall precision. This thesis presents two such measurements.

2.5 Measuring γ with $B^0 \to DK^{*0}$ decays

Direct CP violation can be observed in decays involving a $b \to u$ transition, as their amplitudes contain a factor of $V_{ub} = |V_{ub}|e^{-i\gamma}$. Sensitivity to γ is only obtained if the amplitudes of two different transitions between the initial state and final state interfere. A suitable decay is $B^0 \to D(f)K^{*0}$, where D represents either a D^0 meson or a $\overline{D}^0$ meson decaying to a common final state f. Figure 2.6 shows Feynman diagrams of the two decays, which both occur at tree level with no intermediate loops.

The K^{*0} meson decays promptly to the final state $K^+\pi^-$ via the strong interaction.

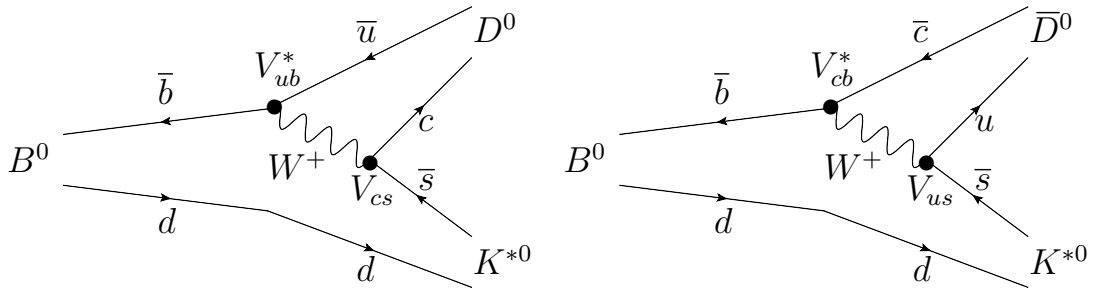

(a) $B^0 \to D^0 K^{*0}$ (b) $B^0 \to \overline{D}^0 K^{*0}$

Figure 2.6: Feynman diagrams of the decays (a) $B^0 \to D^0 K^{*0}$ and (b) $B^0 \to \overline{D}^0 K^{*0}$.

The *CP*-conjugate decay of a $\overline{B}^0$ meson produces a $\overline{K}^{*0}$ meson, which decays to the final state $K^-\pi^+$. The charge configuration of the kaon products therefore tags the flavour of the B meson at the time of decay as B^0 or $\overline{B}^0$.

The amplitude of the $B^0 \to D^0 K^{*0}$ decay contains the CKM matrix elements $V_{cs}V_{ub}^*$, whereas the amplitude of the $B^0 \to \overline{D}^0 K^{*0}$ decay contains a factor of $V_{us}V_{cb}^*$. The weak-phase difference between these amplitudes is therefore $\arg(-V_{cs}V_{ub}^*/V_{us}V_{cb}^*)$, which according to Eq. 2.8 is equal to γ to $\mathcal{O}(\lambda^5) \sim 10^{-4}$.

In addition to the weak-phase difference, the amplitudes differ by a magnitude ratio r_{B^0} and a strong-phase difference δ_{B^0}. The ratio r_{B^0} depends primarily on the ratio $|V_{cs}V_{ub}|/|V_{us}V_{cb}|$ and is approximately 0.3. As both the D meson and K^{*0} meson contain a quark from the B^0 meson, the colours of the final-state quarks are determined by the initial quarks, so both amplitudes are "colour-suppressed" by the same amount. As a result, r_{B^0} is not diluted with respect to the ratio of CKM elements by any colour-related effects. In contrast, the amplitude of a $B^+ \to \overline{D}^0 K^+$ decay is "colour-favoured", as the K^+ meson contains two new quarks, which can have any colour; it is therefore three times larger than the amplitude of a $B^+ \to D^0 K^+$ decay, which is colour-suppressed. This results in a larger overall decay rate for $B^+ \to DK^+$ decays than for $B^0 \to DK^{*0}$ decays, but a smaller value of $r_{B^+} \sim 0.1$, which diminishes the interference in $B^+ \to DK^+$ decays.

To derive the dependence of the $B^0 \to DK^{*0}$ decay rate on γ, we first consider the general case $B^0 \to DX$, where X represents any resonant or nonresonant $K^+\pi^-$

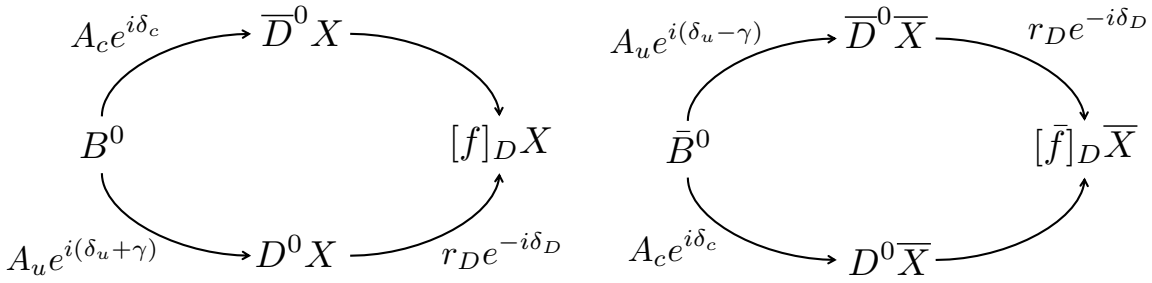

(a) $B^0 \to D(f)K^{*0}$ (b) $\overline{B}^0 \to D(\bar{f})\overline{K}^{*0}$

Figure 2.7: Interfering amplitudes in (a) $B^0 \to D(f)X$ decays and (b) $\overline{B}^0 \to D(\bar{f})\overline{X}$ decays. The relative magnitudes and phases of the intermediate amplitudes are indicated.

pair. The interfering amplitudes depend on the momentum coordinate p in $DK^+\pi^-$ phase space, and can be written as

$$A(B^0 \to \overline{D}^0 X; p) = A_c(p) e^{i\delta_c(p)}, \tag{2.12}$$

$$A(B^0 \to D^0 X; p) = A_u(p) e^{i(\delta_u(p)+\gamma)}, \tag{2.13}$$

where $A_{c(u)}$ and $\delta_{c(u)}$ are the magnitude and strong phase, respectively, for decays involving a $b \to c(u)$ quark transition. The amplitudes of the corresponding decays of $\overline{B}^0$ mesons are obtained under the transformation $\gamma \to -\gamma$, which gives

$$A(\overline{B}^0 \to D^0 \overline{X}; p) = A_c(p) e^{i\delta_c(p)}, \tag{2.14}$$

$$A(\overline{B}^0 \to \overline{D}^0 \overline{X}; p) = A_u(p) e^{i(\delta_u(p)-\gamma)}, \tag{2.15}$$

where $\overline{X}$ represents any resonant or nonresonant $K^-\pi^+$ pair.

The overall decay can proceed via a $B^0 \to D^0 X$ decay followed by a $D^0 \to f$ decay, or a $B^0 \to \overline{D}^0 X$ decay followed by a $\overline{D}^0 \to f$ decay. Figure. 2.7 shows diagrams of the two amplitudes for a $B^0 \to D(f)X$ decay and its *CP*-conjugate decay, $\overline{B}^0 \to D(\bar{f})\overline{X}$, where $\bar{f}$ is the *CP* conjugate of the final state f.

The amplitudes of the decays of D^0 and $\overline{D}^0$ mesons are related by a magnitude ratio, r_D, and a strong-phase difference, δ_D, and can be written as

$$A(\overline{D}^0 \to f) = A(D^0 \to \bar{f}) \propto 1, \tag{2.16}$$

$$A(D^0 \to f) = A(\overline{D}^0 \to \bar{f}) \propto r_D e^{-\delta_D}, \tag{2.17}$$

where small *CP*-violation effects in the D-meson system [21] are ignored.

The amplitudes of the intermediate B-meson and D-meson decays are multiplied together to give the amplitudes contributing to the overall decay. The contributing amplitudes are then added together to give the overall amplitudes:

$$A(B^0 \to D(f)X; p) \propto A_c(p)e^{i\delta_c(p)} + A_u(p)e^{i(\delta_u(p)+\gamma)}r_D e^{-i\delta_D}, \tag{2.18}$$

$$A(B^0 \to D(\bar{f})X; p) \propto A_u(p)e^{i(\delta_u(p)+\gamma)} + A_c(p)e^{i\delta_c(p)}r_D e^{-i\delta_D}, \tag{2.19}$$

$$A(\overline{B}^0 \to D(\bar{f})\overline{X}; p) \propto A_c(p)e^{i\delta_c(p)} + A_u(p)e^{i(\delta_u(p)-\gamma)}r_D e^{-i\delta_D}, \tag{2.20}$$

$$A(\overline{B}^0 \to D(f)\overline{X}; p) \propto A_u(p)e^{i(\delta_u(p)-\gamma)} + A_c(p)e^{i\delta_c(p)}r_D e^{-i\delta_D}. \tag{2.21}$$

The final state DX includes the $K^*(892)^0$ resonance we are interested in, as well as other resonant and nonresonant contributions to the $DK^+\pi^-$ final state. Although in practice we only consider decays near the mass of the K^{*0} meson, interference between the K^{*0} resonance and other contributions in this region dilutes the interference between the B-meson decay amplitudes, and hence dilutes sensitivity to γ. This dilution is quantified by a coherence factor κ, where $0 \leq \kappa \leq 1$; a value of $\kappa = 1$ would indicate a pure-$K^*(892)^0$ sample. The effective amplitude ratio r_{B^0} and strong-phase difference δ_{B^0} depend on the region of $DK^+\pi^-$ phase space sampled, and are defined by

$$r_{B^0}^2 = \frac{\int \mathrm{d}p\, A_u(p)^2}{\int \mathrm{d}p\, A_c(p)^2}, \tag{2.22}$$

$$\kappa e^{i\delta_{B^0}} = \frac{\int \mathrm{d}p\, A_c(p)A_u(p)e^{i(\delta_u(p)-\delta_c(p))}}{\sqrt{\int \mathrm{d}p\, A_c(p)^2}\sqrt{\int \mathrm{d}p\, A_u(p)^2}}, \tag{2.23}$$

where the integrals are performed over the chosen region. It is desirable to choose a region that gives a large value of κ in order to maximise sensitivity to γ.

The probability of a decay occurring depends on its partial width, Γ. Squaring the amplitudes in Eqs. 2.18–2.21 and integrating over the chosen $DK^+\pi^-$ phase space,

we obtain

$$\Gamma(B^0 \to D(f)K^{*0}) \propto 1 + r_{B^0}^2 r_D^2 + 2\kappa r_{B^0} r_D \cos(\delta_{B^0} - \delta_D + \gamma), \tag{2.24}$$

$$\Gamma(\overline{B}^0 \to D(f)\overline{K}^{*0}) \propto 1 + r_{B^0}^2 r_D^2 + 2\kappa r_{B^0} r_D \cos(\delta_{B^0} - \delta_D - \gamma), \tag{2.25}$$

$$\Gamma(B^0 \to D(\bar{f})K^{*0}) \propto r_D^2 + r_{B^0}^2 + 2\kappa r_{B^0} r_D \cos(\delta_{B^0} + \delta_D + \gamma), \tag{2.26}$$

$$\Gamma(\overline{B}^0 \to D(f)\overline{K}^{*0}) \propto r_D^2 + r_{B^0}^2 + 2\kappa r_{B^0} r_D \cos(\delta_{B^0} + \delta_D - \gamma). \tag{2.27}$$

The partial widths of pairs of *CP*-conjugate decays are different due to the different signs of γ in the interference term. The size of this term depends on the value of r_{B^0}, hence $B^0 \to DK^{*0}$ decays ($r_{B^0} \sim 0.3$) have a higher sensitivity to γ than $B^+ \to DK^+$ decays ($r_{B^+} \sim 0.1$). While our aim is to measure γ, the parameters r_{B^0} and δ_{B^0} are not well known and are typically also determined from measurements of the partial widths.

The size of the interference term also depends on parameters related to the D-meson decay, r_D and δ_D, which depend on the final state f and can be input from external measurements. To achieve a high precision on γ, it is best to study multiple D-meson final states and combine the results. This thesis studies final states involving charged kaons and pions, which the LHCb experiment excels at detecting and identifying. An analysis strategy using two- and four-body D-meson decays is outlined in Sect. 2.6, and a strategy with three-body D-meson decays is discussed in Sect. 2.7.

2.6 Measurements with two- and four-body D-meson decays: the GLW and ADS methods

2.6.1 The GLW method

The simplest method for measuring γ, proposed by Gronau, London, and Wyler (GLW) [25, 26], uses *CP*-even D-meson final states, K^+K^- and $\pi^+\pi^-$, both of which are singly Cabibbo suppressed. In this case, $r_D = 1$ and $\delta_D = 0$. This simplifies Eqs. 2.24–2.27 to just two equations:

$$\Gamma(B^0 \to D_{CP}K^{*0}) \propto 1 + r_{B^0}^2 + 2\kappa r_{B^0}\cos(\delta_{B^0} + \gamma), \tag{2.28}$$

$$\Gamma(\overline{B}^0 \to D_{CP}\overline{K}^{*0}) \propto 1 + r_{B^0}^2 + 2\kappa r_{B^0}\cos(\delta_{B^0} - \gamma), \tag{2.29}$$

where D_{CP} represents a D meson decaying to any *CP*-even final state. We can access information about γ, r_{B^0}, and δ_{B^0} by measuring the asymmetry

$$\mathcal{A}_{CP} \equiv \frac{\Gamma(\overline{B}^0 \to D_{CP}\overline{K}^{*0}) - \Gamma(B^0 \to D_{CP}K^{*0})}{\Gamma(\overline{B}^0 \to D_{CP}\overline{K}^{*0}) + \Gamma(B^0 \to D_{CP}K^{*0})}, \tag{2.30}$$

which can be measured for each final state, yielding $\mathcal{A}_{CP}^{KK}$ and $\mathcal{A}_{CP}^{\pi\pi}$. These quantities are expected to be equal when *CP* violation in the D-meson decay is ignored. The asymmetry is related to the underlying parameters by

$$\mathcal{A}_{CP} = \frac{2\kappa r_{B^0}\sin\delta_{B^0}\sin\gamma}{1 + r_{B^0}^2 + 2\kappa\cos\delta_{B^0}\cos\gamma}. \tag{2.31}$$

Further information is contained in the charge-averaged rate of decays involving a D meson decaying to a *CP* eigenstate, defined as

$$\mathcal{R}_{CP} \equiv 2\frac{\Gamma(\overline{B}^0 \to D_{CP}\overline{K}^{*0}) + \Gamma(B^0 \to D_{CP}K^{*0})}{\Gamma(\overline{B}^0 \to D^0\overline{K}^{*0}) + \Gamma(B^0 \to \overline{D}^0K^{*0})}. \tag{2.32}$$

This is related to γ and the auxiliary parameters through

$$\mathcal{R}_{CP} = 1 + r_{B^0}^2 + 2\kappa r_{B^0}\cos\delta_{B^0}\cos\gamma. \tag{2.33}$$

The numerator of Eq. 2.6.1 can be accessed experimentally through decays to *CP*-even eigenstates, such as $B^0 \to D(h^+h^-)K^{*0}$. The Cabibbo-favoured decay $B^0 \to$

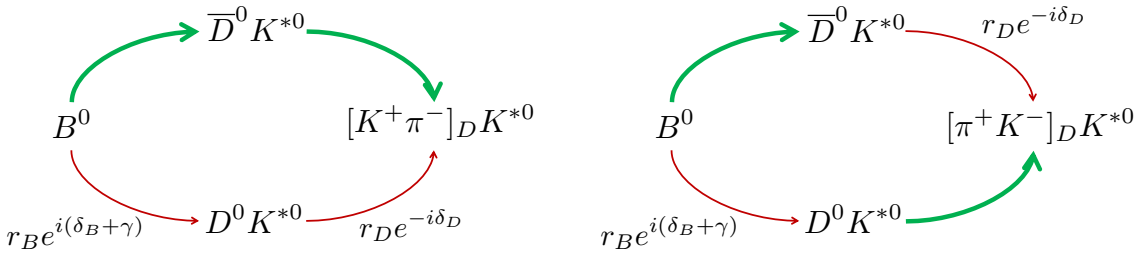

(a) Favoured (b) Suppressed

Figure 2.8: Interfering amplitudes in (a) favoured ADS decays and (b) suppressed ADS decays. The relative amplitudes of the intermediate decays are indicated. Thick green arrows show favoured amplitudes, and thin red arrows show suppressed amplitudes.

$D(K^-\pi^+)K^{*0}$ proceeds primarily via a D^0 meson with very little interference, and can therefore be used to access the denominator. The rates of these decays must be normalised by the known branching fractions of the D-meson decays. We can then construct an experimentally measurable quantity,

$$\mathcal{R}_{CP}^{hh} \equiv \frac{\Gamma(\overline{B}^0 \to D(h^+h^-)\overline{K}^{*0}) + \Gamma(B^0 \to D(h^+h^-)K^{*0})}{\Gamma(\overline{B}^0 \to D(K^-\pi^+)\overline{K}^{*0}) + \Gamma(B^0 \to D(K^+\pi^-)K^{*0})} \times \frac{\mathcal{B}(D^0 \to K^-\pi^+)}{\mathcal{B}(D^0 \to h^+h^-)}, \tag{2.34}$$

which is equal to $\mathcal{R}_{CP}$ when the small amount of interference in $B^0 \to D(K^-\pi^+)K^{*0}$ decays is ignored. The GLW strategy yields four observables: $\mathcal{A}_{CP}^{KK}$, $\mathcal{A}_{CP}^{\pi\pi}$, $\mathcal{R}_{CP}^{KK}$, and $\mathcal{R}_{CP}^{\pi\pi}$.

2.6.2 The ADS method

An alternative method using $D \to K^\pm\pi^\mp$ decays was proposed by Atwood, Dunietz, and Soni (ADS) [27, 28]. There are two categories of such decays, one favoured and one suppressed. A schematic of the interfering amplitudes in each category is shown in Fig. 2.8.

In the favoured case, the decay proceeds predominantly via a favoured $B^0 \to \overline{D}^0 K^{*0}$ decay followed by a favoured $\overline{D}^0 \to K^+\pi^-$ decay. This process therefore has a relatively large partial width. However, as the interfering amplitude is highly suppressed, the interference term is extremely small and this mode has little sensitivity to γ; nonetheless, it serves as a useful normalisation mode, such as in Eq. 2.34. The

favoured mode is characterised by the kaons from the decays of the D and K^{*0} mesons having the same charge.

In the suppressed mode, the amplitude of a favoured $B^0 \to \overline{D}^0 K^{*0}$ decay followed by a doubly Cabibbo-suppressed $\overline{D}^0 \to \pi^+ K^-$ decay interferes with the amplitude of a suppressed $B^0 \to D^0 K^{*0}$ decay followed by a favoured $D^0 \to \pi^+ K^-$ decay. These amplitudes have similar magnitudes, so the interference effects are enhanced, providing even more sensitivity to γ than in the GLW case. The kaons from the decays of the D and K^{*0} mesons have opposite charges in this process.

The partial-rate asymmetry of the suppressed ADS mode is given by

$$\mathcal{A}_{\rm ADS}^{\pi K} \equiv \frac{\Gamma(\overline{B}^0 \to D(\pi^- K^+)\overline{K}^{*0}) - \Gamma(B^0 \to D(\pi^+ K^-)K^{*0})}{\Gamma(\overline{B}^0 \to D(\pi^- K^+)\overline{K}^{*0}) + \Gamma(B^0 \to D(\pi^+ K^-)K^{*0})}, \tag{2.35}$$

and the charge-averaged ratio with respect to the favoured mode is given by

$$\mathcal{R}_{\rm ADS}^{\pi K} \equiv \frac{\Gamma(\overline{B}^0 \to D(\pi^- K^+)\overline{K}^{*0}) + \Gamma(B^0 \to D(\pi^+ K^-)K^{*0})}{\Gamma(\overline{B}^0 \to D(K^- \pi^+)\overline{K}^{*0}) + \Gamma(B^0 \to D(K^+ \pi^-)K^{*0})}. \tag{2.36}$$

These observables have the following dependencies on γ and the auxiliary parameters:

$$\mathcal{A}_{\rm ADS}^{\pi K} = \frac{2\kappa r_{B^0} r_D \sin(\delta_{B^0} + \delta_D) \sin\gamma}{r_{B^0}^2 + r_D^2 + 2\kappa r_{B^0} r_D \cos(\delta_{B^0} + \delta_D)\cos\gamma}, \tag{2.37}$$

$$\mathcal{R}_{\rm ADS}^{\pi K} = \frac{r_{B^0}^2 + r_D^2 + 2\kappa r_{B^0} r_D \cos(\delta_{B^0} + \delta_D)\cos\gamma}{1 + r_{B^0}^2 r_D^2 + 2\kappa r_{B^0} r_D \cos(\delta_{B^0} + \delta_D)\cos\gamma}, \tag{2.38}$$

where $r_D = (5.87 \pm 0.02) \times 10^{-2}$ is the ratio between the magnitudes of the suppressed and favoured D-meson amplitudes, and $\delta_D = (192.1\,^{+8.6}_{-10.2})^\circ$ is the strong-phase difference between the amplitudes [29].[1] The ADS asymmetry is expected to be larger than the GLW asymmetry given in Eq. 2.31, but has a lower statistical sensitivity.

The quantities measured experimentally are the ratios

$$\mathcal{R}_+^{\pi K} = \frac{\Gamma(B^0 \to D(\pi^+ K^-)K^{*0})}{\Gamma(B^0 \to D(K^+ \pi^-)K^{*0})} \tag{2.39}$$

and

$$\mathcal{R}_-^{\pi K} = \frac{\Gamma(\overline{B}^0 \to D(\pi^- K^+)\overline{K}^{*0})}{\Gamma(\overline{B}^0 \to D(K^- \pi^+)\overline{K}^{*0})}, \tag{2.40}$$

[1] All expressions and charm strong-phase values are given in the convention $CP|D^0\rangle = |\overline{D}^0\rangle$. This implies a 180° offset with respect to the values quoted in Ref. [29], which are defined with a different sign convention.

which exhibit better statistical behaviour than $\mathcal{A}_{\rm ADS}^{\pi K}$ and $\mathcal{R}_{\rm ADS}^{\pi K}$ in these low-yielding decays. The relationships

$$\mathcal{A}_{\rm ADS}^{\pi K} \simeq (\mathcal{R}_{-}^{\pi K} - \mathcal{R}_{+}^{\pi K})/(\mathcal{R}_{-}^{\pi K} + \mathcal{R}_{+}^{\pi K}) \tag{2.41}$$

and

$$\mathcal{R}_{\rm ADS}^{\pi K} \simeq (\mathcal{R}_{+}^{\pi K} + \mathcal{R}_{-}^{\pi K})/2 \tag{2.42}$$

allow the ADS observables to be recovered, where the approximate equalities are exact in the absence of *CP* asymmetry in the favoured mode. The favoured mode asymmetry

$$\mathcal{A}_{\rm ADS}^{K\pi} = \frac{\Gamma(\overline{B}^0 \to D(K^-\pi^+)\overline{K}^{*0}) - \Gamma(B^0 \to D(K^+\pi^-)K^{*0})}{\Gamma(\overline{B}^0 \to D(K^-\pi^+)\overline{K}^{*0}) + \Gamma(B^0 \to D(K^+\pi^-)K^{*0})} \tag{2.43}$$

is measured, and is expected to be much smaller than the asymmetry in the suppressed mode.

2.6.3 Extension to four-body *D*-meson decays

The decay $D \to \pi^+\pi^-\pi^+\pi^-$ contains a mixture of *CP*-even and *CP*-odd states. Provided we know the *CP*-even content of the decay, the GLW method can be applied to this mode [30, 31]. The *CP*-even fraction, $F_+^{4\pi}$, is measured to be 0.769 ± 0.023 from decays of quantum-correlated D mesons [32]. We measure the observables $\mathcal{A}_{CP}^{4\pi}$ and $\mathcal{R}_{CP}^{4\pi}$, which are analogous to the two-body observables $\mathcal{A}_{CP}^{hh}$ and $\mathcal{R}_{CP}^{hh}$, respectively. These observables can be interpreted through equivalent expressions to Eqs. 2.31 and 2.33 in which the interference terms acquire a factor of $(2F_+^{4\pi} - 1)$, *i.e.* the *CP* violation is diluted by the non-*CP*-even contributions.

The ADS method can be extended to $D \to K^\pm\pi^\mp\pi^+\pi^-$ decays. The two-body ADS decays $D \to K^\pm\pi^\mp$ are characterised by a single ratio, r_D, and strong-phase difference, δ_D; in the four-body case, these parameters vary over the phase space of the D-meson decay products. As proposed in Ref. [33], we can describe the four-body decays using three hadronic parameters obtained by integrating over the $K^\pm\pi^\mp\pi^+\pi^-$

phase space coordinate p:

$$(r_D^{K3\pi})^2 = \frac{\int \mathrm{d}p\, |A_{\mathrm{sup}}(p)|^2}{\int \mathrm{d}p\, |A_{\mathrm{fav}}(p)|^2}, \tag{2.44}$$

$$\kappa_D^{K3\pi} e^{i\delta_D^{K3\pi}} = \frac{\int \mathrm{d}p\, A_{\mathrm{sup}}(p) A_{\mathrm{fav}}(p)}{\sqrt{\int \mathrm{d}p\, |A_{\mathrm{sup}}(p)|^2}\sqrt{\int \mathrm{d}p\, |A_{\mathrm{fav}}(p)|^2}}, \tag{2.45}$$

where A_{sup} and A_{fav} are the amplitudes of suppressed $D^0 \to K^+\pi^-\pi^+\pi^-$ decays and favoured $D^0 \to K^-\pi^+\pi^+\pi^-$ decays, respectively. The parameters $r_D^{K3\pi}$ and $\delta_D^{K3\pi}$ are the average magnitude ratio and strong-phase difference, respectively, between these amplitudes. The coherence factor $\kappa_D^{K3\pi}$ quantifies the dilution of interference effects due to this averaging. These parameters have been measured in studies of charm mixing and quantum-correlated D-meson decays: $r_D^{K3\pi} = (5.49 \pm 0.06) \times 10^{-2}$, $\delta_D^{K3\pi} = (128\,^{+28}_{-17})^\circ$, and $\kappa_D^{K3\pi} = 0.43\,^{+0.17}_{-0.13}$ [34, 35].

While a more sensitive method, involving dividing the phase space into regions of high coherence and measuring the *CP* observables separately in each region, has been proposed [36], here we use the simpler method of averaging over the entire phase space. We measure the observables $\mathcal{R}_+^{\pi K\pi\pi}$, $\mathcal{R}_-^{\pi K\pi\pi}$, and $\mathcal{A}_{\mathrm{ADS}}^{K\pi\pi\pi}$, which are analogous to the two-body ADS observables. They are interpreted in terms of γ, r_{B^0}, and δ_{B^0} using equivalent expressions to Eqs. 2.37 and 2.38 in which r_D and δ_D are replaced with $r_D^{K3\pi}$ and $\delta_D^{K3\pi}$, respectively, and interference terms are multiplied by $\kappa_D^{K3\pi}$.

2.6.4 Summary of GLW and ADS observables

Measurements of the ratios and asymmetries of the partial decay widths of $B^0 \to DK^{*0}$ decays with the D meson decaying to two- and four-body combinations of charged kaons and pions are used to determine twelve *CP* observables. In the GLW modes K^+K^-, $\pi^+\pi^-$, and $\pi^+\pi^-\pi^+\pi^-$, we measure $\mathcal{A}_{CP}^{KK}$, $\mathcal{A}_{CP}^{\pi\pi}$, $\mathcal{R}_{CP}^{KK}$, $\mathcal{R}_{CP}^{\pi\pi}$, $\mathcal{A}_{CP}^{4\pi}$, and $\mathcal{R}_{CP}^{4\pi}$. In the ADS modes $K^\pm\pi^\mp$ and $K^\pm\pi^\mp\pi^+\pi^-$, we measure $\mathcal{R}_+^{\pi K}$, $\mathcal{R}_-^{\pi K}$, $\mathcal{R}_+^{\pi K\pi\pi}$, $\mathcal{R}_-^{\pi K\pi\pi}$, $\mathcal{A}_{\mathrm{ADS}}^{K\pi}$, and $\mathcal{A}_{\mathrm{ADS}}^{K\pi\pi\pi}$.

The final state DK^{*0} is also accessible to B_s^0 mesons, which are therefore present in samples of $B^0 \to DK^{*0}$ decays. While in principle the twelve *CP* observables can

be measured in the decays of B_s^0 mesons, the amplitude ratio $r_{B_s^0}$ in these decays is around 0.01, so the interference terms are significantly suppressed. The B_s^0-meson observables are therefore not used to determine γ with the current data sample size.

2.7 Measurements with three-body D-meson decays: the GGSZ method

The ADS/GLW observables defined in Sect. 2.6 have trigonometric dependencies on γ and δ_{B^0}, so their measurements provide multiple solutions in (γ, δ_{B^0}) parameter space. A complementary measurement that determines a single value of γ can be made using D-meson decays to self-conjugate three-body final states, $K^0_S\pi^+\pi^-$ and $K^0_S K^+ K^-$.

The magnitude ratio and strong-phase difference between the amplitudes of the decays of D^0 and $\overline{D}^0$ mesons to these final states vary significantly across the phase space of the decay products. The amount of *CP* violation therefore also varies across the phase space. A method for measuring γ proposed by Giri, Grossman, Soffer, and Zupan (GGSZ) [37] exploits this variation by comparing the phase-space distributions of the decays of B^0 and $\overline{B}^0$ mesons, rather than measuring the overall asymmetry.

2.7.1 Dalitz plots for three-body D-meson decays

In the rest frame of a D meson decaying to the final state $K^0_S h^+ h^-$ ($h = K, \pi$), there are twelve degrees of freedom corresponding to the four-momenta of each final-state particle. Conservation of energy and three-momentum imposes four constraints. The fixed masses of the K^0_S and $h^\pm$ mesons impose a further three constraints. The initial and final-state particles have zero spin, so the angular distribution of the decay products is uniform; we can study the amplitude of decays integrated over the three Euler angles to impose three more constraints. This leaves only two degrees of freedom in the final state, so the amplitude of the decay can be fully specified as a function of only two kinematic variables.

The phase space of $D^0 \to K^0_S h^+ h^-$ decays can be visualised using a two-dimensional "Dalitz plot" [38]. The axes of a Dalitz plot are the squared invariant masses of any two of the three D-meson decay products, defined by $m^2(AB) \equiv (p_A + p_B)^2$, where p_A and p_B are the four-momenta of particles A and B, respectively. In the case of

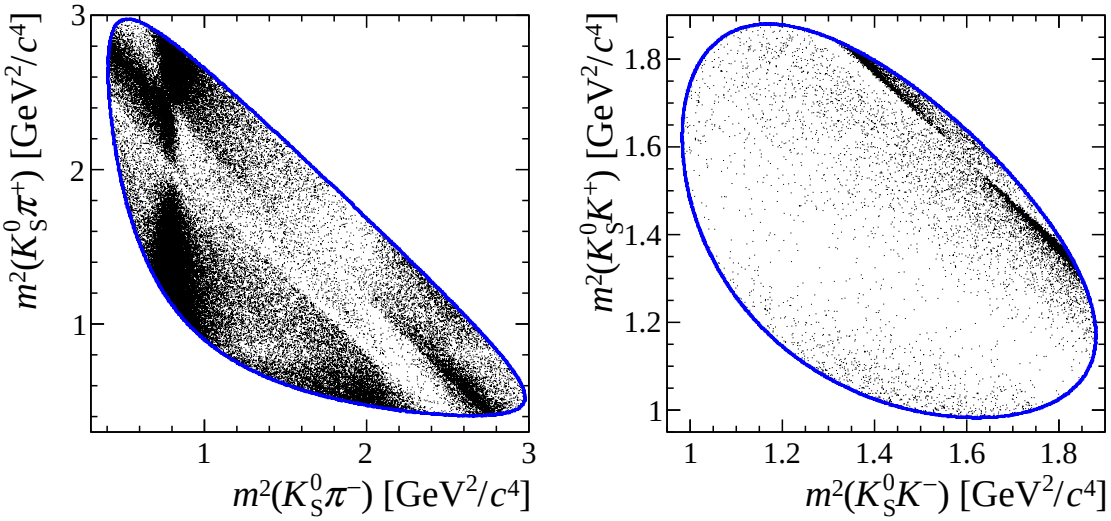

(a) $D \to K^0_S\pi^+\pi^-$ (b) $D \to K^0_SK^+K^-$

Figure 2.9: Dalitz plots of (a) $D \to K^0_S\pi^+\pi^-$ decays and (b) $D \to K^0_SK^+K^-$ decays in LHCb data, reproduced from Ref. [39]. The blue line corresponds to the kinematic boundary imposed by the mass of the D meson.

$D^0 \to K^0_Sh^+h^-$ decays, we have three options: $m^2(K^0_Sh^+)$, $m^2(K^0_Sh^-)$, and $m^2(h^+h^-)$. For symmetry reasons we choose $m^2(K^0_Sh^+)$ and $m^2(K^0_Sh^-)$, which we refer to with the shorthand $m^2_+ \equiv m^2(K^0_Sh^+)$ and $m^2_- \equiv m^2(K^0_Sh^-)$.

Figure 2.9 shows the distributions of samples of $D^0 \to K^0_S\pi^+\pi^-$ and $D^0 \to K^0_SK^+K^-$ decays in the (m^2_-, m^2_+) plane. Because the total invariant mass of the final-state particles equals the mass of the D^0 meson, there is a kinematic boundary on the plot. The internal structure of the plot arises from nonresonant contributions, intermediate resonances, and interference between resonant and/or nonresonant contributions. These structures have been studied in detail in dedicated amplitude analyses [40, 41]. Some notable features are a vertical band at $m^2_- \sim 0.8\,\text{GeV}/c^2$ in the $D^0 \to K^0_S\pi^+\pi^-$ plot, resulting from the intermediate resonance $K^*(892)^- \to K^0_S\pi^-$, and a diagonal band in the $D \to K^0_SK^+K^-$ plot from the resonance $\phi(1020) \to K^+K^-$.

The total amplitude at each point, $A_D(m^2_-, m^2_+)$, is the sum of all contributing amplitudes. The amplitudes A_D and $\overline{A}_D$ of the decays of D^0 and $\overline{D}^0$ mesons, respec-

tively, can be written as

$$A_D(m_-^2, m_+^2) \equiv a(m_-^2, m_+^2)e^{i\delta(m_-^2, m_+^2)}, \tag{2.46}$$

$$\overline{A}_D(m_-^2, m_+^2) \equiv \bar{a}(m_-^2, m_+^2)e^{i\bar{\delta}(m_-^2, m_+^2)}, \tag{2.47}$$

and are related by the transformation $m_-^2 \leftrightarrow m_+^2$. The (m_-^2, m_+^2) dependence of a, $\bar{a}$, δ, and $\bar{\delta}$ is implied for the remainder of this discussion.

2.7.2 The GGSZ method for $B^0 \to DK^{*0}$ decays

The amplitude of the decay $B^0 \to D(K_S^0 h^+ h^-)K^{*0}$ is obtained by combining the D-meson amplitudes in Eqs. 2.46 and 2.47 with the B^0-meson amplitudes in Eqs. 2.12 and 2.13 to give

$$A(B^0 \to D(K_S^0 h^+ h^-)K^{*0}) = A_c(p)e^{i\delta_c(p)}\bar{a}e^{i\bar{\delta}} + A_u(p)e^{i(\delta_u(p)-\gamma)}ae^{i\delta}. \tag{2.48}$$

The partial width, Γ, is calculated by squaring the amplitude and integrating over the phase space of the B^0-meson decay products, giving

$$\Gamma(B^0 \to D(K_S^0 h^+ h^-)K^{*0}) \propto \bar{a}^2 + r_{B^0}^2 a^2 + 2\kappa a\bar{a}r_{B^0}\cos[(\delta_{B^0} - \gamma) + (\delta - \bar{\delta})], \tag{2.49}$$

where the parameters r_{B^0}, δ_{B^0}, and κ are defined in Eqs. 2.22 and 2.23. Further defining the strong-phase difference between the D^0-meson and $\overline{D}^0$-meson amplitudes as $\delta_D = \delta - \bar{\delta}$, this expression can be rewritten as

$$\begin{aligned}\Gamma(B^0 \to D(K_S^0 h^+ h^-)K^{*0}) \propto\ & \bar{a}^2 + r_{B^0}^2 a^2 \\ & + 2\kappa a\bar{a}r_{B^0}[\cos(\delta_{B^0} - \gamma)\cos(\delta_D) - \sin(\delta_{B^0} - \gamma)\sin(\delta_D)].\end{aligned} \tag{2.50}$$

The partial width of the *CP*-conjugate $\overline{B}^0$-meson decay is found by repeating the process with the $\overline{B}^0$-meson amplitudes in Eqs. 2.14 and 2.15, giving

$$\begin{aligned}\Gamma(\overline{B}^0 \to D(K_S^0 h^+ h^-)\overline{K}^{*0}) \propto\ & a^2 + r_{B^0}^2 \bar{a}^2 \\ & + 2\kappa a\bar{a}r_{B^0}[\cos(\delta_{B^0} + \gamma)\cos(\delta_D) + \sin(\delta_{B^0} + \gamma)\sin(\delta_D)].\end{aligned} \tag{2.51}$$

In the absence of interference ($r_{B^0} = 0$) and/or *CP* violation ($\gamma = 0$), the Dalitz plot distributions of the decays of B^0 and $\overline{B}^0$ mesons are identical under the transformation

$m_-^2 \leftrightarrow m_+^2$; however, if r_{B^0} and γ are nonzero, they are different. The parameters γ, r_{B^0}, and δ_{B^0} can be determined from a measurement of the B^0–$\overline{B}^0$ asymmetry as a function of (m_-^2, m_+^2), provided we know a and δ_D.

In a "model-dependent" analysis, a and δ_D are taken from an amplitude model. A systematic uncertainty must be assigned to account for potential biases due to the uncertainty of the model, the size of which is difficult to estimate reliably. This issue is avoided in a "model-independent" analysis, where the amplitude and strong-phase difference are taken from measurement. The uncertainties on these measurements are well known and can be reliably propagated to the results. This thesis presents a model-independent analysis using strong-phase information measured by the BESIII and CLEO experiments, discussed in Sect. 2.7.3, and an amplitude distribution measured with $B^+ \to D\pi^+$ decays, discussed in Sect. 6.1.

In practice, the amplitude and strong-phase parameters are measured in discrete bins of the Dalitz plot. To make use of these measurements, we must bin our B^0-meson-decay data in the same way and measure the yield in each bin. The interference term is symmetric under the transformation $m_-^2 \leftrightarrow m_+^2$, so the bin regions are defined to be symmetric about the line $m_-^2 = m_+^2$. Bins in the region $m_-^2 > m_+^2$ are labelled $i = \{1, 2, \ldots k\}$, and the symmetrical bins in the region $m_-^2 < m_+^2$ are labelled $i = \{-1, -2, \ldots -k\}$, giving $2k$ bins in total.

The binning schemes used are based on an amplitude model developed by the BaBar collaboration [41] and are chosen to maximise sensitivity to γ. Note that the use of an amplitude model to define the binning does not introduce any model-dependent bias in the final measurement; if the structure of the D-meson decay is different in nature than in the model, there will merely be a difference in statistical sensitivity compared with expectation. For $D \to K^0_S\pi^+\pi^-$ decays, a scheme with 8 bins called the "optimal binning" scheme is used. For $D \to K^0_S K^+ K^-$ decays, which are less abundant, the "2-bin" scheme is used. Both schemes are shown in Fig. 2.10.

For each bin i, we define the parameter T_i as the integral of the squared D^0-meson

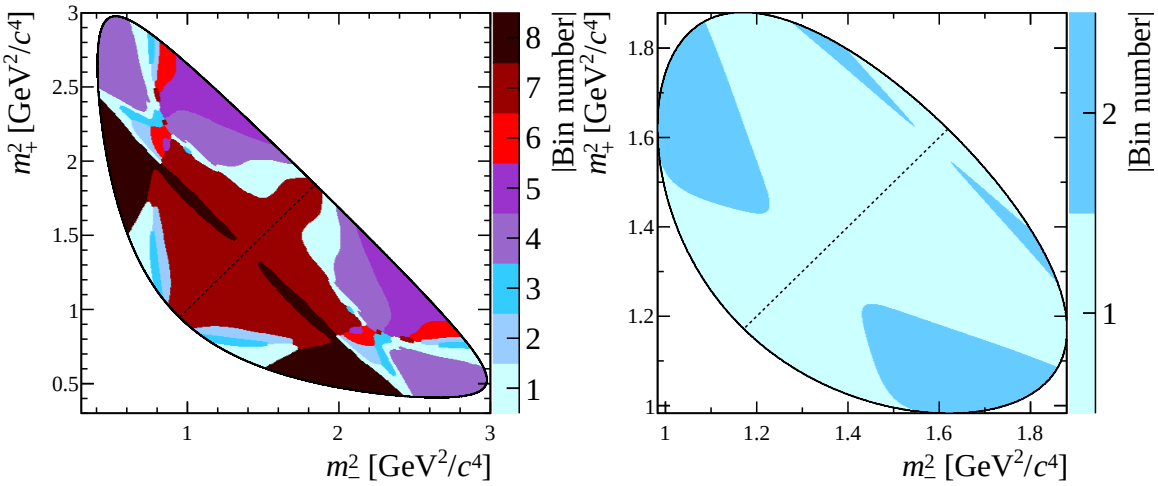

(a) $D \to K^0_S\pi^+\pi^-$ (b) $D \to K^0_S K^+K^-$

Figure 2.10: Binning schemes for (a) $D \to K^0_S\pi^+\pi^-$ decays using the "optimal binning" scheme and (b) $D \to K^0_S K^+K^-$ decays using the "2-bin" scheme. The dotted line separates positive and negative bin numbers, where positive bins are in the region $m^2_- > m^2_+$.

amplitude in that bin,

$$T_i \;= \int_i \mathrm{d}m^2_- \mathrm{d}m^2_+ \, a^2(m^2_-, m^2_+). \tag{2.52}$$

The amplitudes of the decays of D^0 and $\overline{D}^0$ mesons are related by the transformation $m^2_- \leftrightarrow m^2_+$, so the integrated D^0-meson amplitude in the corresponding negative bin, T_{-i}, is equal to the integrated $\overline{D}^0$-meson amplitude in bin i:

$$T_{-i} = \int_{-i} \mathrm{d}m^2_- \mathrm{d}m^2_+ \, a^2(m^2_-, m^2_+) = \int_i \mathrm{d}m^2_- \mathrm{d}m^2_+ \, \bar{a}^2(m^2_-, m^2_+). \tag{2.53}$$

We also define two strong-phase parameters,

$$c_i = \frac{1}{\sqrt{T_i T_{-i}}} \int_i \mathrm{d}m^2_- \mathrm{d}m^2_+ \, a(m^2_-, m^2_+)\bar{a}(m^2_-, m^2_+) \cos\delta_D(m^2_-, m^2_+), \tag{2.54}$$

$$s_i = \frac{1}{\sqrt{T_i T_{-i}}} \int_i \mathrm{d}m^2_- \mathrm{d}m^2_+ \, a(m^2_-, m^2_+)\bar{a}(m^2_-, m^2_+) \sin\delta_D(m^2_-, m^2_+), \tag{2.55}$$

which obey the relationships $c_i = c_{-i}$ and $s_i = -s_{-i}$.

The parameters of interest can be written as Cartesian parameters,

$$x_\pm \equiv r_{B^0} \cos(\delta_{B^0} \pm \gamma), \tag{2.56}$$

$$y_\pm \equiv r_{B^0} \sin(\delta_{B^0} \pm \gamma). \tag{2.57}$$

Using these parameters, we can rewrite the partial widths of the decays of B^0 and $\overline{B}^0$ mesons in each bin as

$$\begin{aligned}\Gamma_{\pm i}(B^0 \to D(K^0_S h^+ h^-)K^{*0}) \\ \propto T_{\mp i} + (x_+^2 + y_+^2)T_{\pm i} + 2\kappa\sqrt{T_{+i}T_{-i}}(x_+ c_{\pm i} - y_+ s_{\pm i}),\end{aligned} \tag{2.58}$$

$$\begin{aligned}\Gamma_{\pm i}(\overline{B}^0 \to D(K^0_S h^+ h^-)\overline{K}^{*0}) \\ \propto T_{\pm i} + (x_-^2 + y_-^2)T_{\mp i} + 2\kappa\sqrt{T_{+i}T_{-i}}(x_- c_{\pm i} + y_- s_{\pm i}).\end{aligned} \tag{2.59}$$

For a binning scheme with $2k$ bins, there are $4k$ equations. In a model-independent analysis, the parameters $T_{\pm i}$, c_i, and s_i are taken from measurement. The only unknown parameters are then $x_\pm$ and $y_\pm$, which can be measured from the yields of B^0-meson and $\overline{B}^0$-meson decays in each bin and used to determine γ, r_{B^0}, and δ_{B^0} through the straightforward relationships in Eqs. 2.56 and 2.57.

2.7.3 Strong-phase inputs

The values of c_i and s_i are taken from a combination of measurements made by the CLEO [42] and BESIII [43] collaborations. These measurements use samples of data from electron-positron collisions at a centre-of-mass energy of 3.773 GeV; this produces the $\psi(3770)$ resonance, which decays to quantum-entangled pairs of D^0 and $\overline{D}^0$ mesons.

The decays of the D mesons in these pairs are not independent; for example, if one decays to a *CP*-even eigenstate, the other must decay to a *CP*-odd eigenstate. This property is exploited by studying "double-tagged" events, where one D-meson final state is tagged as $D \to K^0_S h^+ h^-$ and the other is tagged as either a *CP*-even, *CP*-odd, or flavour-specific final state. The D^0 and $\overline{D}^0$ content of the latter decay is known, so we also know the D^0 and $\overline{D}^0$ content of the entangled $D \to K^0_S h^+ h^-$ decay. The yields of each type of double-tagged event in each Dalitz bin are used to determine c_i and s_i.

2.8 Previous measurements of $B^0 \to DK^{*0}$ decays

Measurements of $B^0 \to DK^{*0}$ decays have previously been made using LHCb data collected from 2011–2012. An ADS/GLW analysis using two-body D-meson final states measured the amplitude ratio to be $r_{B^0} = 0.240\,^{+0.055}_{-0.048}$ and placed constraints on the (γ, δ_{B^0}) parameter space [44]. The suppressed ADS decay $B^0 \to D(\pi^+K^-)K^{*0}$ was observed to a significance of 2.7σ, which did not meet the 5σ threshold for a first observation.

An amplitude analysis of the full phase space of $B^0 \to DK^+\pi^-$ decays has been performed at LHCb using the two-body GLW modes [45]. The suppressed ADS mode was not studied due to challenging background levels. The model determined in this analysis predicts the value of the K^{*0} coherence factor to be $\kappa = 0.958\,^{+0.005}_{-0.046}$ for a particular region of $DK^+\pi^-$ phase space; this region is used for the measurements in this thesis.

The BaBar and Belle collaborations have studied $B^0 \to DK^{*0}$ decays with the D meson reconstructed in the ADS modes [46, 47]. The signal yields in these analyses are very low, so upper limits on $R_{\rm ADS}$ are presented. The BaBar analysis also studies the final states $D \to K^\pm\pi^\mp\pi^0$ and $K^\pm\pi^\mp\pi^+\pi^-$; this is the only prior measurement of $B^0 \to DK^{*0}$ decays with a four-body D-meson final state.

The GGSZ modes have been studied by Belle using the model-independent method [48] and by LHCb with both the model-dependent [49] and model-independent [21] methods. The model-independent LHCb analysis measures the following parameters: $\gamma = (71 \pm 20)^\circ$, $r_{B^0} = 0.56 \pm 0.17$, and $\delta_{B^0} = (204\,^{+21}_{-20})^\circ$.

The overall LHCb γ combination [23,24] uses measurements from the ADS analysis of $B^0 \to D(K^\pm\pi^\mp)K^{*0}$ [50], the amplitude analysis of $B^0 \to D(h^+h^-)K^+\pi^-$ [45], and the model-independent GGSZ analysis of $B^0 \to D(K^0_{\rm S}h^+h^-)K^{*0}$ [51], in addition to inputs from other B-meson decays. The B^0-meson decay parameters are found to be $r_{B^0} = 0.221\,^{+0.044}_{-0.047}$ and $\delta_{B^0} = (187\,^{+23}_{-20})^\circ$. The best-fit value of γ is $(74.0\,^{+5.0}_{-5.8})^\circ$; this is dominated by measurements of $B^+ \to DK^+$ decays, which alone give $\gamma = (69.8\,^{+5.9}_{-7.1})^\circ$.

The analyses presented in Chaps. 4 to 7 of this thesis are updates to the ADS/GLW and GGSZ analyses published in Refs. [44] and [51], respectively. These updates benefit from larger data sets, improved selection methods, and a better understanding of the B^0-meson invariant-mass distribution. The ADS/GLW analysis also incorporates four-body D-meson decays for the first time at LHCb, which improves the constraint on γ. The results of these analyses are combined in Chap. 8 to give a measurement of γ using only $B^0 \to DK^{*0}$ decays.

Chapter 3

The LHCb experiment

The B^0 meson has a mass of $5.28\,\mathrm{GeV}/c^2$, and can therefore only be produced in a high-energy interaction. This can be achieved using collider experiments, which collide accelerated beams of charged particles at large centre-of-mass energies to produce heavier particles. While B^0 mesons decay too rapidly to seen directly, their decay products can be observed by a particle detector and used to reconstruct the B^0-meson decay.

The Large Hadron Collider (LHC) at CERN is a circular proton-proton (pp) collider with a circumference of 27 km. Figure 3.1 shows the CERN accelerator complex. The protons begin as hydrogen atoms, which are ionised and boosted to an energy of 25 GeV by the Proton Synchrotron (PS). The Super Proton Synchrotron (SPS) increases this energy more than tenfold to 450 GeV. The protons are then injected as two separate beams into the LHC, where they circulate in opposite directions. A series of superconducting dipole magnets bends the beams into a circular shape, while further magnets focus and stabilise the beams. Accelerating cavities boost the beams to their final energies of 6.5 TeV. The LHC can hold up to 2808 bunches of $\mathcal{O}(10^{11})$ protons.

Once stable, the proton beams are brought together to collide with a combined energy of 13 TeV. This occurs at four points around the ring, where the four main LHC detector experiments are situated: the Large Hadron Collider Beauty (LHCb) experiment and the ATLAS, CMS, and ALICE experiments. The beams can circulate

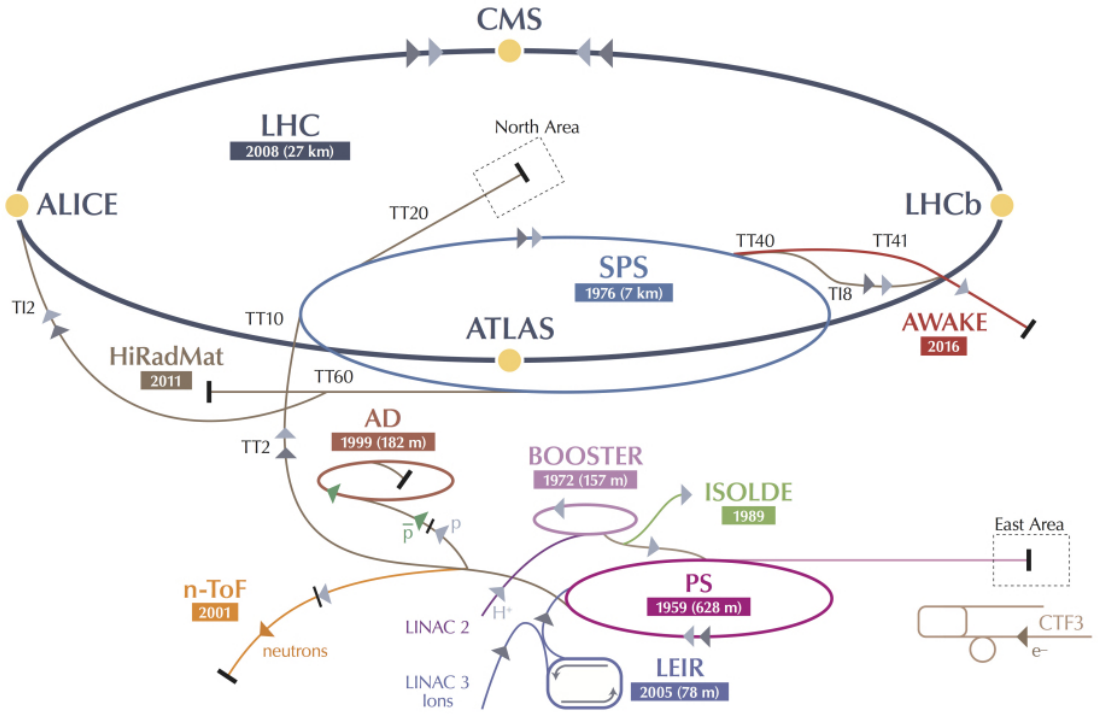

Figure 3.1: Schematic of the CERN accelerator complex, reproduced from Ref. [52]. Protons used in pp collisions at the LHC follow the sequence LINAC 2 $\rightarrow$ BOOSTER $\rightarrow$ PS $\rightarrow$ SPS $\rightarrow$ LHC.

for several hours while continuously colliding, in a period known as a "fill", until the number of protons becomes too low to be useful.

The LHC has completed two major periods of data taking. During Run 1 (2010–2012), the LHC ran at a reduced energy of 7–8 TeV. The energy was increased to 13 TeV in Run 2 (2015–2018). This thesis only considers data from 2011 onwards, as the luminosities in 2010 were very low. The spacing between the proton bunches was 50 ns in Run 1 and was reduced to 25 ns in Run 2.

The rate $\frac{\mathrm{d}N}{\mathrm{d}t}$ of a scattering process, such as the production of a pair of $b\bar{b}$ quarks, depends on its interaction cross-section σ and the instantaneous luminosity of the collision $\mathcal{L}_{\text{inst}}$ via

$$\frac{\mathrm{d}N}{\mathrm{d}t} = \mathcal{L}_{\text{inst}}\sigma. \tag{3.1}$$

The amount of data collected over some period of time is quantified by the integrated

Table 3.1: Collision energy and integrated luminosity for each year of data taking in Run 1 and Run 2 at the LHCb experiment.

	Run 1		**Run 2**			
	2011	2012	2015	2016	2017	2018
Collision energy (TeV)	7	8	13	13	13	13
Integrated luminosity (fb^{-1})	1.0	2.0	0.3	1.6	1.7	2.1

luminosity,

$$\mathcal{L} = \int \mathcal{L}_{\text{inst}} \, \mathrm{d}t, \tag{3.2}$$

which is measured in units of fb^{-1}. Table 3.1 gives the collision energies and integrated luminosities collected each year by the LHCb experiment.

At the ATLAS and CMS experiments, the proton beams are collided head-on to obtain the maximum possible instantaneous luminosity, which decreases throughout the fill as the number of protons in each bunch is depleted. The LHCb experiment is optimised to operate at a lower instantaneous luminosity, achieved by deliberately offsetting the beams. Figure 3.2 compares the instantaneous luminosities throughout a fill for the three experiments. Most of the LHCb data were collected at an instantaneous luminosity of $4 \times 10^{32} \, \mathrm{cm}^{-2} \, \mathrm{s}^{-1}$. The average number of collisions per bunch crossing, μ, ranges from 1.1 to 1.7 at LHCb depending on the year of data taking, whereas ATLAS operates at $\mu = 27$. The lower value of μ at LHCb improves the accuracy of detecting B mesons by decreasing the likelihood of a track being associated with the incorrect pp collision vertex. It also improves the performance of the LHCb subdetectors by decreasing their average occupancy, and reduces radiative damage to its vertex locator, which is situated very close to the beam pipe.

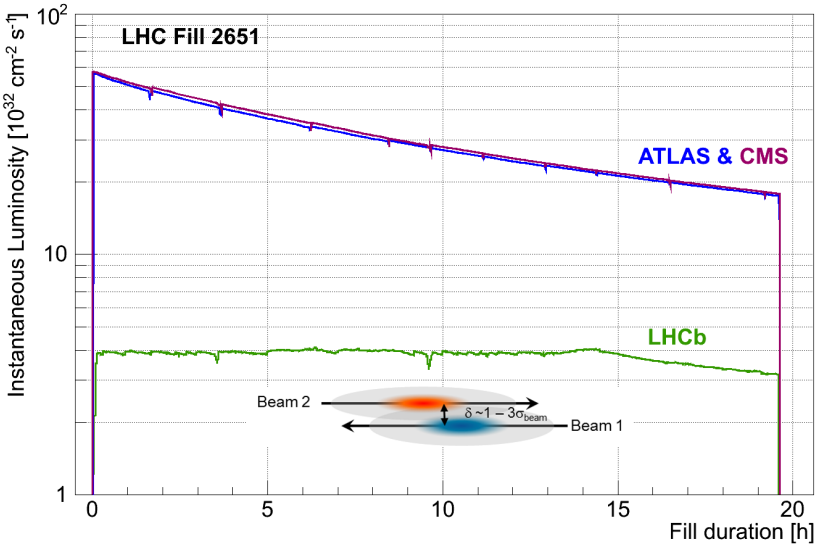

Figure 3.2: Development of the instantaneous luminosity throughout a fill at the ATLAS, CMS and LHCb experiments, reproduced from Ref. [53]. At LHCb, the luminosity is kept stable to within 5% of the desired value, $4 \times 10^{32}\,\mathrm{cm}^{-2}\,\mathrm{s}^{-1}$, for around 15 hours.

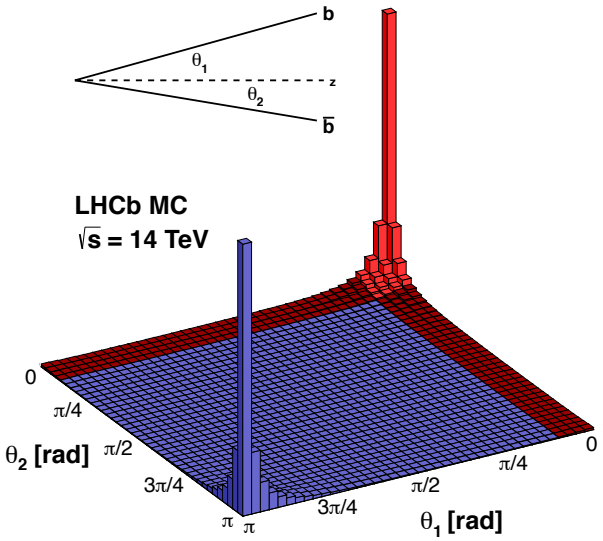

Figure 3.3: The angular distribution of $b\bar{b}$ quark pairs produced in simulated pp collisions at 14 TeV, reproduced from Ref. [54]. The region covered by the LHCb detector is shown in red.

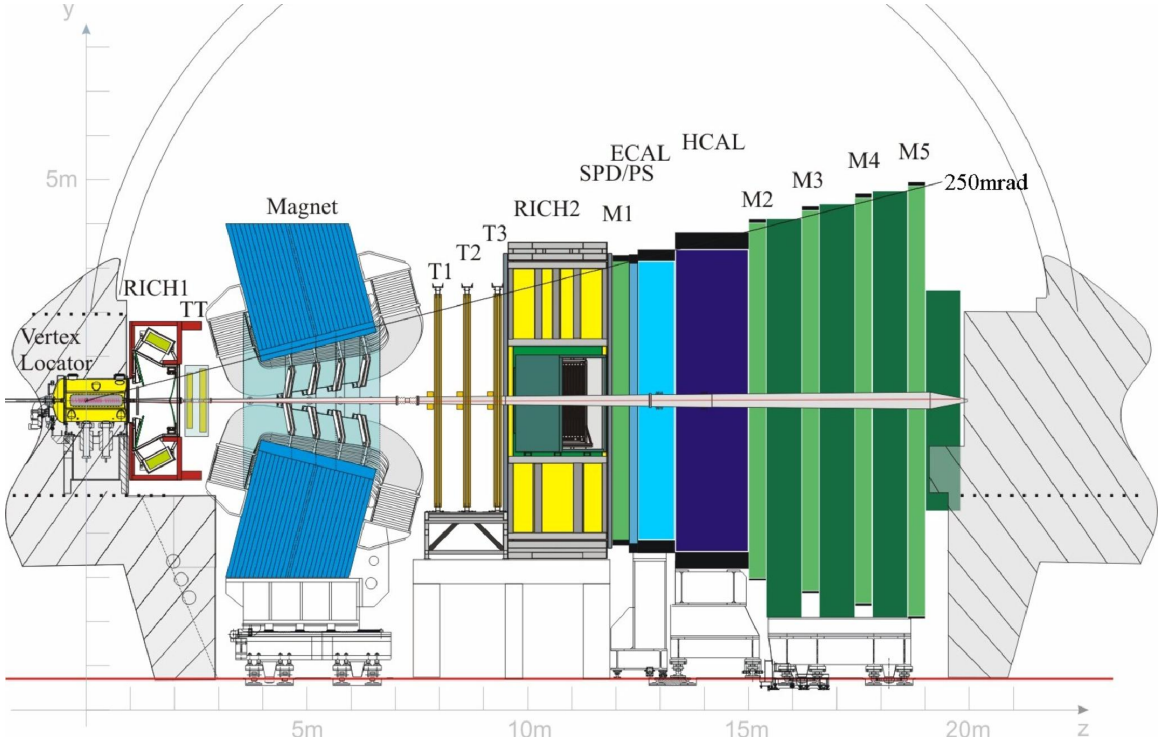

Figure 3.4: The LHCb detector, reproduced from Ref. [56].

3.1 The LHCb detector

The LHCb detector [53, 55] is designed to detect the decays of beauty and charm hadrons. The dominant mechanism for $b\bar{b}$ production at a collision energy of 13 TeV is gluon fusion, which is most likely when the interacting gluons have asymmetric momenta in the pp centre-of-mass frame. This causes the produced $b\bar{b}$ pair to be boosted along the beam direction, with both quarks very likely to be in the same forward or backward cone, as shown in Fig. 3.3. The LHCb detector is therefore arranged in the forward direction, in contrast to the cylindrical designs of the ATLAS, CMS, and ALICE detectors.

A schematic of the LHCb detector is shown in Fig. 3.4. The detector is described with respect to a right-handed coordinate system where the z-axis points along the beam line and the x and y axes point in the horizontal and vertical directions, respectively. The proton bunches collide inside the vertex locator at $z = 0$, and the detector extends to $z = 20\,\text{m}$.

Along the length of the detector, particles traverse several subdetectors:

1. The **VErtex LOcator (VELO)** locates the primary collision vertex and the decay vertex of the beauty or charm hadron;
2. **Ring Imaging Cherenkov detectors (RICH1 and RICH2)** provide information for identifying the species of charged particles;
3. The **Tracker Turicensis (TT)** locates particle tracks upstream of the magnet;
4. The **dipole magnet** bends the tracks of charged particles so that their curvature can be used to measure their momentum and charge;
5. The **tracking stations (T1–T3)** measure the positions of tracks downstream of the magnet;
6. The **calorimetry systems (SPD/PS, ECAL and HCAL)** provide particle identification information and measure deposits of energy;
7. The **muon detectors (M1–M5)** identify muons and measure their transverse momenta.

The detector covers an angular range of $10 < \theta < 300\,\text{mrad}$ in the bending plane of the magnet and $10 < \theta < 250\,\text{mrad}$ in the non-bending plane. This range captures 25% of the $b\bar{b}$ pairs produced in the pp collisions. Because the b hadrons within this range have high momenta, they typically travel around 10 mm from the primary vertex (PV) at which they are produced before decaying. They are characterised by this displacement and the large transverse momenta (p_{T}) of their decay products. These properties are detected using high-quality measurements of the vertex positions and track momenta by the VELO and tracking system. The RICH detectors and calorimeters contribute to the precise identification of the species of charged particles, which is crucial in flavour-physics analyses. To cope with the high pp collision rate, LHCb uses a fast and efficient trigger system to decide which events to store, including a

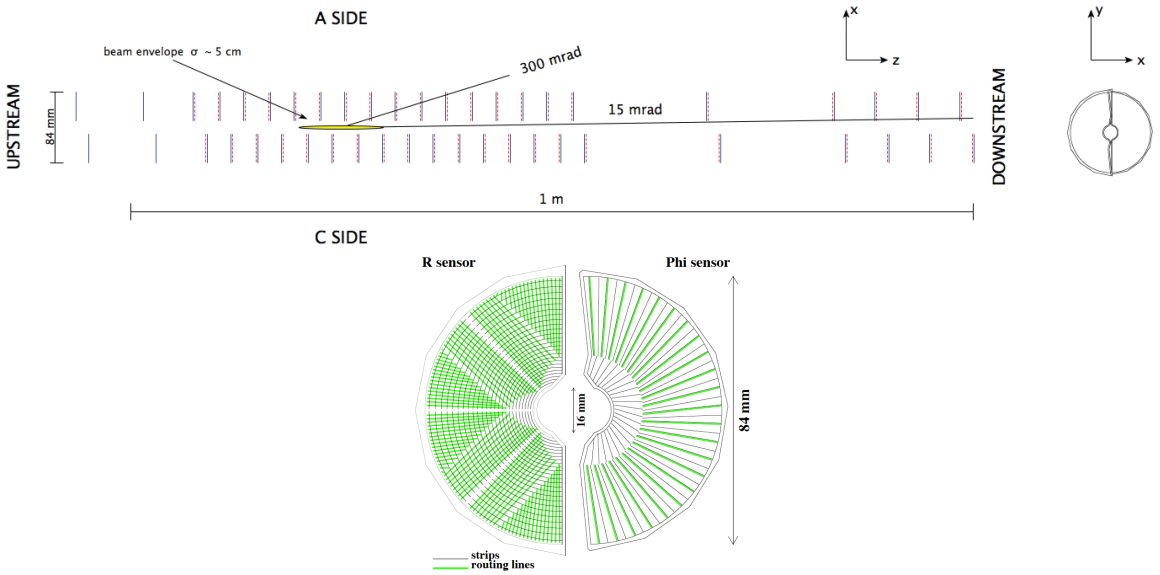

Figure 3.5: Diagrams of (top) the arrangement of the layers of the VELO detector, and (bottom) the structure of a radial (R) sensor and an angular (Φ) sensor, reproduced from Ref. [57].

hardware trigger that relies on information from the calorimeters and muon detectors and a software trigger using full detector information. The remainder of this chapter discusses each of these features in more detail.

3.2 The VELO

Processes involving b hadrons are characterised by a significant separation between the PV and the b-hadron decay vertex. Precise reconstruction of these vertices is essential for distinguishing b-hadron decays from the many other tracks coming from the pp collision. This is achieved by the VELO, which is a set of 42 semicircular silicon microstrip detectors surrounding the pp interaction region. When charged particles collide with silicon atoms, they liberate electrons and produce a detectable electrical current. The layers of the VELO alternate between between radial (R) detectors and angular (Φ) detectors. A diagram of the VELO layout and sensors is shown in Fig. 3.5.

To increase precision, the sensors are positioned just 7 mm from the beam pipe during data taking. At this proximity, the VELO would suffer huge amounts of ra-

diative damage before the beams are focussed. To avoid this damage, the VELO automatically retracts to a safe distance of 35 mm during beam injection and stabilisation and moves back towards the beam for data taking.

The recorded hits in the VELO are combined with information from the trackers to reconstruct the positions of charged tracks and vertices, as described in Sect. 3.4.

3.3 Tracking stations and magnet

In a particle physics analysis, we typically infer the presence of a particle decay by searching for a peak in the invariant-mass distribution of the final-state particles. A good invariant-mass resolution is needed to distinguish signal peaks from underlying backgrounds. The invariant mass is calculated from the momenta of the final-state tracks, and thus a good momentum resolution is required; this is achieved by the tracking system in combination with the VELO.

The arrangement of the tracking stations is illustrated in Fig. 3.6. The Tracker Turicensis (TT) is positioned upstream of the magnet, and three additional stations T1–T3, collectively referred to as the "T stations", are positioned downstream.

Silicon microstrip trackers are used in the TT and the region of the T stations closest to the beam pipe, called the Inner Tracker (IT), where the density of tracks is highest. The TT is 130 cm high and 150 cm wide, covering the full detector acceptance, while the IT is cross-shaped and is 40 cm high and 120 cm wide. The TT and each of the three IT stations are composed of four layers in a x–u–v–x structure, with the x layers positioned vertically and layers u and v positioned at angles of $\pm 5^\circ$ from the vertical. The silicon technology used is expensive, but provides a very fine spatial resolution of around 50 μm [53].

The region of the T stations further from the beam pipe is called the Outer Tracker (OT) and is made up of 5 mm-diameter straw-tubes filled with a gas mixture of argon, CO_2, and O_2. Each station is composed of four layers arranged in the same x–u–v–x structure as the silicon trackers. When a charged particle passes through the straw-

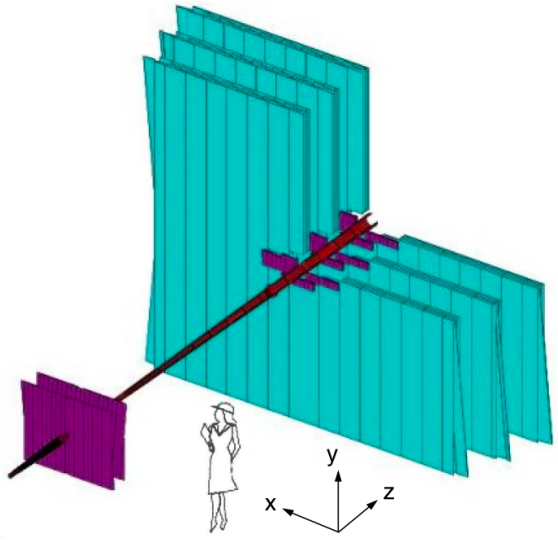

Figure 3.6: Arrangement of the tracking stations, reproduced from Ref. [55]. The Tracker Turicensis and Inner Tracker, which use silicon microstrip technology, are shown in purple. The Outer Tracker, which is made up of straw-tube modules, is shown in cyan.

tubes, it ionises the gas molecules inside, producing electrons that are detected by an anode wire at the centre. The position of the track within the tube is calculated from the drift-time taken for the electrons to reach the wire, providing a much finer precision than simply using the position of the tube. Straw-tube technology is cheaper than silicon strips and is therefore well-suited to covering the large area further from the beam. The OT achieves a drift-time below 50 ns and a spatial resolution of around 200 µm [53].

A warm (non-superconduting) dipole magnet is positioned between the TT and the T stations, and provides an integrated magnetic field of around 4 Tm. Its purpose is to deflect charged particles in the x–z plane, producing a measurable curvature from which a charged particle's momentum can be calculated. As positively and negatively charged particles are deflected in opposite directions, a charge detection asymmetry could arise from a difference in performance of the left- and right-hand sides of the detector. The direction of the magnetic field is regularly switched during data-taking to cancel out this asymmetry.

3.4 Charged-track reconstruction

The trajectories of charged particles are reconstructed from hits in the VELO, TT, and T stations. Tracks are categorised according to their route through the detector:

- **Long tracks** traverse the entire tracking system. They have the most precise momentum estimate and are therefore the most useful tracks for physics analyses.
- **Upstream tracks** pass through the VELO and TT. They are deflected out of the detector acceptance before reaching the T stations due to their low momenta.
- **Downstream tracks** only traverse the TT and T stations, and typically originate from long-lived particles such as K^0_S mesons that decay outside the VELO. While they have a slightly worse momentum resolution than long tracks, they are still useful in analyses involving long-lived intermediate particles. Around two-thirds of detected K^0_S mesons are reconstructed from downstream tracks.
- **VELO tracks** only produce hits in the VELO. They are typically large-angle or backwards tracks and are useful for reconstructing the PV.
- **T tracks** only produce hits in the T stations, and are likely to come from secondary interactions with the detector material. Their momentum is unknown, so they are of little use for physics analyses.

Figure 3.7 shows a sketch of the different track types.

Once tracks have been identified, their trajectories are fitted using a Kalman filter [59], which accounts for multiple scattering and corrects for energy loss due to ionisation of the detector material. The quality of the track is quantified by the χ^2 per degree-of-freedom of this fit. A neural network is used to remove fake tracks, which mostly originate from incorrect associations between VELO tracks and tracks in the T stations.

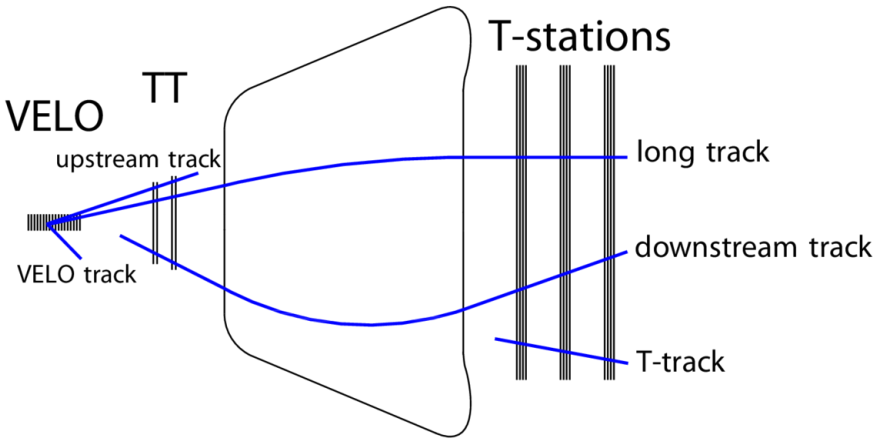

Figure 3.7: Sketch of the different types of tracks traversing the VELO, TT, and T stations, reproduced from Ref. [58].

The tracking efficiency, defined as the probability that the trajectory of a charged particle that has passed through the full tracking system is reconstructed, is greater than 96% for tracks in the momentum range $5 < p < 200\,\text{GeV}/c$ [58]. The momentum resolution of reconstructed tracks is extremely good; the relative uncertainty $\delta p/p$ varies from 0.5% at low momentum to 1.0% at high momentum, as shown in Fig. 3.8(a).

The resolution of the PV depends on the number of tracks used in its reconstruction, with more tracks providing a better resolution. Figure 3.8(b) shows the resolution in the x and y directions as a function of track multiplicity. For a PV reconstructed with 25 tracks, the resolution is 13 μm in the transverse plane and 71 μm along the beam axis [57].

The impact parameter (IP) of a track is its distance from the PV at the point of closest approach. As b hadrons tend to have a displaced decay vertex, the IP of their products is typically larger than that of particles originating from the PV. The IP resolution is inversely proportional to the p_{T} of the track, as shown in Fig. 3.8(c), and is less than 35 μm for tracks with a p_{T} greater than $1\,\text{GeV}/c$. For each track, an additional parameter, χ^2_{IP}, is calculated. This is defined as the difference in χ^2 of the PV fit with and without the inclusion of the track. This quantity behaves like

$(\mathrm{IP}/\sigma_{\mathrm{IP}})^2$, and therefore tends to be large for b-hadron decay products. Requirements on the IP and χ^2_{IP} variables are frequently used in analyses to remove contamination from prompt backgrounds.

Once the three-momentum $\mathbf{p}$ of a particle has been measured, its energy can be calculated for a given mass hypothesis m using

$$E = \sqrt{|\mathbf{p}|^2c^2 + m^2c^4}. \tag{3.3}$$

The invariant mass of an n-body combination of tracks can be calculated from

$$m^2_{\mathrm{tot}}c^4 = E^2_{\mathrm{tot}} - |\mathbf{p}_{\mathrm{tot}}|^2c^2 = \left(\sum_i^n \sqrt{|\mathbf{p}_i|^2c^2 + m_i^2c^4}\right)^2 - \left|\sum_i^n \mathbf{p}_i\right|^2 c^2. \tag{3.4}$$

The precise momentum measurements at LHCb therefore provide an excellent invariant-mass resolution. The relative mass resolution σ_m/m has been measured for various dimuon resonances, as shown in Fig. 3.8(d), and is around 0.5% for masses up to the mass of the Υ resonance.

3.5 The RICH detectors

The accurate identification of charged particles is extremely important in flavour physics, for instance to tag the flavour of B mesons or distinguish between favoured and suppressed decays. Excellent identification of charged hadrons (π, K and p) is achieved at LHCb by the two RICH detectors.

When a charged particle passes through a dielectric medium faster than the speed of light in that medium, a phenomenon known as Cherenkov radiation occurs, which is an optical analogue of a sonic boom. This results in the emission of a cone of electromagnetic radiation with an angle given by $\cos\theta = \frac{1}{n\beta}$, where n is the refractive index of the medium and β is the ratio of the particle's velocity to the speed of light in a vacuum. The relationship between θ and the particle's momentum therefore depends on its mass. Figure 3.9 shows the Cherenkov angle versus momentum for particles of different masses in C_4F_{10}, which has a refractive index $n = 1.0014$. The

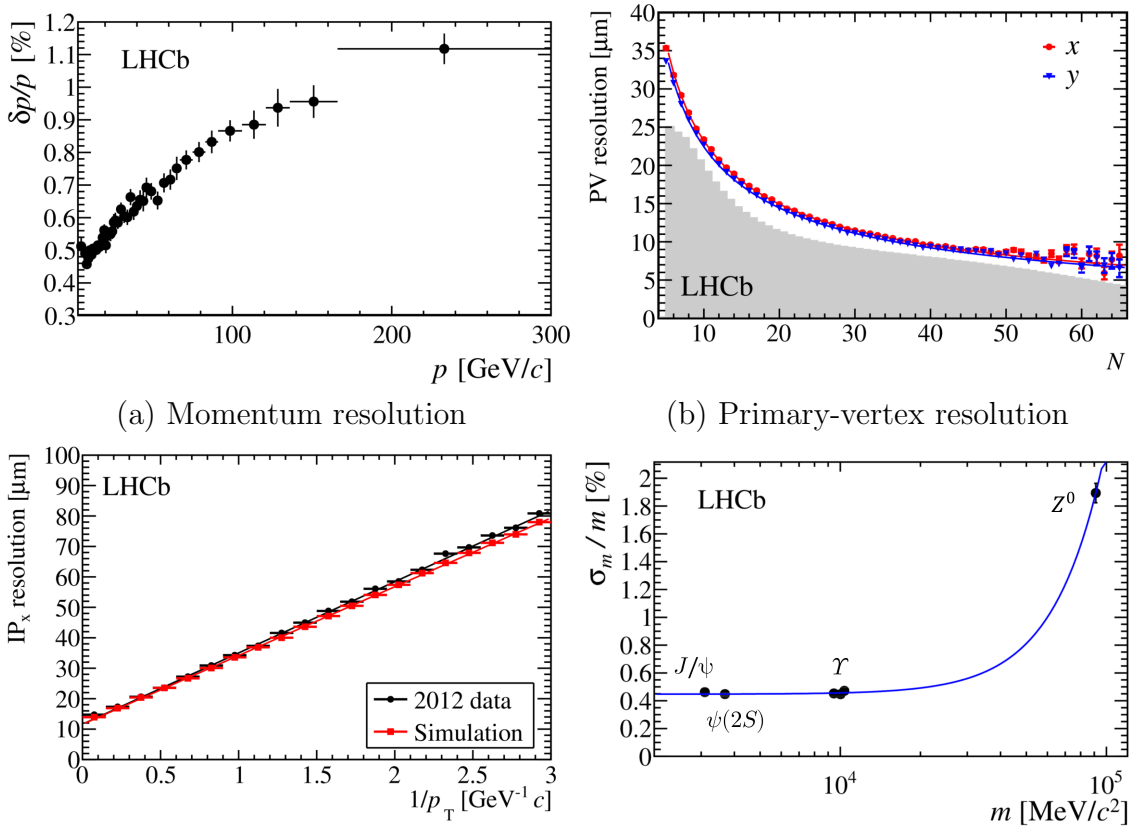

(a) Momentum resolution

(b) Primary-vertex resolution

(c) Impact-parameter resolution

(d) Mass resolution

Figure 3.8: Studies of the tracking performance at LHCb. (a) Relative momentum resolution versus momentum for long tracks in J/ψ decays [53]. (b) Primary-vertex resolution in the x and y directions as a function of track multiplicity. The grey histogram shows the resolution for all events that pass the High Level Trigger [53]. (c) Resolution of the x component of the impact parameter as a function of $1/p_{\mathrm{T}}$ in 2012 data and simulation [57]. (d) Relative mass resolution versus mass, measured for various dimuon resonances [53].

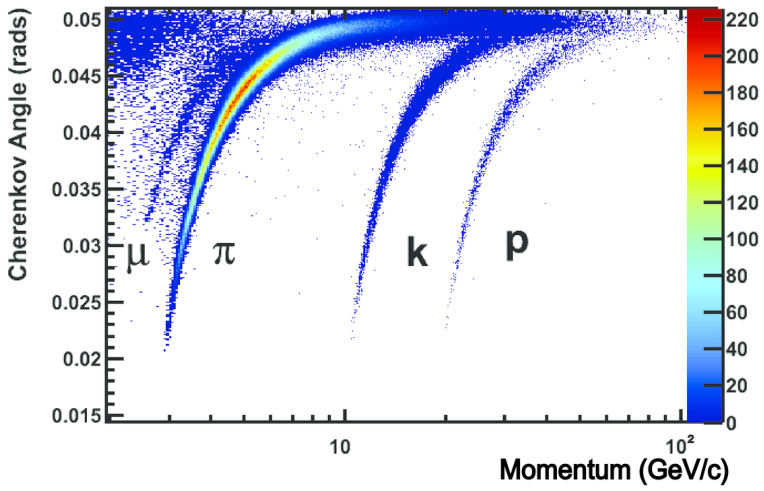

Figure 3.9: Reconstructed Cherenkov angle as a function of track momentum for different charged hadron species in the C_4F_{10} radiator of the RICH detector, reproduced from Ref. [60].

Cherenkov angle is measured from detected photons in the RICH photosensors and compared with the momentum of the track matching those hits to provide information on the track's probable species.

The RICH1 detector is located upstream of the magnet and is designed to provide particle identification in the low-momentum range $2 < p < 40\,\text{GeV}/c$. It covers the full angular acceptance of the detector and is positioned as close to the interaction point as possible to limit its volume. During Run 1, the RICH1 detector contained two radiators, C_4F_{10} and silica aerogel ($n = 1.03$). The inclusion of the aerogel was not as effective as expected, so it was removed in Run 2 to improve the efficiency by allowing a larger volume of C_4F_{10} to be used.

The RICH2 detector lies downstream of the magnet and encompasses the high-momentum range $15 < p < 100\,\text{GeV}/c$ using CF_4 ($n = 1.0005$) as a radiator. Although it covers a limited angular range of 15–200 mrad, a large proportion of the high-momentum tracks for which the RICH2 has high separation power enter this region. Both RICH detectors use mirrors to focus the Cherenkov photons into rings, which are detected by arrays of hybrid photon detectors (HPDs). The resolution of the reconstructed Cherenkov angle is 1.618 mrad in RICH1 and 0.68 mrad in RICH2 [60].

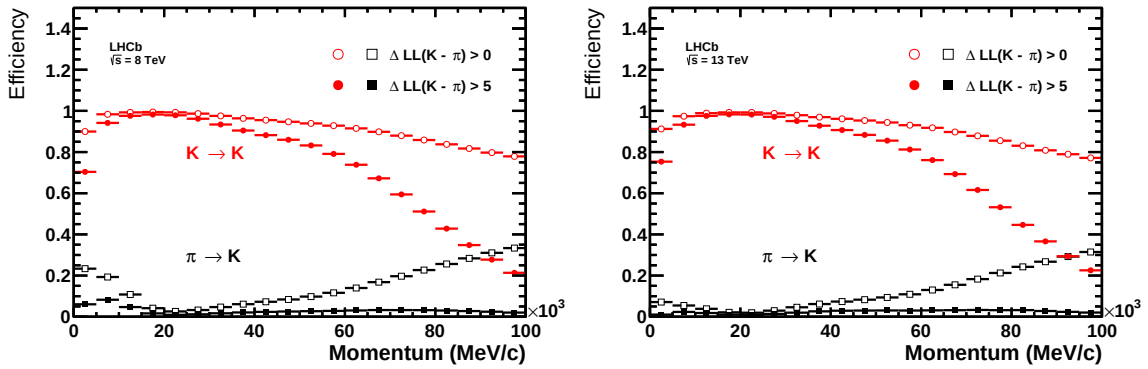

(a) 2012 data (b) 2016 data

Figure 3.10: Kaon identification efficiency (red) and pion misidentification rate (black) in data from (a) 2012 and (b) 2016 as a function of track momentum. Two different requirements on $\Delta\mathrm{LL}(K-\pi) = \log L_K - \log L_\pi$ are applied, resulting in the open and filled marker distributions. Reproduced from Ref. [61].

A fit is performed to find the likelihood L of each mass hypothesis for tracks that have passed through the RICH detectors. The difference in log-likelihood for each species X is defined as

$$\mathrm{DLL}_X = \log L_X - \log L_\pi. \tag{3.5}$$

This variable compares the likelihood of species X with that of a pion, which is the most abundant species, and is frequently used in analyses to remove backgrounds with misidentified particles. Figure 3.10 shows the kaon identification efficiency and pion misidentification rate versus momentum for two different DLL_K requirements in Run 1 and Run 2. An improvement can be seen at low momentum in Run 2 due to the removal of the aerogel.

3.6 Calorimeter

The calorimetry system serves several purposes. It provides identification for electrons, photons, and π^0 mesons, and measures their positions and energies, which are used in the reconstruction of decays with neutral final-state particles. It also provides information to the hardware trigger, which selects candidates with large transverse energies (E_T) as discussed in Sect. 3.8.

The calorimeter consists of a scintillating pad detector (SPD), a preshower (PS), an electromagnetic calorimeter (ECAL), and a hadronic calorimeter (HCAL). The SPD and PS are both made from arrays of scintillating pads and are separated by a 15 mm-thick lead converter. This setup provides separation between electrons and photons, as both species produce a signal in the PS but only charged particles produce a signal in the SPD. The energy deposition profile in the PS helps to distinguish electrons from charged pions.

The ECAL is made up of alternating layers of lead and scintillator tiles. Particles interact with the lead to produce electromagnetic showers, which are converted to UV light by the scintillator layers. The UV light is detected by photomultiplier tubes (PMTs) and used to determine the deposited energy. The length of the ECAL corresponds to 25 radiation lengths, enough for almost all of the energy in the electromagnetic showers to be deposited.

The HCAL consists of alternating layers of iron and scintillator, and operates similarly to the ECAL. It only covers 5.6 nuclear interaction lengths due to space constraints; this is sufficient for its intended purpose, which is to sample the energies of hadronic tracks for use in the hardware trigger rather than to measure their total energies.

3.7 Muon detectors

Many interesting B-meson decays have muons in their final states, which have long lifetimes in the lab frame and traverse the entire detector. The muon stations identify these muons and provide a fast measurement of their p_{T} for use in the hardware trigger. The first station, M1, is placed upstream of the calorimeter and is important for the p_{T} measurement. The stations M2–M5 are positioned downstream of the calorimeter and are interleaved with iron absorber plates to ensure that penetrating muons are the only particles to traverse all five stations. Multi-wire proportional chambers (MWPCs) are used everywhere in the muon stations, except in the inner

region of M1 where the particle flux is highest, which is equipped with gas electron multiplier (GEM) detectors.

Information from the RICH detectors, calorimeter, and muon stations is combined to calculate the likelihood and DLL of each charged-particle hypothesis: e, μ, K, π and p.

3.8 Trigger and stripping

Bunches of protons at the LHC collide at a rate of around 40 MHz, while the rate of interesting B-meson decays is only a few Hz. It is impossible to record and process all events due to limited storage capacity, detector readout speed, and computing resources, so a trigger system is employed to cherry-pick interesting events to save. The design of the trigger has been refined throughout the operation of LHCb. Figure 3.11 shows overviews of the trigger system in 2012 and 2015.

3.8.1 Hardware trigger

The first level of the trigger is the hardware trigger (L0). This reduces the event rate to around 1 MHz, the maximum frequency at which the entire detector can be read out. The L0 trigger uses information from the calorimeter and muon systems to construct hadron, photon, electron and muon candidates, which are accepted or rejected based on their transverse energy or momentum. Transverse energy is calculated in 2×2 clusters of ECAL or HCAL cells, and is defined as

$$E_{\mathrm{T}} = \sum_{i=1}^{4} E_i \sin\theta_i, \tag{3.6}$$

where E_i is the energy deposited in cell i, and θ_i is the angle between the z axis and a line connecting the cell-centre average to the average pp collision point.

Hadron candidates (`L0Hadron`) are constructed from the HCAL cluster with the largest E_{T}, which is added to the E_{T} from the matching cluster in the ECAL. Photon candidates (`L0Photon`) use the highest E_{T} ECAL cluster with one or two matching PS hits and no matching hits in the SPD. Electron candidates (`L0Electron`) use the

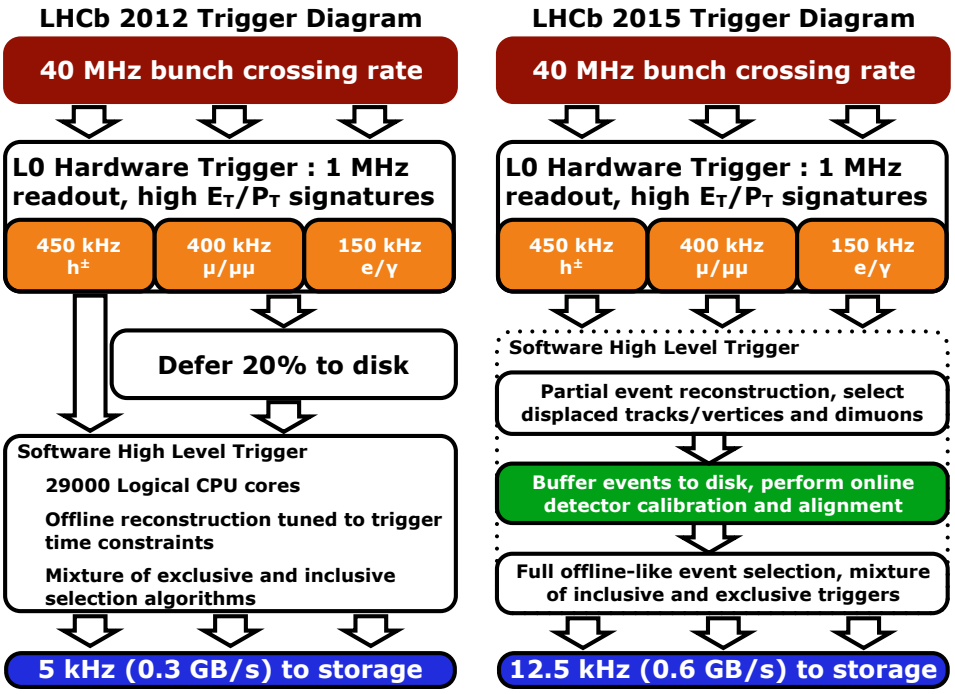

(a) 2012 (b) 2015

Figure 3.11: Overview of the trigger system in (a) 2012 and (b) 2015, reproduced from Ref. [62].

same requirements as photon candidates but must have a corresponding hit in the SPD. Events where at least one candidate has a sufficiently large E_{T} are kept.

Muon candidates (`L0Muon`) are required to have hits in all five muon stations. Events are if saved either the p_{T} of the highest-p_{T} muon track or the product of the p_{T} of the tracks with the highest and second-highest p_{T} exceeds a threshold.

In samples of reconstructed decays, the trigger decision is classified as `TOS` (Trigger On Signal) if particles in the signal decay fired the trigger, or `TIS` (Trigger Independent of Signal) if any other particles in the pp-collision event fired the trigger. The `TIS` condition is typically activated by the decay products of the other b hadron produced in the collision. In analyses of decays with hadronic final states, it is useful to require `TOS` candidates to have activated the `L0Hadron` trigger, while allowing `TIS` candidates to have activated any trigger.

3.8.2 Software trigger

The hardware trigger is followed by the High Level Trigger (HLT), which is implemented in software and uses full detector information. The HLT is divided into two sub-levels, HLT1 and HLT2. HLT1 uses a partial reconstruction of the tracks and vertices in the VELO. Candidates that do not involve muons are kept if they contain at least one track consistent with originating from a displaced beauty or charm decay vertex, *i.e.* with a high p_{T} and χ^2_{IP}. Candidates that fired the `L0Muon` trigger are kept if they contain a displaced muon track or a dimuon combination.

The output of HLT1 is a few tens of kHz. This is low enough for HLT2 to run a full event reconstruction and perform a more detailed search for various decays of interest. This produces the final output of a few kHz, which is written to permanent storage for further offline processing. Around 40% of the HLT2 output comes from "topological" trigger decisions, which select candidates containing a secondary vertex consistent with being a b-hadron decay to at least two charged final-state tracks. Combinations of two, three and four tracks with a sufficiently small distance-of-closest-approach (DOCA) are considered. These candidates are accepted or rejected based on the results of a multivariate classifier [63] whose inputs include the p_{T}, χ^2_{IP} and DOCA of the tracks.

Improvements to computing infrastructure and reconstruction algorithms between Run 1 and Run 2 allowed the output rates of HLT1 and HLT2 to be doubled, and more time to be spent processing each event in HLT2. The HLT2 event reconstruction was improved from a simplified version of the offline reconstruction to a full offline-quality reconstruction using real-time detector alignment and calibration and full PID information. These trigger improvements significantly increased the efficiency of recording useful events. In combination with the increased collision energy in Run 2, which led to a corresponding increase in $b\bar{b}$ production cross-section, this means that the Run 2 data samples contain around 2.5 times as many B-meson decays per fb^{-1} as the Run 1 samples.

3.8.3 Stripping

During offline processing, reconstructed candidates are categorised into families of similar decays in a process known as "stripping". Some sensible loose selection requirements are applied to remove background events, reducing the processing time and storage requirements for subsequent analyses. The full data set is periodically "restripped" to add new decay categories and improve existing stripping selections. The stripped samples form the starting point for LHCb physics analyses, which typically apply more sophisticated selection requirements to the samples.

3.9 Simulation

Samples of simulated signal and background events play an important role in particle physics analyses. In this thesis, simulated samples are primarily used in three ways:

1. Training multivariate classifiers to select signal decays;

2. Finding probability density functions to describe the invariant-mass spectra of signal and background decays;

3. Calculating selection efficiencies and correction factors.

The Pythia [64] package with a specific LHCb configuration [65] is used to generate pp collisions that produce $b\bar{b}$ pairs. One b quark is randomly selected to decay to a user-specified final state, while the other decays according to a list of all possible b-hadron decays scaled by their branching fractions. These decays are simulated by EvtGen [66] with final-state radiation generated using Photos [67]. The final-state tracks of the user-specified decay are generated within the acceptance of the LHCb detector. The Geant4 toolkit [68] is used to model the interactions of the decay products with the detector, as described in Ref. [69]. The simulated detector response is processed to match the format of the real detector response, which is then treated in the same way as real data, the only difference being that some useful generator-level information, including the true identity and momentum of each particle, is stored.

In the simulated $B^0 \to DK^{*0}$ decays used in this thesis, the B^0 meson is forced to decay to the final state $DK^+\pi^-$ via the $K^*(892)^0$ resonance. Samples are produced for each magnet polarity and D-meson final state, and for at least one year in each period of data taking. In the D-meson final states with three or four particles, the D-meson decay products are generated uniformly across phase space.

Chapter 4

Selection and parametrisation of $B^0 \to DK^{*0}$ decays with two- and four-body D-meson final states

The following two chapters describe an analysis of $B^0 \to DK^{*0}$ decays with the D meson reconstructed in the two-body final states $K^+\pi^-$, π^+K^-, K^+K^-, and $\pi^+\pi^-$, and the four-body final states $K^+\pi^-\pi^+\pi^-$, $\pi^+K^-\pi^+\pi^-$, and $\pi^+\pi^-\pi^+\pi^-$. The aim of the analysis is to measure the *CP* observables listed in Sect. 2.6.4, which can be used to constrain the value of the CKM angle γ. This work is published in Ref. [50].

The measurement uses $5\,\text{fb}^{-1}$ of pp collision data collected by the LHCb experiment from 2011–2012 and 2015–2016 for all D-meson decays except $D \to \pi^+\pi^-\pi^+\pi^-$, for which only the $2\,\text{fb}^{-1}$ of data collected from 2015–2016 are used. This is because there was no stripped sample for decays of this type in the 2011–2012 data at the time of the analysis.

The analysis strategy is as follows:

1. Select $B^0 \to DK^{*0}$ candidates and split them into categories according to **mode** (D-meson final state), **flavour** (B^0 or $\overline{B}^0$, tagged according to the charge of the kaon from the decay of the K^{*0} meson) and **data-taking period** (Run 1, comprising 2011 and 2012 data, and Run 2, comprising 2015 and 2016 data).

2. Develop a model to describe the invariant-mass distributions of the selected candidates.

3. Perform a simultaneous fit to the invariant-mass distribution in each category, including corrections for any experimental effects such that the *CP* observables are measured directly from the fit.

4. Evaluate the systematic uncertainties.

Section 4.1 outlines the candidate selection strategy. Section 4.2 describes the invariant-mass model, and Sect. 4.3 presents the results of the invariant-mass fit. The measurement of the *CP* observables is detailed in Chap. 5.

Throughout this discussion, the labels $K\pi(\pi\pi)$ refer to modes involving the decay $D \to K^{\pm}\pi^{\mp}(\pi^+\pi^-)$ where the kaons from the decays of the D and K^{*0} mesons have the same charge; these are the favoured ADS modes, which have larger yields than all other modes. Conversely, the labels $\pi K(\pi\pi)$ refer to the suppressed ADS modes, where the kaons from the decays of the D and K^{*0} mesons have opposite charges. The GLW modes $D \to K^+K^-$, $\pi^+\pi^-$, and $\pi^+\pi^-\pi^+\pi^-$ are labelled KK, $\pi\pi$, and 4π, respectively.

4.1 Candidate selection

4.1.1 Reconstruction and trigger requirements

Candidate $B^0 \to DK^{*0}$ decays are formed offline and stored in a centrally processed data set during stripping. Some loose requirements are applied to the stripping samples to reduce the size of the data set before storage, including thresholds on the momentum, transverse momentum, and track-fit quality of all final-state particles.

The reconstruction begins with the final-state tracks and proceeds up the decay chain. A sketch of a $B^0 \to DK^{*0}$ decay is shown in Fig. 4.1. The candidate K^{*0} meson is reconstructed from a $K^+\pi^-$ pair, and the candidate D meson is reconstructed in the two- and four-body final states of interest. The K^{*0} and D mesons must both have a high p_{T}, a good-quality vertex fit, a significant separation from the PV, and a distance-of-closest-approach of no more than 0.5 mm between their decay products.

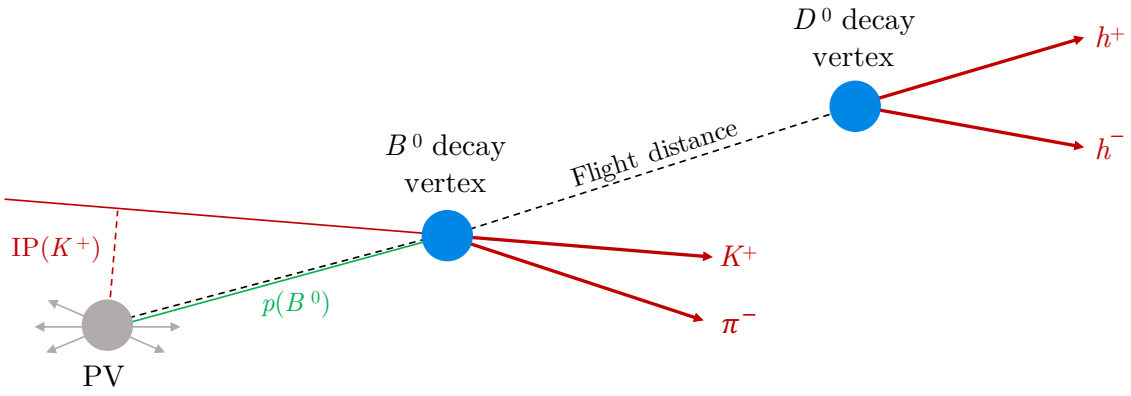

Figure 4.1: Topology of a $B^0 \to D(h^+h^-)K^+\pi^-$ decay. The primary vertex (PV) and decay vertices of the B^0 and D mesons are well separated. Red lines indicate final-state tracks, which can be extended backwards to calculate the impact parameter (IP), as shown for the K^+ meson. Black dashed lines show the trajectories of intermediate particles. These may not point in exactly the same direction as the momentum of the particle, shown by a green line for the B^0 meson. The cosine of the angle between the momentum and trajectory vectors is called the direction angle (DIRA).

The candidate B^0 meson is reconstructed from the K^{*0}-meson and D-meson candidates and must have a p_{T} greater than 5 GeV/c, a lifetime greater than 0.2 ps, and a good-quality vertex fit. Only candidates with invariant masses in the range 4750–6000 MeV/c^2 are retained.

The DecayTreeFitter framework [70] is used to improve the resolution of the B^0-meson invariant-mass distribution using knowledge of the kinematics of the decay. The decay chain is refit with the mass of the D meson fixed to its known value, and the momentum vector of the B^0 meson constrained to be parallel to a vector connecting the PV to its decay vertex; this provides a new invariant-mass variable for each reconstructed particle. The B^0-meson invariant-mass distributions discussed in this analysis are the refit version, unless otherwise stated.

Selected candidates are required to have activated a particular set of trigger conditions. At the hardware level (L0), candidates must satisfy either `L0_Hadron_TOS`, meaning that a signal particle deposited a significant amount energy in the hadron calorimeter, or `L0_Global_TIS`, meaning that a non-signal particle satisfied any hardware trigger requirement. At the software level, candidates must satisfy a HLT1

condition where at least one particle in the signal decay has a high p_{T} and χ^2_{IP}. In HLT2, candidates must have activated a "topological" trigger, where a multivariate algorithm has identified a secondary vertex in the signal decay that is consistent with being a two-, three- or four-body b-hadron decay vertex.

After the stripping stage and trigger requirements, a significant amount of background made up of random tracks resembling $B^0 \to DK^{*0}$ decays remains; this is known as "combinatorial background". The sample is also contaminated with various "physics backgrounds" from specific b-hadron decays. A set of selection requirements is applied to remove background events while retaining as much signal as possible.

The purity of the reconstructed D-meson and K^{*0}-meson candidates is greatly improved by removing candidates with invariant masses far from the known masses of these mesons. Candidate D mesons are selected within $\pm 25\,\mathrm{MeV}/c^2$ of the known D-meson mass; this encompasses almost the entire D-meson mass peak, which has a width of approximately $8\,\mathrm{MeV}/c^2$ due to the finite detector resolution. A larger selection window of $\pm 50\,\mathrm{MeV}/c^2$ is used for the K^*-meson candidates, as the $K^*(892)^0$ resonance has a width of $47.3\,\mathrm{MeV}/c^2$ [71]. Figure 4.2 shows these cuts overlaid on the invariant-mass spectra of the reconstructed D and K^{*0} mesons at the output of the stripping and after the trigger requirements. The invariant-mass requirements on the D and K^{*0} mesons select 97% and 69% of true signal candidates, respectively.

The $K^+\pi^-$ final state used to reconstruct the K^{*0} meson can appear in many other resonant and nonresonant combinations; this can be seen from the invariant-mass spectrum in Fig. 4.2(b), which covers a large range and contains multiple peaks. Many non-K^{*0}-meson decays remain in the data sample even after the invariant-mass cut. The purity is improved by exploiting the fact that the K^{*0} meson has spin 1 and is produced in a scalar $\to$ vector–scalar decay. Conservation of angular momentum requires that the K^{*0} meson be produced with a helicity of zero, giving its products a distinctive momentum distribution in its rest frame. In decays containing a true K^{*0} resonance, the cosine of the helicity angle θ^*, defined as the angle between the momentum of the K^+ meson in the rest frame of the K^{*0} meson and the momentum of

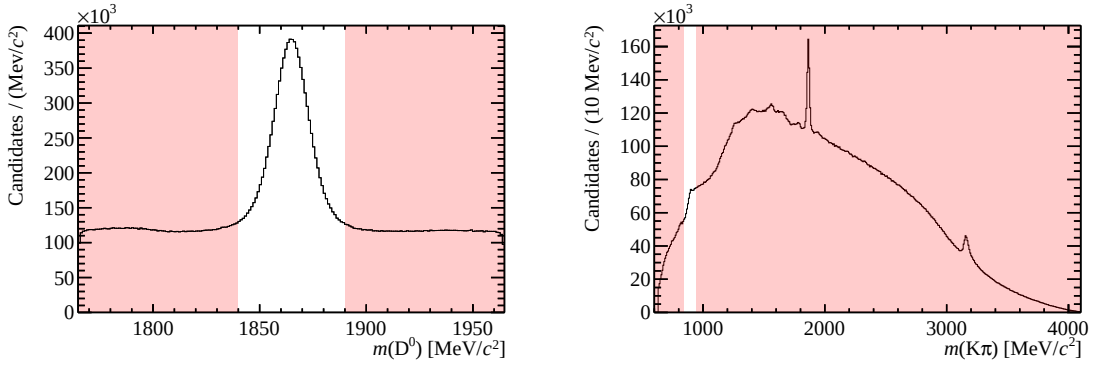

(a) D meson (b) K^{*0} meson

Figure 4.2: Invariant-mass distributions of (a) the reconstructed D meson and (b) the reconstructed K^{*0} meson in candidates from the output of the stripping that have passed the trigger requirements. Regions rejected by the invariant-mass cuts are highlighted in red.

the K^{*0} meson in the rest frame of the B^0 meson, has a parabolic distribution centred at zero. Figure 4.3 compares the $\cos(\theta^*)$ distributions of signal and background samples. Only candidates with $|\cos(\theta^*)| > 0.4$ are selected, which removes 60% of the background with a fake K^{*0} meson while retaining 93% of signal candidates.

The choice of invariant-mass and helicity-angle requirements for the K^{*0} meson is motivated by the need to use the coherence factor κ determined in Ref. [45], which is calculated for the specific region of kinematic phase space used here.

4.1.2 Multivariate analysis with a boosted decision tree

Signal candidates and combinatorial background can be separated using variables that have different distributions in signal and background decays. When these distributions have a large degree of overlap, a multivariate selection exploiting correlations between the variables is more powerful than a simple cut-based selection. One way to create such a selection is training a boosted decision tree (BDT).

A decision tree takes a set of variables from "training samples" of known signal and background events and constructs an algorithm to label events as signal-like or background-like. Figure 4.4 shows a typical decision tree structure. The algorithm splits the training data into subsets based on the value of one of the variables in a

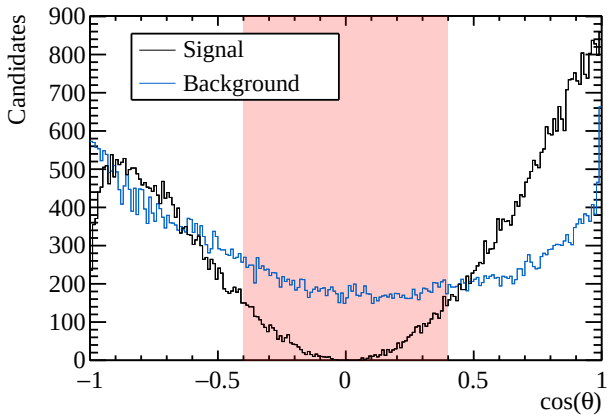

Figure 4.3: The cosine of the helicity angle of the K^{*0} meson in a sample of simulated signal events and a background-rich sample of data taken from the upper sideband of the B^0-meson invariant-mass ($m(B^0) > 5800\,\text{MeV}/c^2$). The region rejected by the requirement $|\cos(\theta^*)| > 0.4$ is highlighted in red.

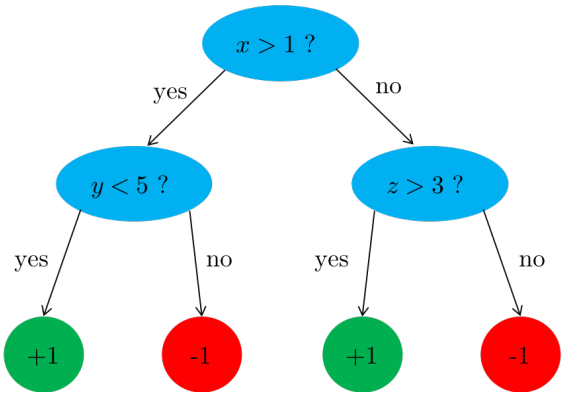

Figure 4.4: An example of the structure of a decision tree. At each blue node, the sample is split based on the value of a variable. At the red and green leaves, events are tagged as signal-like and assigned a value of $+1$, or as background-like and assigned a value of -1.

way that optimises separation between signal and background. This decision forms the "branches" of the tree, and is repeated for more variables for each subset up to a specified depth, forming a flowchart-like structure. The nodes at the end of the flowchart, called "leaves", are tagged as signal leaves (with a value of $+1$) or background leaves (with a value of -1).

While a single decision tree is unlikely to be reliable, classification algorithms that construct a weighted average over many trees perform significantly better. One method for training multiple trees is "gradient boosting", where misclassified events

in each tree are given a greater weight ("boosted") before the next tree is trained. The resultant algorithm assigns a BDT response value between -1 and $+1$ to an event, where -1 represents a purely background-like event and $+1$ represents a purely signal-like event. The user can discard events with a response below some chosen threshold, keeping only signal-like events.

BDT setup

Five gradient boosted decision trees are trained: one for the two-body ADS modes, one for the four-body ADS modes, and one for each of the GLW modes. Simulated $B^0 \to DK^{*0}$ decays are used as signal training samples, and data from the upper sideband of the B^0-meson invariant mass ($m(B^0) > 5800\,\mathrm{MeV}/c^2$) are used as background samples; this region is chosen to be outside the range used in the invariant-mass fit so that the data used to train the BDTs are independent of the data to be analysed. Both samples are required to have passed the requirements discussed in Sect. 4.1.1 so that they resemble the signal and background decays that would end up in the selected data set. The samples are randomly split in half, with one half used to train the BDTs and the other used to test their performance.

Table 4.1 lists the variables used in the BDTs, and Fig. 4.5 compares the distributions of the signal and background samples in the $K\pi$ mode. The chosen variables are based on those used for a BDT in Ref. [44] with a few updates, notably the inclusion of the p_T-asymmetry variable. This is defined as $({p_\mathrm{T}}^B - {p_\mathrm{T}}^\mathrm{cone})/({p_\mathrm{T}}^B + {p_\mathrm{T}}^\mathrm{cone})$, where ${p_\mathrm{T}}^B$ is the p_T of the candidate B^0 meson, and ${p_\mathrm{T}}^\mathrm{cone}$ is the scalar sum of the p_T of all other tracks in a cone around the candidate. The p_T asymmetry is a measure of the isolation of the B^0 meson and is a powerful discriminating variable.

The other BDT variables are:

- The direction angle (DIRA) of the B^0 meson, defined as the angle between its momentum vector and a vector connecting the PV to its decay vertex;
- The χ^2_IP of various tracks, defined as the difference in χ^2 of the PV fit with and

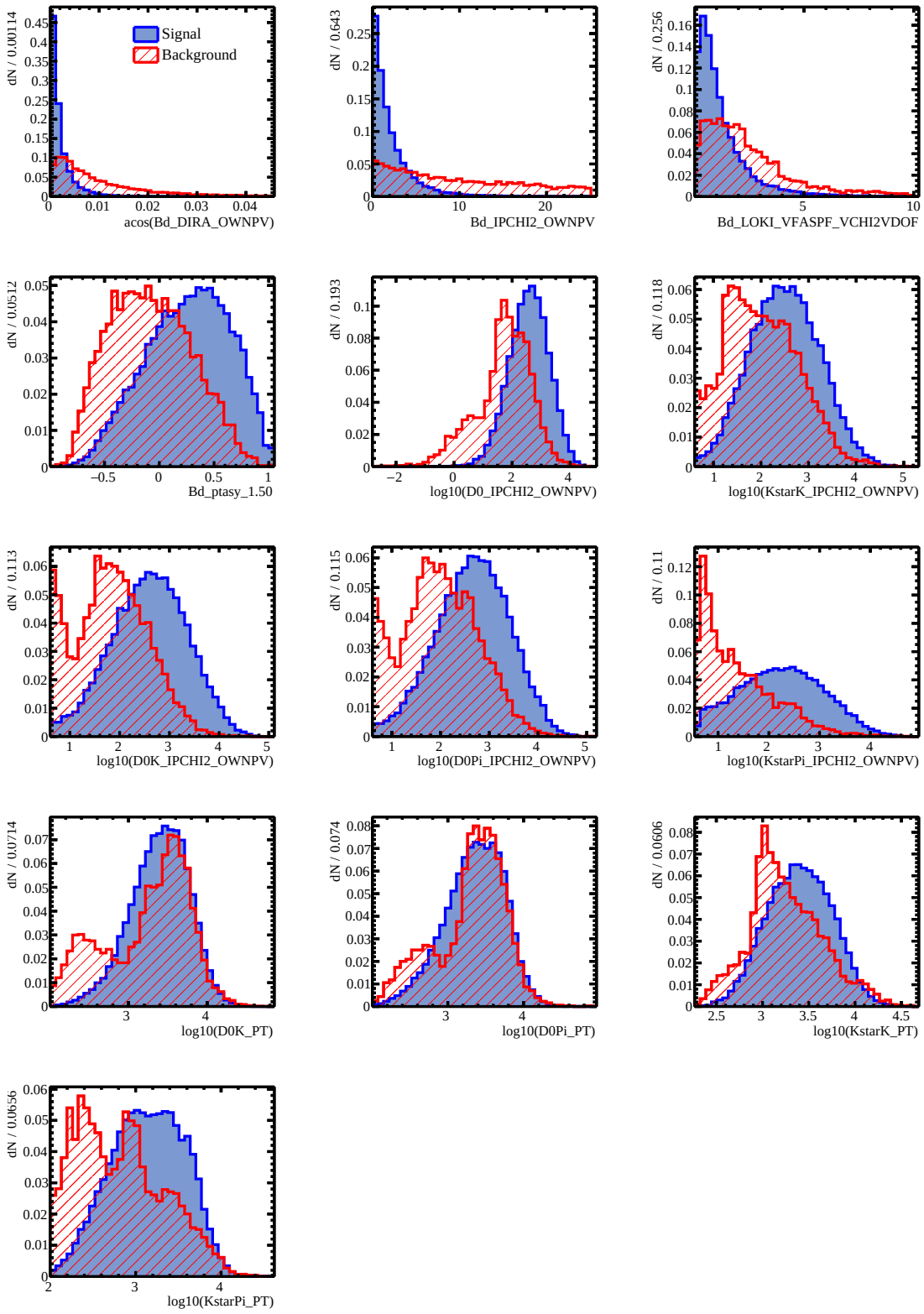

Figure 4.5: Distributions of the boosted decision tree variables in the signal (blue) and background (red) training samples for the $K\pi$ mode.

Table 4.1: Variables used in the boosted decision trees. All variables are used for two-body D-meson decays, whereas only variables in black are used for four-body D-meson decays.

Variable	Description
acos(Bd_DIRA_OWNPV)	Direction angle of B^0 meson
Bd_IPCHI2_OWNPV	χ^2_{IP} of B^0 meson
Bd_LOKI_VFASPF_VCHI2VDOF	Vertex-fit χ^2 / degrees-of-freedom of B^0 meson
Bd_ptasy_1.50	p_{T} asymmetry of B^0 meson
log10(D0_IPCHI2_OWNPV)	χ^2_{IP} of D meson
log10(D0_h1_IPCHI2_OWNPV)	χ^2_{IP} of a D-meson product
log10(D0_h2_IPCHI2_OWNPV)	χ^2_{IP} of other D-meson product
log10(KstarK_IPCHI2_OWNPV)	χ^2_{IP} of kaon from K^{*0} meson
log10(KstarPi_IPCHI2_OWNPV)	χ^2_{IP} of pion from K^{*0} meson
log10(D0_h1_PT)	p_{T} of a D-meson product
log10(D0_h2_PT)	p_{T} of other D-meson product
log10(KstarK_PT)	p_{T} of kaon from K^{*0} meson
log10(KstarPi_PT)	p_{T} of pion from K^{*0} meson

without that track;

- The transverse momenta of the final-state particles.

Some variables are transformed by taking their logarithm in order to improve the signal-background separation. The BDTs for the two-body modes use the p_{T} and χ^2_{IP} of the D-meson decay products, whereas these variables are not included in the BDTs for the four-body modes; this avoids significant distortions to the phase-space distribution of the final-state particles.

Figure 4.6 shows the distributions of the BDT response in the training and testing samples in the $K\pi$ mode. A difference between the responses of the samples would indicate that the BDT is too closely tuned to small fluctuations in the training samples; no such evidence of overtraining is seen. The signal and background responses are well separated, which indicates that the BDT has a high separation power.

Choice of BDT selection

To find the optimal BDT response at which to make a cut, the invariant-mass fit described in Sect. 4.2 is applied to data candidates at a range of different BDT cuts. For each cut, the signal yields in the favoured modes are measured in a region

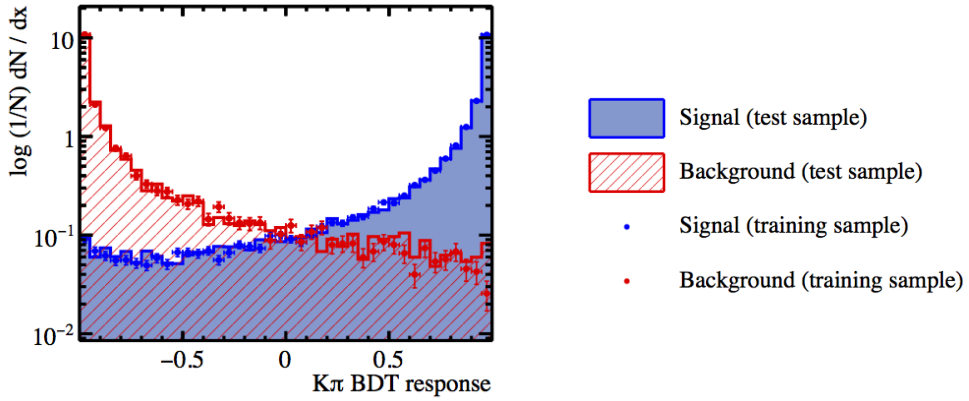

Figure 4.6: BDT response in signal and background samples for the favoured $D \to K\pi$ mode, shown on a logarithmic scale. The responses are consistent between the training and testing samples, indicating the absence of overtraining.

$\pm 50\,\text{MeV}/c^2$ around the known mass of the B^0 meson, while the signal yields in all other modes are blinded to avoid any bias to the results. The expected values of the ratios $\mathcal{R}_{CP}$, $\mathcal{R}_{\text{ADS}}^{\pi K(\pi\pi)}$ and $\mathcal{R}_{CP}^{4\pi}$ are calculated from their definitions in Eqs. 2.33 and 2.38 using the LHCb averages for r_{B^0}, δ_{B^0}, and γ [24] and are used to extrapolate the signal yield S in each mode from the favoured-mode yields.

The combinatorial background yield B in the B^0-meson mass region in each mode is measured from the fit. An estimate of the signal significance, $S/\sqrt{S+B}$, is plotted against the BDT cut; plots for the KK mode are shown in Fig. 4.7. A cut that optimises the significance in both Run 1 and Run 2 is chosen for each mode. The optimal requirements for the πK and $\pi K\pi\pi$ modes are used for the $K\pi$ and $K\pi\pi\pi$ modes, respectively; this ensures that the selection efficiency cancels out when determining ratios between the suppressed and favoured ADS-mode yields. Table 4.2 gives the chosen cuts and their efficiencies.

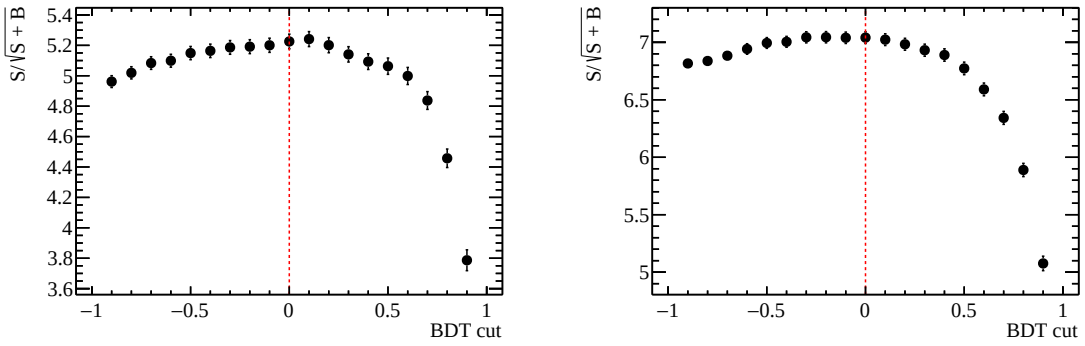

(a) Run 1 (b) Run 2

Figure 4.7: Predicted signal significance versus BDT requirement in the KK mode for the two running periods. The red dashed lines indicate the optimal cut.

Table 4.2: Requirements on the BDT response used in the candidate selection for each D-meson mode. The signal and background efficiencies are also shown.

***D* mode**	**BDT cut**	**Signal (%)**		**Background (%)**	
		Run 1	Run 2	Run 1	Run 2
πK	0.0	90	91	12	10
KK	0.0	89	91	12	11
$\pi\pi$	0.4	84	87	5	4
$\pi K\pi\pi$	0.0	90	95	8	7
4π	0.7	n/a	86	n/a	2

4.1.3 Particle identification requirements

The selection requirements discussed so far are almost identical for each of the D-meson final states. It is therefore essential to apply a particle identification (PID) selection that distinguishes between final-state kaons and pions in order to remove cross-feed between different D modes, particularly contamination from the favoured modes in the lower-yielding modes.

The PID selection uses the DLL_K variables from the RICH detectors, defined in Eq. 3.5. Kaons from the decay of the D meson are required to satisfy $\mathrm{DLL}_K > 1$, and pions from two-body D-meson decays are required to satisfy $\mathrm{DLL}_K < -1$. These non-overlapping requirements ensure that that no candidate can appear in more than one D-meson-decay category. In the four-body ADS modes, the two pions with the opposite sign to the kaon must satisfy $\mathrm{DLL}_K < -1$; this reduces cross-feed from the favoured mode into the suppressed mode. The background $D \to K^{\pm}K^{\mp}K^{+}\pi^{-}$ has a very low branching fraction, so no PID cut on the same-sign pion is needed. In the 4π mode, a requirement of $\mathrm{DLL}_K < -1$ is applied only to the two pions with the opposite sign to the kaon from the K^{*0}-meson decay in order to remove cross-feed from the favoured ADS mode.

It is also important to correctly identify the decay products of the K^{*0} meson, as the charge of the kaon tags the flavour of the B meson. The kaon is required to satisfy $\mathrm{DLL}_K > 5$, and the pion is required to satisfy $\mathrm{DLL}_K < -1$. The stringent requirement on the kaon reduces background from misidentified $B^0 \to D\pi^{+}\pi^{-}$ decays.

4.1.4 Peaking physics backgrounds

Several backgrounds arise from decays that have the same or similar topology to the signal decay. In some cases, particles in the decay chain are missed or incorrectly identified during reconstruction. These backgrounds appear as peaking structures in the B^0-meson invariant-mass distribution and can therefore affect the measurement of the signal yield; it is important to either reduce them to negligible levels or model

them in the invariant-mass fit. Table 4.3 lists the backgrounds considered in this analysis and gives the strategy employed to deal with each. This section discusses each background in more detail.

Table 4.3: Peaking physics backgrounds considered in this analysis. Each background is either modelled in the invariant-mass fit, removed with a veto, used to assign a systematic uncertainty, or ignored if sufficiently small.

Background decay	Description	Strategy
$\overline{B}{}^0_s \to DK^{*0}$	Same final state as signal	Fit
$B^0 \to D^*K^{*0}$	Partially reconstructed	Fit
$\overline{B}{}^0_s \to D^*K^{*0}$	Partially reconstructed	Fit
$B^+ \to DK^+\pi^-\pi^+$	Partially reconstructed	Fit
$B^0 \to D\pi^+\pi^+$	Misidentified pion	Fit
$B^0 \to h^+h'^-K^{*0}$	Charmless background	Veto & systematic
$B^0 \to D(K\pi)K^{*0}$	Favoured-to-suppressed cross-feed	Veto
$B^+ \to DK^+$	Combined with random pion	Veto
$B^0_{(s)} \to D^-_{(s)}h^+$	Same final state as signal	Veto
$\Lambda^0_b \to Dph$	Misidentified proton	Ignore
$\Lambda^0_b \to \Lambda^+_c(pK\pi)h$	Misidentified proton	Ignore

Decays of B^0_s mesons

The final state DK^{*0} is accessible to B^0_s mesons. As these mesons contain a strange quark, the B^0_s meson decays to $D\overline{K}{}^{*0}$ and the $\overline{B}{}^0_s$ meson decays to DK^{*0}, so decays from $\overline{B}{}^0_s$ mesons contaminate the sample of B^0 mesons, and vice versa. These decays are of little interest, as they are not expected to exhibit significant *CP* violation with the current data sample size. However, they have large yields in all but the favoured modes and must be accounted for in the invariant-mass fit. They appear as a peak at the mass of the B^0_s meson, which is $87.26\,\mathrm{MeV}/c^2$ larger than the mass of the B^0 meson [71].

Partially reconstructed backgrounds

A large background comes from $B^0 \to D^*K^{*0}$ and $\overline{B}{}^0_s \to D^*K^{*0}$ decays, where the D^* meson decays via $D^* \to D\gamma$ or $D^* \to D\pi^0$. The reconstruction efficiency for neutral

particles with the LHCb detector is low, so it is not practical to search for these decay products; the D^*K^{*0} final state is hence incorrectly reconstructed as DK^{*0}. This background is irreducible due to its similarity to the signal decay. It has a distinctive invariant-mass structure below the mass of the B^0 meson, as shown in Fig. 4.8, and is modelled in the fit as discussed in Sect. 4.2.4.

A background from partially reconstructed $B^+ \to DK^+\pi^-\pi^+$ decays with a missed π^+ meson also contaminates the low-mass region. The modelling of this background is discussed in Sect. 4.2.5.

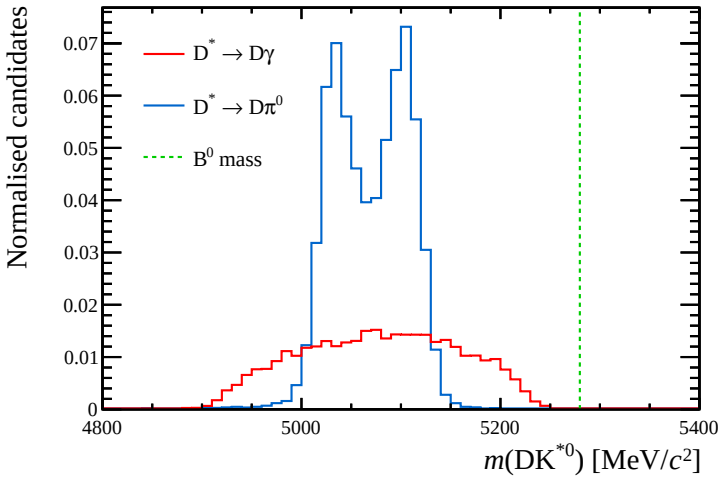

Figure 4.8: Invariant-mass distributions of partially reconstructed simulated $B^0 \to D^*(D\gamma)K^{*0}$ decays (red) and $B^0 \to D^*(D\pi^0)K^{*0}$ decays (blue), which contaminate the low-mass region in data. The green dashed line indicates the known mass of the B^0 meson.

Misidentified $B^0 \to D\pi^+\pi^-$ background

The decay $B^0 \to D\pi^+\pi^-$ can be reconstructed as $B^0 \to DK^{*0}$ if one of the pions is misidentified as a kaon. Although this background is reduced by the PID requirement on the kaon, a small contamination remains in the selected sample. Figure 4.9 shows the distributions of simulated $B^0 \to D\pi^+\pi^-$ events before and after the PID cut. This background peaks above the mass of the B^0 meson due to the extra mass incorrectly assigned to the misidentified pion, and is modelled in the invariant-mass fit as discussed in Sect. 4.2.6.

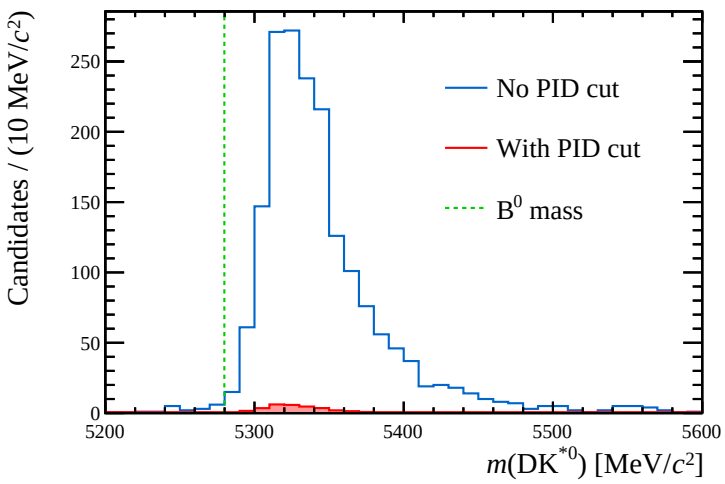

Figure 4.9: Invariant-mass distributions of misidentified simulated $B^0 \to D\pi^+\pi^-$ events before (blue) and after (red) a PID requirement of $\mathrm{DLL}_K > 5$ is applied to the misidentified pion. The green dashed line indicates the known mass of the B^0 meson.

Charmless background

A potential background comes from $B^0 \to h^+h'^-K^{*0}$ and $B^0 \to h^+h'^-\pi^+\pi^-K^{*0}$ decays that do not proceed via an intermediate D meson, known as "charmless" decays. Charmless decays form a particularly dangerous background as they peak at the mass of the B^0 meson, overlapping with true signal events. This background is reduced by placing a requirement on the flight-distance significance (FDS) of the D meson, defined as

$$\mathrm{FDS} = \frac{z_D - z_B}{\sqrt{\sigma^2_{z_D} + \sigma^2_{z_B}}}, \tag{4.1}$$

where z_B and z_D are the decay positions along the beam axis of the B^0 meson and D meson, respectively, and σ_{z_B} and σ_{z_D} are their uncertainties. In a charmless decay, all particles from the B^0-meson decay originate from the same point in space, so requiring candidates to have a large FDS decreases the charmless yield.

The distribution of charmless decays is uniform in D-meson invariant mass and peaking in B^0-meson invariant mass. The charmless contribution can therefore be quantified by examining candidates in the D-meson invariant-mass sidebands ($>$ 50 MeV/c^2 from the known D-meson mass). As these sidebands can be populated

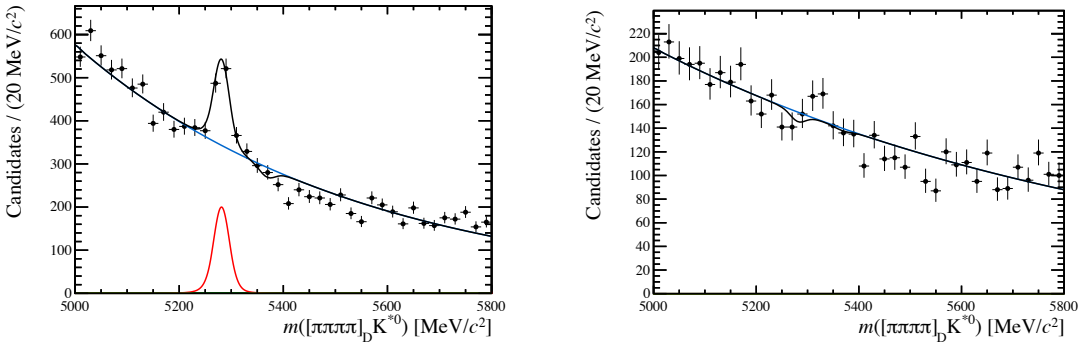

(a) FDS > 0 (b) FDS > 3

Figure 4.10: Fits to the B^0-meson invariant-mass distribution in the D-meson mass sideband in the 4π mode, with the flight-distance significance of the D meson required to be (a) greater than 0 and (b) greater than 3.

by physics backgrounds other than charmless decays, we only consider the upper or lower sideband for certain modes; for example, misidentified $K\pi$ events contaminate the upper sideband of the KK mode and the lower sideband of the $\pi\pi$ mode. The sideband yields in the fully selected samples are very low, so this study is performed using data samples without any BDT requirements and therefore provides upper bounds on the charmless yields in the final samples.

Evidence for contamination from charmless B_s^0 decays is also seen in the πK and $\pi K\pi\pi$ modes prior to the FDS cut, but is reduced to a negligible level with FDS > 3.

A requirement of FDS > 3 is used in the final selection, which retains around 70% of true signal candidates while reducing the charmless yield to a negligible level. As the uncertainties on the yields in Table 4.4 are relatively large, a potential residual contamination is investigated as a source of systematic uncertainty in Sect. 5.3.

Favoured-to-suppressed cross-feed

Favoured $D \to K\pi(\pi\pi)$ decays can contaminate the samples of less abundant decays, particularly the suppressed ADS modes $D \to \pi K(\pi\pi)$, which have branching fractions approximately 17 times smaller than those of the favoured modes. This cross-feed occurs when a kaon and pion from the D-meson decay are both misidentified, and is therefore referred to as the "double-mis-ID" background.

Table 4.4: Estimated charmless yields in data for flight-distance significance cuts of 0 and 3. Negative yields are allowed in the fits to increase stability.

D mode	FDS > 0		FDS > 3	
	Run 1	Run 2	Run 1	Run 2
$K\pi$	6 ± 9	0 ± 5	-7 ± 3	-1 ± 3
πK	14 ± 12	24 ± 10	-2 ± 5	-1 ± 4
KK	101 ± 16	145 ± 15	2 ± 8	1 ± 5
$\pi\pi$	122 ± 15	259 ± 19	3 ± 5	5 ± 5
$K\pi\pi\pi$	6 ± 12	-17 ± 14	12 ± 9	-1 ± 10
$\pi K\pi\pi$	5 ± 17	6 ± 13	6 ± 9	2 ± 12
4π	n/a	348 ± 35	n/a	-14 ± 18

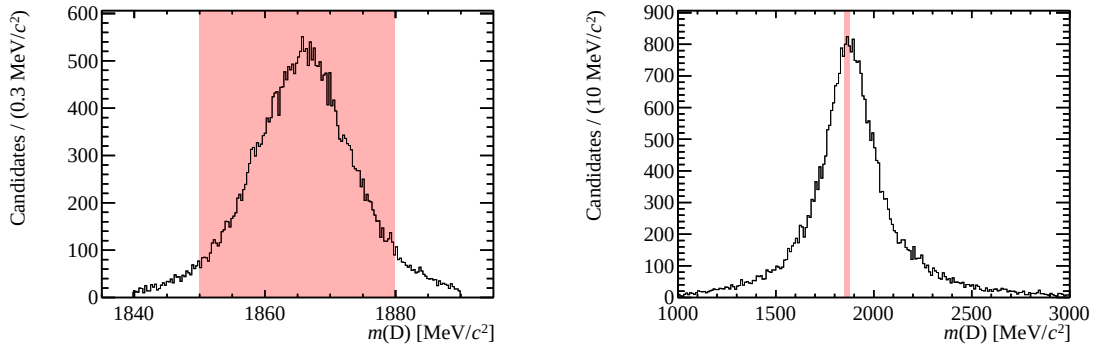

(a) Correct D-meson mass

(b) Swapped hypothesis D-meson mass

Figure 4.11: Invariant-mass distribution of the D meson in simulated $B^0 \to D(K\pi)K^{*0}$ decays, with (a) correctly identified decay products and (b) the kaon and pion mass hypotheses swapped. The red shaded area shows the region removed by a veto on candidates within $\pm 15\,\mathrm{MeV}/c^2$ of the known D-meson mass.

The D-meson invariant-mass requirement discussed in Sect. 4.1.1 and PID selection discussed in Sect. 4.1.3 significantly reduce this background, but an additional veto must be applied in order to reduce it to a negligible level. In the πK mode, the double-mis-ID invariant mass of the D meson is calculated by swapping the kaon and pion mass hypotheses. Candidates for which this variable is within $\pm 15\,\mathrm{MeV}/c^2$ of the known mass of the D meson are removed from the sample. Figure 4.11 shows the vetoed region overlaid on the correctly reconstructed and double-mis-ID D-meson invariant-mass distributions of simulated events. The veto retains 93% of genuine signal and removes 89% of double-mis-ID background.

In four-body ADS decays, $D \to K^{\pm}\pi^{\mp}\pi^{+}\pi^{-}$, there are two pions that could be misidentified as a kaon. The two corresponding double-mis-ID D-meson invariant masses are calculated, and the $\pm 15\,\mathrm{MeV}/c^2$ veto is applied to both. The vetoes are also applied to the favoured modes so that the favoured and suppressed modes have the same selection efficiencies.

The remaining double-mis-ID contamination in the selected samples depends on the efficiencies of the D-meson invariant-mass requirement, PID selection, and double-mis-ID veto. The efficiencies are calculated from simulated samples in the case where the D-meson products are correctly identified and the case where the kaon and pion are swapped. The ratio between the total efficiencies of the two cases gives the expected ratio between the double-mis-ID yield and the favoured-mode signal yield, which is found to be approximately 10^{-4}. The favoured-mode yields are found to be $\mathcal{O}(1000)$ events in the invariant-mass fits to selected candidates, so the double-mis-ID yield in the suppressed ADS samples is $\mathcal{O}(0.1)$ events and is considered to be negligible.

A cross-feed from doubly misidentified K^{*0}-meson products can also contaminate the suppressed modes. The tight PID requirement on the kaon from the K^{*0} meson suppresses this background to $\mathcal{O}(0.5)$ events, which is small enough that no additional veto is required.

Background from $B^+ \to DK^+$ with a random pion

A background can arise from $B^+ \to DK^+$ decays combined with a random pion from elsewhere in the event, which appear as a peak at the mass of the B^+ meson in the DK^+ invariant-mass spectrum. This background is reduced to a negligible level with the requirement $|m(DK^+) - m_{\mathrm{PDG}}(B^+)| > 25\,\mathrm{MeV}/c^2$, where $m_{\mathrm{PDG}}(B^+)$ is the known mass of the B^+ meson.

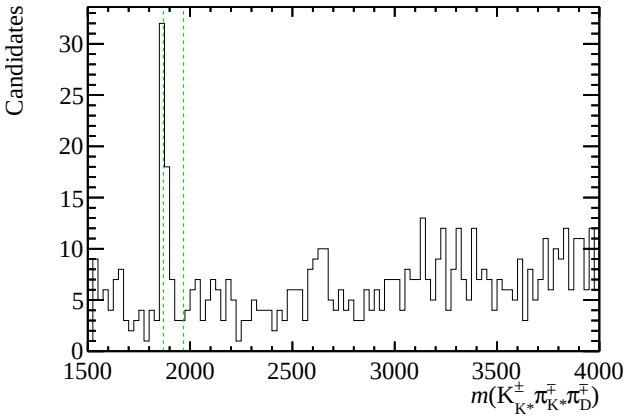

Figure 4.12: Invariant-mass distribution of $K^+\pi^-\pi^-$ mesons in selected data candidates in the $\pi\pi$ mode. The known masses of the D^+ and D_s^+ mesons are marked in green. A peak from $B^0 \to D^-(K^+\pi^-\pi^-)\pi^+$ decays can be seen at the D^+-meson mass.

Background from $B^0_{(s)} \to D^{\pm}_{(s)} h^{\mp}$ decays

Decays of $B^0_{(s)} \to D^- h^+$ ($h = K, \pi$), $D_s^- K^+$ and $D_s^+ \pi^+$, where the $D^{\pm}_{(s)}$ meson decays to a three-body combination of kaons and pions, can have the same final state as the signal decay. The dominant charm-meson decays making up this background are $D^+ \to K^-\pi^+\pi^+$ and $D_s^+ \to K^+K^-\pi^+$. We search for this background by studying three-body combinations of the four final-state tracks in selected candidates. The invariant-mass requirement on the D meson ensures that the masses of three-body combinations including both D-meson products are larger than the masses of the $D^{\pm}_{(s)}$ mesons; therefore, only combinations containing both K^{*0}-meson decay products are of interest.

Figure 4.12 shows a peak from $D^- \to K^+\pi^-\pi^-$ decays in the $\pi\pi$ mode. Evidence of this decay is also seen in the $K\pi$ mode, while evidence of $D_s^- \to K^+K^-\pi^-$ decays is seen in the KK mode. These backgrounds are removed by vetoing candidates whose three-body invariant masses lie within $\pm 15\,\mathrm{MeV}/c^2$ of the relevant charm-meson mass.

In the four-body modes, we search for backgrounds with five-body $D^{\pm}_{(s)}$ decays. These decays have lower branching fractions than the three-body decays, and are found to be completely removed by the invariant-mass constraint on the four D-meson decay products.

Backgrounds involving a Λ_b^0 baryon

A potential background from $\Lambda_b^0 \to Dph$ ($h = K, \pi$) decays, where the proton is misidentified as a kaon or pion, is investigated using simulated events. The selection efficiency of this background is found to be a factor of $(8.4 \pm 1.1) \times 10^{-4}$ smaller than the signal efficiency, so this background is ignored. A background from $\Lambda_b^0 \to \Lambda_c^+(pK\pi)h$ decays was studied in a previous analysis of $B^0 \to DK^{*0}$ decays [44], where it was found to be completely removed by the D-meson FDS cut and PID requirements. The cuts in this analysis are either the same as or tighter than those in Ref. [44], so this background is assumed to be eliminated.

4.1.5 Summary of selection requirements

The selection requirements used in this analysis are summarised in Table 4.5.

Table 4.5: Summary of the requirements used to select $B^0 \to DK^{*0}$ decays with two- and four-body D-meson final states. Known particle masses $m_{\rm PDG}$ are taken from Ref. [71].

Variable	Selection requirement
Mass and helicity angle	
$\lvert m(D) - m_{\rm PDG}(D^0)\rvert$	$< 25\,\text{MeV}/c^2$
$\lvert m(K^{*0}) - m_{\rm PDG}(K^{*0})\rvert$	$< 50\,\text{MeV}/c^2$
$\lvert\cos(\theta^*)\rvert$	> 0.4
BDT classifier	
BDT response for $K\pi/\pi K$	> 0.0
BDT response for KK	> 0.0
BDT response for $\pi\pi$	> 0.4
BDT response for $K\pi\pi\pi/\pi K\pi\pi$	> 0.0
BDT response for 4π	> 0.7
Particle identification	
DLL_K of K^{*0}-meson products	> 5 for kaon, < -1 for pion
DLL_K of D-meson products ($D \to hh'$)	> 1 for kaons, < -1 for pions
DLL_K of D-meson products ($D \to K^-\pi^+\pi^-\pi^+$)	> 1 for K^-, < -1 for both π^+
DLL_K of D-meson products ($D \to \pi^+\pi^-\pi^+\pi^-$)	< -1 for both π^+
Cuts to suppress physics backgrounds	
D-meson flight-distance significance	> 3
$\lvert m(D_{\rm swapped}) - m_{\rm PDG}(D^0)\rvert$	$> 15\,\text{MeV}/c^2$ for ADS modes
$\lvert m(DK^+) - m_{\rm PDG}(B^+)\rvert$	$> 25\,\text{MeV}/c^2$
$\lvert m(K^+\pi^-\pi^-) - m_{\rm PDG}(D^+)\rvert$	$> 15\,\text{MeV}/c^2$ for $K\pi$ and KK
$\lvert m(K^+K^-\pi^-) - m_{\rm PDG}(D_s^+)\rvert$	$> 15\,\text{MeV}/c^2$ for $\pi\pi$

4.2 Invariant-mass parametrisation

A model is developed to describe the invariant-mass distributions of the selected candidates. The model contains the following components:

1. Signal $B^0 \to DK^{*0}$ and $\overline{B}{}^0_s \to DK^{*0}$ decays;
2. Combinatorial background;
3. Partially reconstructed $B^0 \to D^*K^{*0}$ and $\overline{B}{}^0_s \to D^*K^{*0}$ decays;
4. Partially reconstructed $B^+ \to DK^+\pi^-\pi^+$ decays;
5. Misidentified $B^0 \to D\pi^+\pi^-$ decays.

This section describes how each component is modelled and how the yields of some components are constrained in order to simplify the fit to data.

4.2.1 Extended maximum-likelihood fit

A set of experimental measurements x contains n independent observations $\{x_1, x_2, \ldots, x_n\}$; for example, in this analysis we have a measurement of the invariant mass for each of the n selected candidates. A probability density function (PDF) $f(x;\theta)$ models the distribution of x and depends on a set of parameters θ related to the shape of the function. The set of parameters that best models x can be found by maximising the likelihood $L(\theta)$, where

$$L(\theta) = \prod_{i=1}^{n} f(x_i;\theta), \tag{4.2}$$

which is the probability of observing the data set x given the shape parameters θ.

In a counting experiment, the total number of observations varies randomly as well as the observed values themselves. The maximum-likelihood technique can be extended to account for this by including the total number of events described by the PDF, N, as a free parameter. The likelihood in Eq. 4.2 is multiplied by a Poisson

function to give the extended likelihood,

$$L(\theta, N) = \frac{e^{-N}}{n!} N^n \prod_{i=1}^{n} f(x_i; \theta), \tag{4.3}$$

which is the probability of observing a sample x containing n events. The best estimate for θ and N is found by maximising $L(\theta, N)$. In practice, the negative log likelihood, $-2 \log L(\theta, N)$, is minimised using numerical methods. The statistical uncertainty of each parameter is the change in that parameter required to increase $-2 \log L$ by one.

4.2.2 Signal shape

In a perfect measurement, the invariant-mass distribution of true signal decays would be a delta function at the known mass of the B^0 meson. In reality, the finite detector resolution smears the peak, and radiative effects cause tails. As the detector resolution varies with the momenta and positions of the final-state tracks, a single Gaussian function is not sufficient to describe the distribution. Signal decays are modelled using a Cruijff function, which is a centred Gaussian distribution with different left and right resolutions and non-Gaussian tails. It is defined as

$$f_{\text{Cruijff}}(m) = \begin{cases} \exp\left(\dfrac{(m-\mu)^2}{2\sigma_{\text{L}} + \alpha_{\text{L}}(m-\mu)^2}\right), & m < \mu, \\ \exp\left(\dfrac{(m-\mu)^2}{2R\sigma_{\text{L}} + \alpha_{\text{R}}(m-\mu)^2}\right), & m \geq \mu, \end{cases} \tag{4.4}$$

where m is the invariant-mass variable, μ is the mean, σ_{L} is the width of the left-hand side of the shape, R is the ratio between the right and left widths, and $\alpha_{\text{L,R}}$ are tail parameters. The values of the shape parameters are determined from a fit to the invariant-mass distribution of simulated signal decays in the $K\pi$ mode. The projection of the fit is shown in Fig. 4.13. The residuals of the fit are calculated from the differences between the simulated signal yield and the projected fit PDF divided by the Poisson error on the yield. The fitted parameters are given in Table. 4.6. This shape is used in the fit to data, with R and $\alpha_{\text{L,R}}$ fixed, and μ and σ free to vary.

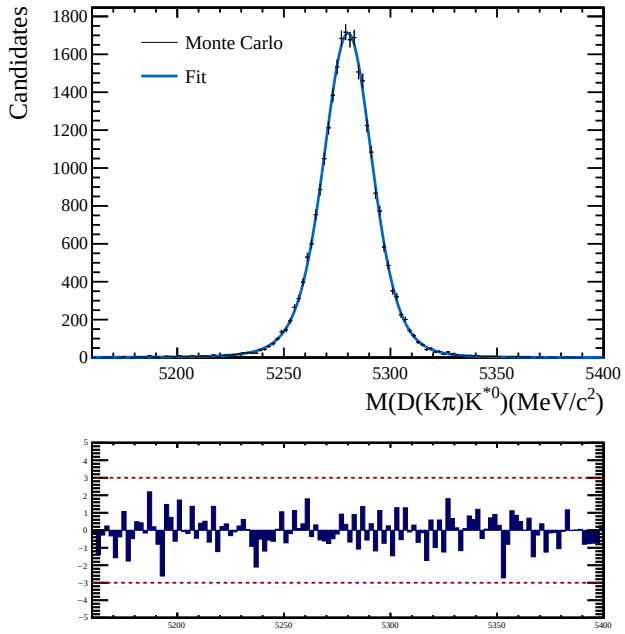

Figure 4.13: Fit to the invariant-mass distribution of selected simulated $B^0 \to D(K\pi)K^{*0}$ decays using a Cruijff function. The residuals are shown below.

Table 4.6: Parameters obtained from fitting a Cruijff function to the invariant-mass distribution of selected simulated $B^0 \to D(K\pi)K^{*0}$ decays.

Parameter	Value
μ (MeV/c^2)	5280.07 ± 0.08
σ_{L} (MeV/c^2)	11.07 ± 0.06
R	0.993 ± 0.009
α_{L}	0.1252 ± 0.0010
α_{R}	0.1131 ± 0.0011

The simulated signal distributions are compared for the different D-meson final states and data-taking periods. No significant variation is seen between Run 1 and Run 2, so shapes obtained from Run 2 simulation are used to describe the full data set throughout this analysis. No difference is observed between the different two-body modes, but the four-body distributions are found to be approximately 5% wider than the two-body distributions. The shape from the $K\pi$ mode is used for all seven modes in the fit to data, with σ_{L} multiplied by a free parameter R_σ in the four-body modes.

A similar model is used for $\overline{B}{}^0_s \to DK^{*0}$ decays, which have larger yields than

$B^0 \to DK^{*0}$ decays in all but the favoured modes. A Cruijff function is obtained from a fit to simulated $\overline{B}{}^0_s \to DK^{*0}$ events. The mean and width of this shape are independent free parameters in the fit to data.

The yields of $B^0 \to DK^*$ and $\overline{B}{}^0_s \to DK^{*0}$ decays in the fit are free to vary in each mode and flavour category. The yields in different categories are related via various asymmetries and ratios, several of which are the *CP* observables of interest.

4.2.3 Combinatorial-background shape

The combinatorial background is modelled using an exponential PDF of the form $f_{\rm comb}(m) = e^{cm}$, where the slope c is negative and is a free parameter. The slope is expected to be the same in the favoured and suppressed ADS modes, so the $K\pi(\pi\pi)$ modes share their slope parameters with the $\pi K(\pi\pi)$ modes. The combinatorial background yield is a free parameter in each mode category and is constrained to be the same in the B^0 and $\overline{B}{}^0$ categories, as this background is not expected to exhibit any *CP* violation.

4.2.4 Partially reconstructed $B^0_{(s)} \to D^*K^{*0}$ background shape

A substantial background from $B^0 \to D^*K^{*0}$ decays with a missed photon or neutral pion appears in the low-mass region. Because this is a scalar $\to$ vector–vector decay, conservation of angular momentum implies that there are only three nonzero helicity amplitudes:

- A_{001}: D^* and K^{*0} mesons both produced with helicity -1;
- A_{010}: D^* and K^{*0} mesons both produced with helicity 0;
- A_{100}: D^* and K^{*0} mesons both produced with helicity $+1$.

The amplitudes A_{001} and A_{100} produce identical invariant-mass distributions, so are combined into a single category labelled 101. The invariant-mass distributions of $D^* \to D\gamma$ and $D^* \to D\pi^0$ decays are different, so four PDFs are needed to describe this

background. Their shapes are found by fitting to samples of simulated $B^0 \to D^* K^{*0}$ decays using three analytic functions named the "Horns", "Hill", and "LittleHorns" functions, which were developed in previous analyses [39, 72].

Horns function

Consider first the decay $B^0 \to D^*(D\pi^0)K^{*0}$ with the D^* meson produced in helicity state 0. The partially reconstructed mass of the B^0 meson is lower than the true B^0-meson mass due to the missing mass and momentum of the neutral pion. The B^0-meson invariant mass has a one-to-one correspondence with the momentum of the π^0 meson, with a larger π^0-meson momentum resulting in a smaller reconstructed B^0-meson mass, and vice versa.

The helicity of the D^* meson and conservation of angular momentum means that in the rest frame of the D^* meson, the spin-0 π^0 meson tends to be emitted in either the same direction or opposite direction to the B^0 meson, where it will carry either the maximum or minimum possible fraction of the momentum of the D^* meson, respectively. The resultant invariant-mass distribution is a parabola $p_{\text{Horns}}(x)$, defined as

$$p_{\text{Horns}}(x) = \begin{cases} \left(x - \dfrac{a+b}{2}\right)^2, & a \geq x \geq b, \\ 0, & \text{otherwise}, \end{cases} \tag{4.5}$$

where a and b are the kinematic endpoints, which are determined by the masses of the particles in the decay.

To account for the finite resolution of the detector, the parabola is convolved with the sum of two Gaussian functions, called a "double Gaussian" function. For Gaussian functions $\mathrm{G}(x|\mu,\sigma)$ with mean μ and width σ, the double Gaussian function $\mathrm{DG}(x)$ is defined as

$$\mathrm{DG}(x) = f_G \mathrm{G}(x|\mu,\sigma) + (1 - f_G)\mathrm{G}(x|\mu, R_\sigma \sigma), \tag{4.6}$$

where σ is the width of the first Gaussian function, R_σ is the relative width of the second Gaussian function, and f_G is the fraction of events contained by the first

Gaussian function. Convolving $\mathrm{DG}(x)$ with $p_{\mathrm{Hill}}(x)$ creates a double-peaked shape, hence the name "Horns".

Candidates with high transverse momenta are more likely to be selected, which distorts the shape such that the right-hand peak is taller than the left. This is accounted for by convolving the PDF with a linear polynomial with slope $1-\xi$, where ξ is the height of the left-hand peak relative to the right. The overall Horns function is given by

$$f_{\mathrm{Horns}}(m) = \int_a^b \mathrm{d}x \left(x - \frac{a+b}{2}\right)^2 \mathrm{DG}(x|m,\sigma,f_G,R_\sigma) \left(\frac{1-\xi}{b-a}x + \frac{b\xi - a}{b-a}\right), \quad (4.7)$$

where m is the invariant-mass variable to be fitted and x is the integration variable in the convolution.

Hill function

Consider instead $B^0 \to D^*(D\pi^0)K^{*0}$ decays with the D^* meson produced in helicity state ± 1. In the rest frame of the D^* meson, the π^0 meson is predominantly produced at $\pm\,90^\circ$ to the direction of the B^0 meson. The fraction of the D^*-meson momentum carried by the π^0 meson is therefore midway between its minimum and maximum values, so instead of a double peak we observe a single, broader peak centred halfway between a and b. This is described by the Hill parabola,

$$p_{\mathrm{Hill}}(x) = \begin{cases} -(x-a)(x-b), & a \geq x \geq b, \\ 0, & \text{otherwise.} \end{cases} \quad (4.8)$$

This parabola is convolved with a double Gaussian function and a linear polynomial to account for detector and selection effects, respectively, giving the overall Hill PDF:

$$f_{\mathrm{Hill}}(m) = \int_a^b \mathrm{d}x \left[-(x-a)(x-b)\mathrm{DG}(x|m,\sigma,f_G,R_\sigma) \left(\frac{1-\xi}{b-a}x + \frac{b\xi - a}{b-a}\right)\right]. \quad (4.9)$$

The Hill function is also used in the case of $B^0 \to D^*(D\gamma)K^{*0}$ decays with the D^* meson produced in helicity state 0. The photon is a spin-1 boson and is therefore predominantly emitted at $\pm\,90^\circ$ to the direction of the B^0 meson in the rest frame of the D^* meson when the D^* meson is longitudinally polarised.

LittleHorns function

The final decay category is $B^0 \to D^*(D\gamma)K^{*0}$ with the D^* meson produced in helicity state ± 1, which requires a third function, LittleHorns. In this case, the underlying kinematic distribution is the sum of a parabola and a uniform distribution:

$$p_{\text{LittleHorns}}(x) = \begin{cases} \left(x - \frac{a+b}{2}\right)^2 + \left(\frac{a-b}{2}\right)^2, & a \geq x \geq b, \\ 0, & \text{otherwise.} \end{cases} \tag{4.10}$$

The overall LittleHorns function is therefore

$$f_{\text{LittleHorns}}(m) = \int_a^b \mathrm{d}x \left[\left(x - \frac{a+b}{2}\right)^2 + \left(\frac{a-b}{2}\right)^2 \right] \mathrm{DG}(x|m, \sigma, f_G, R_\sigma) \tag{4.11}$$

$$\times \left(\frac{1-\xi}{b-a} x + \frac{b\xi - a}{b-a} \right). \tag{4.12}$$

Fits to simulated $B^0 \to DK^{*0}$ decays

Samples of simulated $B^0 \to D^*K^{*0}$ decays are produced with each of the possible D^*-meson decays and helicity configurations. The samples are reconstructed as the signal decay and fitted with the following shapes:

D^* decay	Helicity state	Shape
$D^* \to D\pi^0$	010	Hill
$D^* \to D\pi^0$	101	Horns
$D^* \to D\gamma$	010	LittleHorns
$D^* \to D\gamma$	101	Hill

Fig. 4.14 shows projections of the fits, and Table 4.7 lists the fitted parameters.

An analogous background from $\overline{B}{}^0_s \to D^*K^{*0}$ decays appears in the data at a higher invariant mass. Equivalent PDFs for this background are obtained by fitting the Horns, Hill and LittleHorns functions to simulated $\overline{B}{}^0_s \to D^*K^{*0}$ decays.

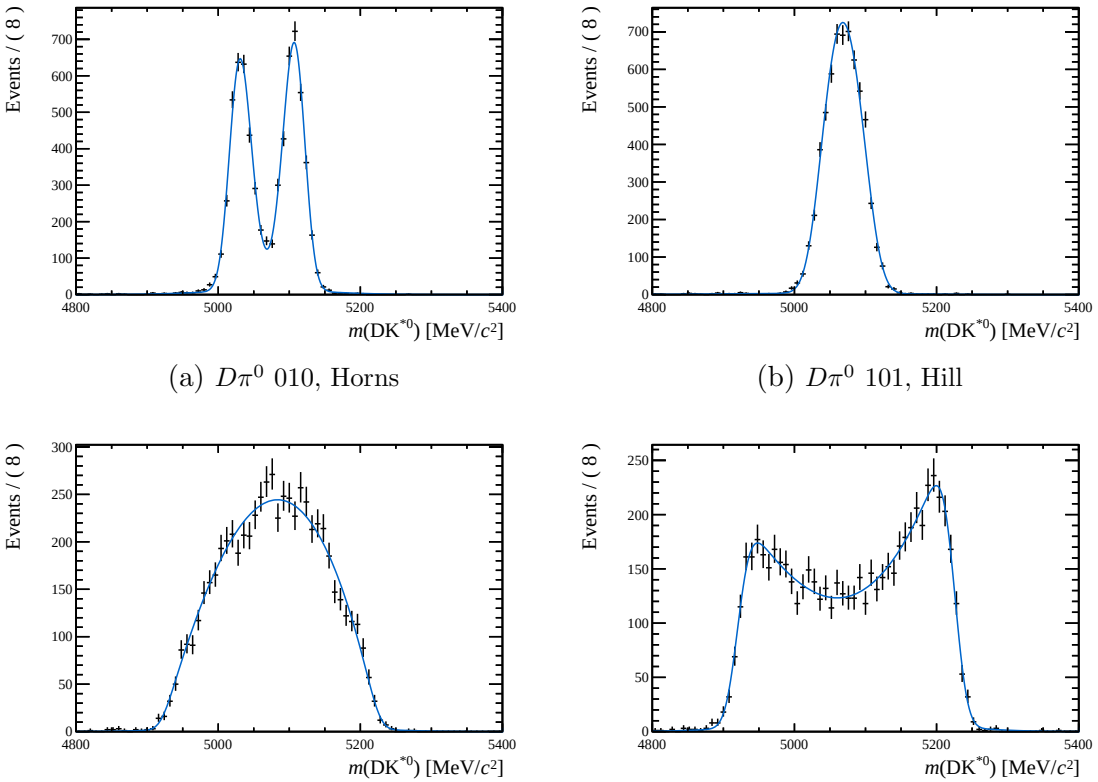

(a) $D\pi^0$ 010, Horns

(b) $D\pi^0$ 101, Hill

(c) $D\gamma$ 010, Hill

(d) $D\gamma$ 101, LittleHorns

Figure 4.14: Fits to the invariant-mass distributions of simulated $B^0 \to D^* K^{*0}$ decays in the four different D^*-meson final-state and helicity configurations: (a) $D^* \to D\pi^0$ with helicity 0, fit with a Horns function; (b) $D^* \to D\pi^0$ with helicity ± 1, fit with a Hill function; (c) $D^* \to D\gamma$ with helicity 0, fit with a Hill function; (d) $D^* \to D\gamma$ with helicity ± 1, fit with a LittleHorns function.

Table 4.7: Parameters obtained from fitting the Horns, Hill and LittleHorns functions to partially reconstructed simulated $B^0 \to D^* K^{*0}$ decays.

	$D^* \to D\pi^0$		$D^* \to D\gamma$	
	010	101	010	101
a (MeV/c^2)	5020.73 ± 0.13	5026.9 ± 0.7	4920.2 ± 0.8	4920.9 ± 0.4
b (MeV/c^2)	5117.06 ± 0.12	5115.4 ± 0.6	5225.8 ± 0.6	5224.9 ± 0.3
σ (MeV/c^2)	12.54 ± 0.08	15.6 ± 0.4	12.2 ± 0.7	13.76 ± 0.28
R_σ	5.71 ± 0.15	7.7 ± 0.4	6.0 ± 0.6	4.70 ± 0.26
f_G	0.9528 ± 0.0025	0.9807 ± 0.0012	0.973 ± 0.006	0.892 ± 0.010
ξ	0.881 ± 0.011	1.33 ± 0.03	0.698 ± 0.027	0.684 ± 0.011

Overall PDF

The overall PDF used to describe $B^0 \to D^* K^{*0}$ decays is the sum of the four PDFs obtained from simulation, with all shape parameters fixed. This can be written as

$$f_{\text{low}} = \alpha_{010} \left[g_{010} f_{\gamma,010} + (1 - g_{010}) f_{\pi^0,010} \right] \tag{4.13}$$

$$+ (1 - \alpha_{010}) \left[g_{101} f_{\gamma,101} + (1 - g_{101}) f_{\pi^0,101} \right], \tag{4.14}$$

where $f_{X,H}$ represents the PDF for $D^* \to DX$ decays with helicity state H, g_H is the relative fraction of $D^* \to D\gamma$ decays in helicity state H, and α_{010} is the relative fraction of events in helicity state 010.

The factors g_{010} and g_{101} are calculated from the relative branching fractions and selection efficiencies of $D^* \to D\gamma$ and $D^* \to D\pi^0$ decays. These values are given in Table 4.8 and are combined to give

$$g_{010} = 0.341 \pm 0.015,$$
$$g_{101} = 0.330 \pm 0.014.$$

The relative contribution of each helicity state is unknown, and is therefore a free parameter in the fit. A single parameter α_{010} is shared between the ADS modes in both B-meson-flavour categories. The different helicity components can exhibit different levels of CP violation, so separate fractions $\alpha_{010}^{\text{GLW}+}$ and $\alpha_{010}^{\text{GLW}-}$ are used in the GLW modes for the decays of B^0 and $\overline{B}^0$ mesons, respectively. The $\overline{B}_s^0 \to D^* K^{*0}$ background can have a different helicity composition to $B^0 \to D^* K^{*0}$ decays but

Table 4.8: Branching fractions, detector acceptance efficiencies, and selection efficiencies of partially reconstructed $B^0 \to D^* K^{*0}$ decays with different D^*-meson final states and helicity configurations. Efficiencies are calculated from simulation.

	$D^* \to D\gamma$		$D^{*0} \to D\pi^0$	
	010	101	010	101
Branching fraction (%)	35.3 ± 0.9 [71]		64.7 ± 0.9 [71]	
Acceptance efficiency (%)	17.56 ± 0.04	17.41 ± 0.05	15.65 ± 0.03	15.49 ± 0.05
Selection efficiency (%)	1.152 ± 0.013	0.565 ± 0.006	1.364 ± 0.014	0.704 ± 0.008

exhibits negligible *CP* violation, so a single helicity fraction β_{010} is used for the $\overline{B}{}^0_s \to D^* K^{*0}$ background in all fit categories.

Yield constraints

There are several overlapping backgrounds in the low-mass region. The invariant-mass fit becomes unstable if the yields of all of these backgrounds are free parameters, particularly in the low-statistics D-meson modes. The stability is improved by sharing parameters between modes where appropriate.

The ratio R_{low} between the yield of the $B^0 \to D^* K^{*0}$ background and the signal yield is shared between the favoured $K\pi(\pi\pi)$ modes for both data-taking periods. The *CP* asymmetry and yield ratio with respect to the favoured modes is shared between the GLW modes.

In the $\pi K(\pi\pi)$ modes, where the yields of B^0_s-meson decays are highest, the ratio $R_{s,\text{low}}$ between the yield of the $\overline{B}{}^0_s \to D^* K^{*0}$ background and the fully reconstructed $\overline{B}{}^0_s \to DK^{*0}$ yield is shared between both modes and data-taking periods. As the interference in this background is negligible, its yield in the GLW modes can be fully fixed from the $\pi K(\pi\pi)$ yields using

$$\mathcal{N}^{hh(hh)}_{s,\text{low}} = \mathcal{N}^{\pi K(\pi\pi)}_{s,\text{low}} \times \frac{\mathcal{B}(D^0 \to h^+h^-(\pi^+\pi^-))}{\mathcal{B}(D^0 \to \pi^+K^-(\pi^+\pi^-))} \times \frac{\epsilon(B^0 \to D(h^+h^-(\pi^+\pi^-))K^{*0})}{\epsilon(B^0 \to D(\pi^+K^-(\pi^+\pi^-))K^{*0})}, \tag{4.15}$$

where $\mathcal{N}^{hh(\pi\pi)}_{s,\text{low}}$ is the yield in the GLW mode $hh(\pi\pi)$, $\mathcal{N}^{\pi K(\pi\pi)}_{s,\text{low}}$ is the yield in the $\pi K(\pi\pi)$ mode, $\mathcal{B}$ is a known branching fraction, and ϵ is the efficiency of the selection and PID requirements. The *CP* asymmetry is fixed to zero.

4.2.5 Partially reconstructed $B^+ \to DK^+\pi^-\pi^+$ background shape

The background from $B^+ \to DK^+\pi^-\pi^+$ decays with a missed pion is made up of various resonant and nonresonant contributions. The selection efficiency for this background is low, so a large fully simulated sample would be very time-consuming to produce. Instead, a simplified simulation is run using the RapidSim [73] package,

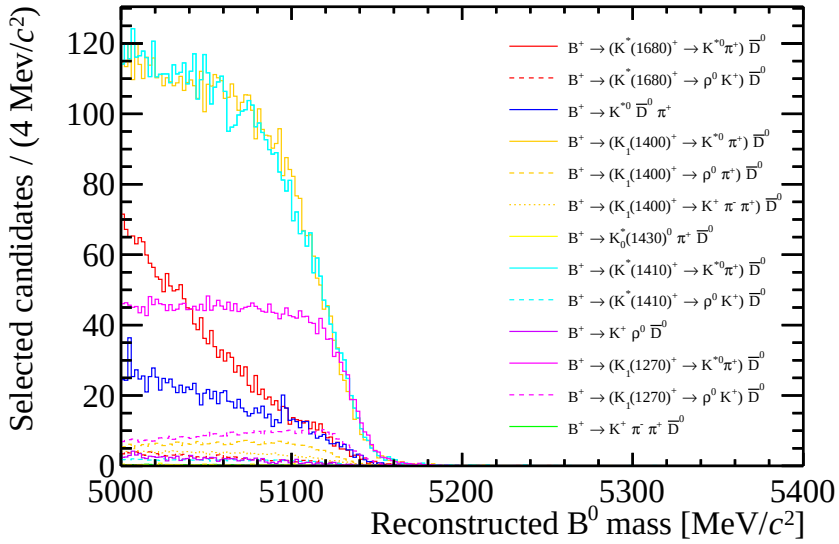

Figure 4.15: Invariant-mass distributions of samples of partially reconstructed $B^+ \to DK^+\pi^-\pi^+$ decays with different intermediate resonances.

which generates the decay kinematics and applies simple resolution effects but does not simulate the full LHCb detector. One million events of each contributing decay are generated and reconstructed as the signal decay. The samples are combined into a cocktail, with each contribution weighted according to its relative branching fraction. Figure 4.15 shows the invariant-mass distributions of the weighted samples.

To model this background, an arbitrary PDF consisting of the sum of two Gaussian functions with different means and a Hill function is fitted to the invariant-mass distribution of the cocktail. Figure 4.16 shows the fit projection. The fitted parameters are listed in Table 4.9 and are fixed in the fit to data.

The $B^+ \to DK^+\pi^-\pi^+$ background is large enough in the favoured D-meson modes that its yield can be a free parameter without causing fit instability. The ratio of this yield with respect to the signal yield, $R_{DK\pi\pi}$, is shared between the $K\pi(\pi\pi)$ modes for both data-taking periods. In all other modes, this background has a low yield and can exhibit a nonzero B^0–$\overline{B}^0$ asymmetry due to CP violation. The CP asymmetries and yield ratios with respect to the favoured mode are fixed to values measured in a dedicated analysis of $B^+ \to DK^+\pi^-\pi^+$ decays [74].

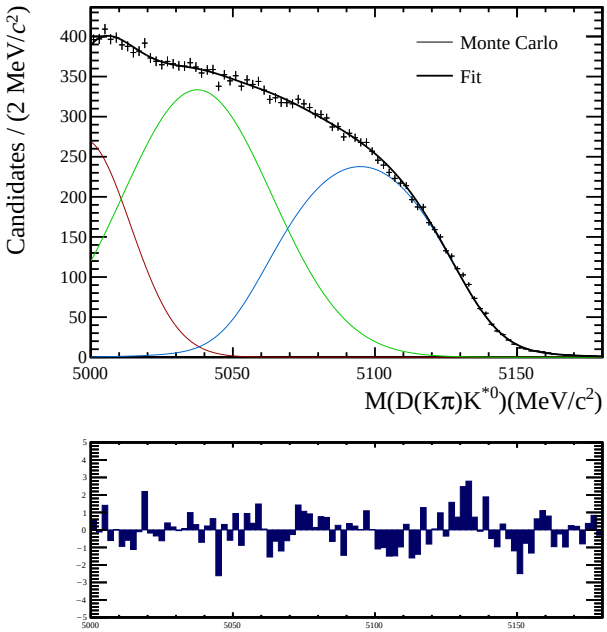

Figure 4.16: Fit to partially reconstructed simulated $B^0 \to DK^+\pi^-\pi^+$ decays. The fit PDF is the sum of a Hill function (blue) and two Gaussian functions (red and green). The residuals are shown below.

Table 4.9: Parameters obtained from a fit to partially reconstructed simulated $B^+ \to DK^+\pi^-\pi^+$ decays using the sum of a Hill function and two Gaussian functions.

Shape	Parameter	Value
Hill	a (MeV/c^2)	5050 (fixed)
	b (MeV/c^2)	5139.69 (fixed)
	σ (MeV/c^2)	10.6 ± 2.0
	R_σ	2.5 ± 0.6
	f_G	0.85 ± 0.16
	ξ	1 (fixed)
Gaussian 1	μ (MeV/c^2)	4998 ± 6
	σ (MeV/c^2)	16 ± 8
	f	0.12 ± 0.10
Gaussian 2	μ (MeV/c^2)	5038 ± 8
	σ (MeV/c^2)	26 ± 5
	f	0.50 ± 0.11

4.2.6 Misidentified $B^0 \to D\pi^+\pi^-$ background shape

The background from misidentified $B^0 \to D\pi^+\pi^-$ decays appears as a peak above the mass of the B^0 meson. The dominant contribution to these decays is $B^0 \to D\rho^0$. A PDF is obtained by fitting to a sample of simulated $B^0 \to D\rho^0$ decays using the sum of two Crystal Ball functions. A single Crystal Ball function is defined as

$$\mathrm{CB}(m) = \begin{cases} e^{-((m-\mu)/\sigma)^2/2}, & \frac{m-\mu}{\sigma} \geq -\alpha, \\ \left(\frac{n}{|\alpha|}\right)^n e^{|\alpha|^2/2} \left(\frac{n}{|\alpha|} - |\alpha| - \left(\frac{m-\mu}{\sigma}\right)\right)^{-n}, & \text{otherwise,} \end{cases} \tag{4.16}$$

where μ is the mean, σ is the width, and α and n are tail parameters. In the double Crystal Ball fit, the two functions share a single mean but have separate widths and tail parameters, so the double Crystal Ball function can be written as

$$\mathrm{DCB}(m) = f_\mathrm{L}\mathrm{CB}(m|\mu, \sigma_\mathrm{L}, \alpha_\mathrm{L}, n_\mathrm{L}) + (1 - f_\mathrm{L})\mathrm{CB}(m|\mu, R_\sigma\sigma_\mathrm{L}, \alpha_\mathrm{R}, n_\mathrm{R}), \tag{4.17}$$

where f_L is the fraction of events contained within the left-hand Crystal Ball function, and R_σ is the ratio between the right- and left-hand widths.

The invariant-mass distribution of misidentified decays depends on the PID requirement applied to the misidentified particle. The PID efficiency of each simulated $B^0 \to D\rho^0$ event is calculated according to the measured performance of the PID requirement in calibration data (discussed further in Sect. 5.1.2), and the invariant-mass distribution is weighted by these efficiencies. The projection of a fit to the weighted distribution is shown in Fig. 4.17, and the fitted parameters are given in Table 4.10. These parameters are fixed in the fit to data.

Yield constraints

The ratio of the $B^0 \to D\pi^+\pi^-$ yield with respect to the signal yield is a free parameter $R_{D\pi\pi}$, which is shared between the $K\pi$ and $K\pi\pi\pi$ modes. The absence of a true K^+ meson means that the candidates cannot be accurately tagged as originating from a B^0 or $\overline{B}^0$ meson, and are instead distributed randomly between the flavour categories. The CP asymmetry in this background is therefore fixed to zero. The charge of the

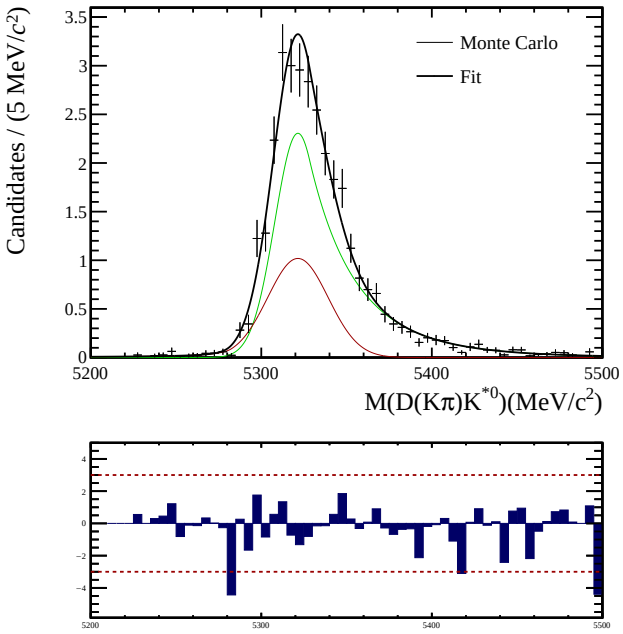

Figure 4.17: Fit to misidentified simulated $B^0 \to D\rho^0$ decays using the sum of two Crystal Ball functions. The residuals are shown below.

K^+ meson is also used to separate the favoured and suppressed ADS modes, so the background is assumed to be equally split between these modes, *i.e.* the $\pi K(\pi\pi)$ yields are fixed to the $K\pi(\pi\pi)$ yields. The yields in the GLW modes are fixed with respect to the ADS yields in a similar manner to the yields of the $\overline{B}{}^0_s \to D^* K^{*0}$ background, given in Eq. 4.15.

The relative background yield is expected to be slightly different in the two data-taking periods due to improvements in particle identification in Run 2, so the parameter $R_{D\pi\pi}$ cannot be shared between the two periods. The yield of this background in the Run 1 data is too small for $R_{D\pi\pi}(\text{Run 1})$ to be determined independently, but it can be fixed with respect to the $R_{D\pi\pi}(\text{Run 2})$ using

$$R_{D\pi\pi}(\text{Run 2}) = R_{D\pi\pi}(\text{Run 1}) \times \frac{\epsilon_{\text{PID}}(D\rho^0, \text{Run 2})}{\epsilon_{\text{PID}}(D\rho^0, \text{Run 1})} \times \frac{\epsilon_{\text{PID}}(DK^{*0}, \text{Run 1})}{\epsilon_{\text{PID}}(DK^{*0}, \text{Run 2})}, \quad (4.18)$$

where $\epsilon_{\text{PID}}(DX, \text{Run } N)$ is the PID efficiency of simulated $B^0 \to DX$ decays in Run N. The measured efficiencies are given in Table 4.11. The ratio between $R_{D\pi\pi}(\text{Run 2})$ and $R_{D\pi\pi}(\text{Run 1})$ is found to be 0.928 ± 0.014, which indicates that the background-

Table 4.10: Parameters obtained from a fit to misidentified simulated $B^0 \to D\rho^0$ decays with the sum of two Crystal Ball functions.

Parameter	Value
μ (MeV/c^2)	5321.5 ± 2.9
σ_L (MeV/c^2)	18 ± 4
R_σ	0.76 ± 0.24
f_L	0.3 ± 0.3
α_L	2.2 ± 0.6
α_R	-0.5 ± 0.3
n_L	1 (fixed)
n_R	9 ± 5

Table 4.11: PID efficiencies in % of simulated misidentified $B^0 \to D\rho^0$ decays and signal $B^0 \to DK^{*0}$ decays, and the ratio between them, given for each data-taking period.

	$\epsilon_{\rm PID}(D\rho^0)$	$\epsilon_{\rm PID}(DK^{*0})$	Ratio
Run 1	2.2 ± 0.5	66.6 ± 0.4	$(3.3 \pm 0.8) \times 10^{-2}$
Run 2	2.4 ± 0.9	77.49 ± 0.18	$(3.0 \pm 1.2) \times 10^{-2}$

to-signal ratio is lower in Run 2, as expected.

4.2.7 Shared fit parameters

To account for small inaccuracies in the simulation, the means of all background shapes in the fit to data are added to a floating global shift, Δ. This is not necessary for the signal shapes, which have floating means.

In studies of simulated signal decays, the four-body invariant-mass distributions were found to be wider than the two-body distributions. In the fit to data, the four- and two-body signal widths are related via a free parameter, R_σ; however, it is found that the fit is only stable if the widths of the background PDFs are completely fixed. The widths of the four-body background shapes are therefore calculated by multiplying the two-body widths by a fixed ratio of 1.054 ± 0.007, which is calculated from fits to simulated events in the $K\pi$ and $K\pi\pi\pi$ modes.

4.3 Results of the invariant-mass fit

The selected data candidates are split into the seven D-meson final states, two B-meson flavours, and two data-taking periods. As data from Run 1 are not used in the 4π mode, there are a total of 26 categories. The invariant-mass distributions of the candidates in each category are fitted simultaneously in the range $5000 < m(B^0) < 5800\,\text{MeV}/c^2$. Several shape and yield parameters are set to be common, allowing parameters that are constrained by the high-yielding modes to be shared with the less abundant ones.

Figures 4.18–4.21 show the invariant mass distributions and fitted PDFs for each D-meson decay and B-meson flavour, summed over data-taking period. Table 4.12 gives the signal yields of each decay. The central values and statistical uncertainties of the free parameters in the fit, including the CP observables, are given in Table 4.3.

In the GLW fits, shown in Fig. 4.18, distinct signal peaks from $B^0 \to DK^{*0}$ and $\overline{B}{}^0_s \to DK^{*0}$ decays appear at the masses of the B^0 and B^0_s mesons, respectively. The low-mass region is populated by the partially reconstructed $B^0 \to D^*K^{*0}$ and $\overline{B}{}^0_s \to D^*K^{*0}$ backgrounds, which contribute in roughly the same proportion as their fully reconstructed counterparts. A small contribution from $B^+ \to DK^+\pi^-\pi^+$ decays lies in the low-mass region, and a very small peak from misidentified $B^0 \to D\pi^+\pi^-$ decays appears between the B^0-meson and B^0_s-meson peaks.

The two-body ADS fits are shown in Fig. 4.19. In the favoured mode, signal $B^0 \to DK^{*0}$ decays and partially reconstructed $B^0 \to D^*K^{*0}$ decays have large yields, while the corresponding decays of B^0_s mesons have negligible yields. The invariant-mass distributions of the suppressed ADS modes are shown on a logarithmic scale to emphasise the small signal peak. The $\overline{B}{}^0_s \to DK^{*0}$ and $\overline{B}{}^0_s \to D^*K^{*0}$ decays have large yields in the suppressed mode.

The distributions of the four-body modes, shown in Figs. 4.20 and 4.21, are very similar to the two-body distributions. Although the four-body D-meson decays have larger branching fractions than the two-body decays, the measured four-body yields

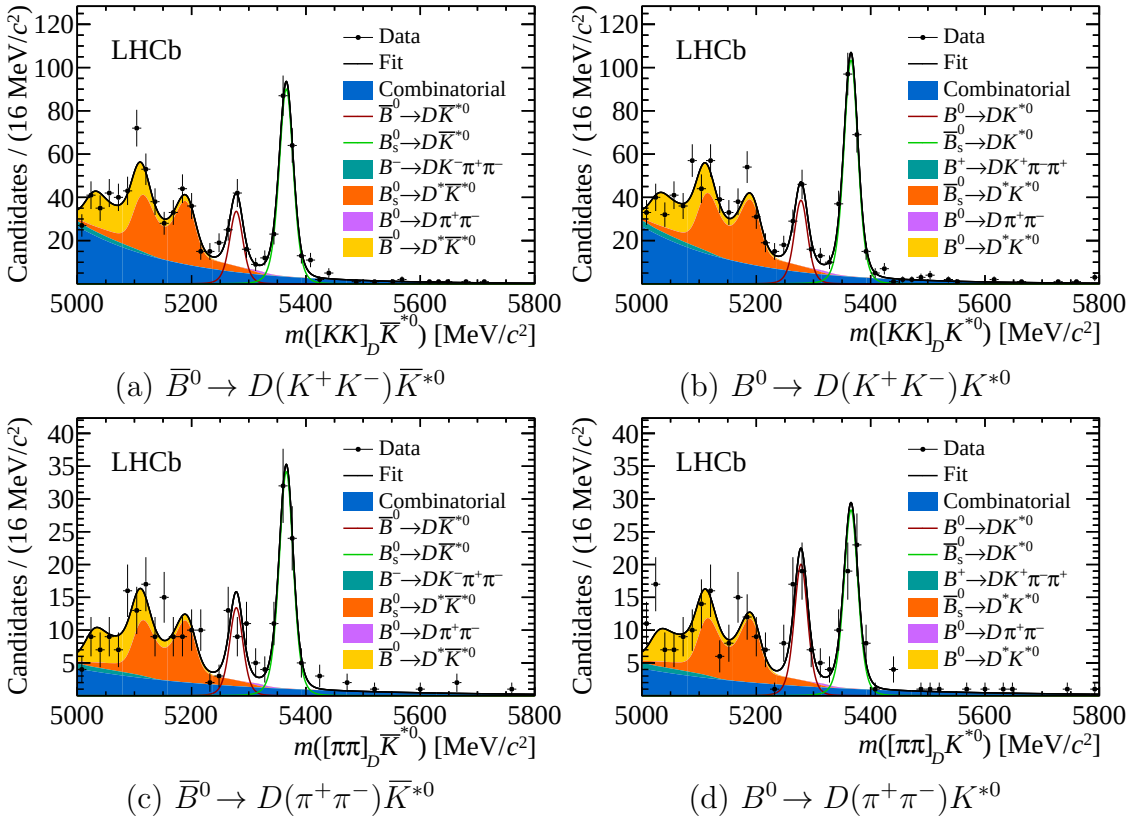

(a) $\overline{B}^0 \to D(K^+K^-)\overline{K}^{*0}$ (b) $B^0 \to D(K^+K^-)K^{*0}$

(c) $\overline{B}^0 \to D(\pi^+\pi^-)\overline{K}^{*0}$ (d) $B^0 \to D(\pi^+\pi^-)K^{*0}$

Figure 4.18: Invariant-mass distributions (data points with error bars) and results of the fit (lines and coloured areas) for the two-body GLW decays (a) $\overline{B}^0 \to D(K^+K^-)\overline{K}^{*0}$, (b) $B^0 \to D(K^+K^-)K^{*0}$, (c) $\overline{B}^0 \to D(\pi^+\pi^-)\overline{K}^{*0}$, and (d) $B^0 \to D(\pi^+\pi^-)K^{*0}$.

are smaller because the efficiency of reconstructing a decay decreases as the number of final-state tracks increases. The significant signal peaks in the 4π mode are notable, as this is the first time $B^0 \to D(\pi^+\pi^-\pi^+\pi^-)K^{*0}$ decays have been studied.

Table 4.12: Summary of signal yields. The uncertainties are statistical.

Decay channel	$\overline{B}^0$ yield	B^0 yield
$B^0 \to D(K^+K^-)K^{*0}$	67 ± 10	77 ± 11
$B^0 \to D(\pi^+\pi^-)K^{*0}$	27 ± 6	40 ± 7
$B^0 \to D(\pi^+\pi^-\pi^+\pi^-)K^{*0}$	32 ± 7	35 ± 8
$B^0 \to D(K^+\pi^-)K^{*0}$	786 ± 29	754 ± 29
$B^0 \to D(\pi^+K^-)K^{*0}$	76 ± 16	47 ± 15
$B^0 \to D(K^+\pi^-\pi^+\pi^-)K^{*0}$	557 ± 25	548 ± 25
$B^0 \to D(\pi^+K^-\pi^+\pi^-)K^{*0}$	41 ± 14	40 ± 14

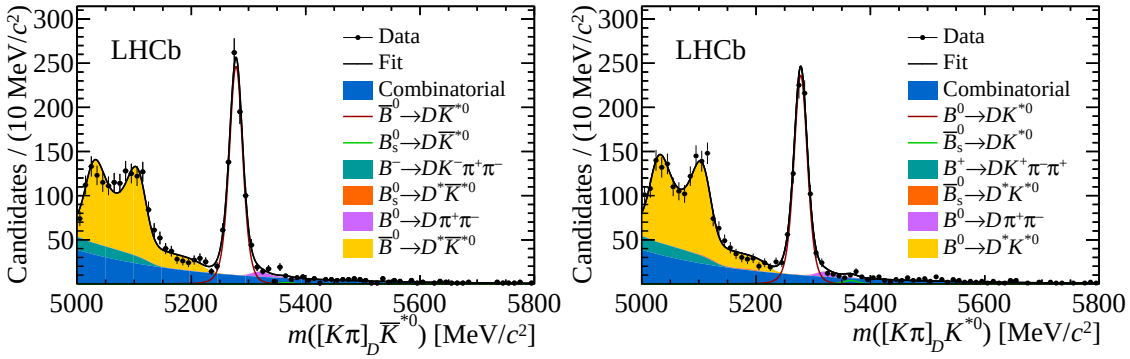

(a) $\overline{B}^0 \to D(K^-\pi^+)\overline{K}^{*0}$ (b) $B^0 \to D(K^+\pi^-)K^{*0}$

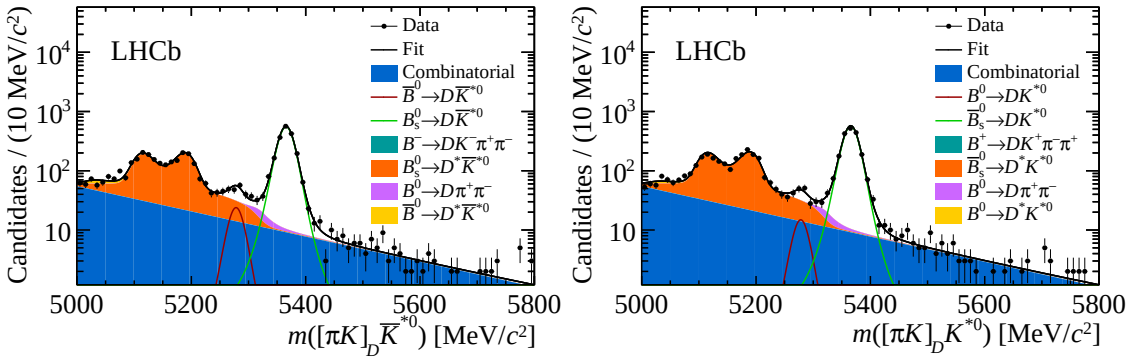

(a) $\overline{B}^0 \to D(\pi^-K^+)\overline{K}^{*0}$ (b) $B^0 \to D(\pi^+K^-)K^{*0}$

Figure 4.19: Invariant-mass distributions (data points with error bars) and results of the fit (lines and coloured areas) for the two-body favoured ADS decays (a) $\overline{B}^0 \to D(K^-\pi^+)\overline{K}^{*0}$ and (b) $B^0 \to D(K^+\pi^-)K^{*0}$, and the two-body suppressed ADS decays (c) $\overline{B}^0 \to D(\pi^-K^+)\overline{K}^{*0}$ and (d) $B^0 \to D(\pi^+K^-)K^{*0}$. The bottom distributions are shown on a logarithmic scale.

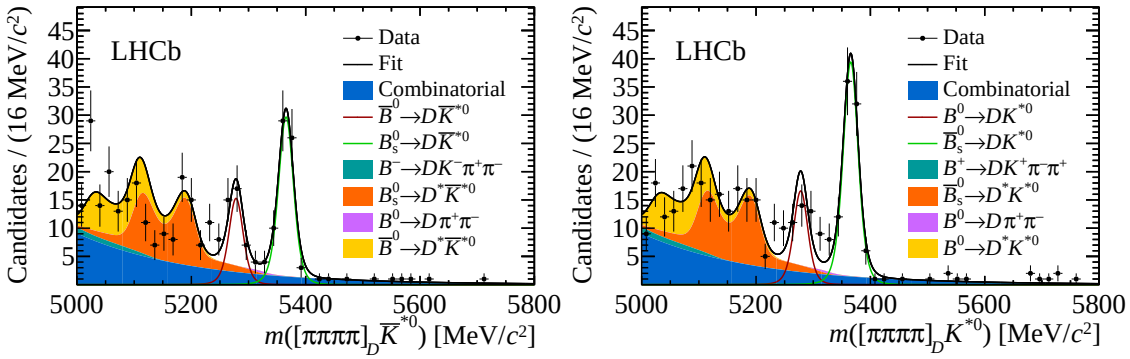

(a) $\overline{B}^0 \to D(\pi^+\pi^-\pi^+\pi^-)\overline{K}^{*0}$ (b) $B^0 \to D(\pi^+\pi^-\pi^+\pi^-)K^{*0}$

Figure 4.20: Invariant-mass distributions (data points with error bars) and results of the fit (lines and coloured areas) for the four-body GLW decays (a) $\overline{B}^0 \to D(\pi^+\pi^-\pi^+\pi^-)\overline{K}^{*0}$, (b) $B^0 \to D(\pi^+\pi^-\pi^+\pi^-)K^{*0}$.

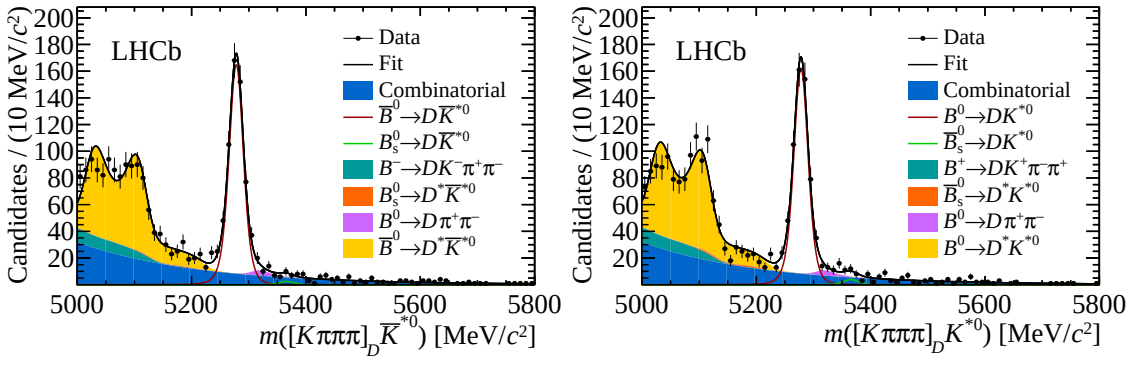

(a) $\overline{B}^0 \to D(K^-\pi^+\pi^+\pi^-)\overline{K}^{*0}$

(b) $B^0 \to D(K^+\pi^-\pi^+\pi^-)K^{*0}$

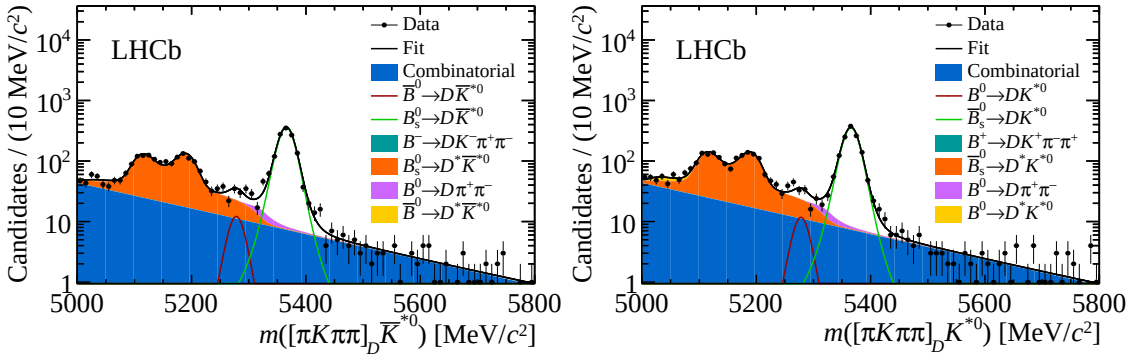

(a) $\overline{B}^0 \to D(\pi^-K^+\pi\pi^-)\overline{K}^{*0}$

(b) $B^0 \to D(\pi^+K^-\pi\pi^-)K^{*0}$

Figure 4.21: Invariant-mass distributions (data points with error bars) and results of the fit (lines and coloured areas) for the four-body favoured ADS decays (a) $\overline{B}^0 \to D(K^-\pi^+\pi^-\pi^+)\overline{K}^{*0}$ and (b) $B^0 \to D(K^+\pi^-\pi^+\pi^-)K^{*0}$, and the four-body suppressed ADS decays (c) $\overline{B}^0 \to D(\pi^-K^+\pi^+\pi^-)\overline{K}^{*0}$ and (d) $B^0 \to D(\pi^+K^-\pi^-\pi^+)K^{*0}$. The bottom distributions are shown on a logarithmic scale.

Table 4.13: Values obtained for the free parameters in a fit to the invariant-mass distributions of selected data candidates.

Parameter	Description	Value
CP observables		
$\mathcal{A}_{CP}^{KK}$	*CP* asymmetry in KK mode	-0.05 ± 0.10
$\mathcal{A}_{CP}^{\pi\pi}$	*CP* asymmetry in $\pi\pi$ mode	-0.18 ± 0.14
$\mathcal{R}_{CP}^{KK}$	Normalised ratio between KK and $K\pi$ yields	0.92 ± 0.10
$\mathcal{R}_{CP}^{\pi\pi}$	Normalised ratio between $\pi\pi$ and $K\pi$ yields	1.32 ± 0.19
$\mathcal{A}_{CP}^{4\pi}$	*CP* asymmetry in 4π mode	-0.03 ± 0.15
$\mathcal{R}_{CP}^{4\pi}$	Normalised ratio between 4π and $K\pi\pi\pi$ yields	1.01 ± 0.16
$\mathcal{R}_{+}^{\pi K}$	Ratio between πK and $K\pi$ yields in B^0 decays	0.095 ± 0.021
$\mathcal{R}_{-}^{\pi K}$	Ratio between πK and $K\pi$ yields in $\overline{B}^0$ decays	0.064 ± 0.021
$\mathcal{R}_{+}^{\pi K\pi\pi}$	Ratio between $\pi K\pi\pi$ and $K\pi\pi\pi$ yields in B^0 decays	0.072 ± 0.025
$\mathcal{R}_{-}^{\pi K\pi\pi}$	Ratio between $\pi K\pi\pi$ and $K\pi\pi\pi$ yields in $\overline{B}^0$ decays	0.074 ± 0.026
$\mathcal{A}_{\text{ADS}}^{K\pi}$	*CP* asymmetry in $K\pi$ mode	0.047 ± 0.027
$\mathcal{A}_{\text{ADS}}^{K\pi\pi\pi}$	*CP* asymmetry in $K\pi\pi\pi$ mode	0.04 ± 0.03
Signal $B^0 \to DK^{*0}$ decays		
μ	Mean of Cruijff in MeV/c^2	5278.16 ± 0.30
σ	Width of left side of Cruijff in MeV/c^2	11.31 ± 0.28
R_σ	Ratio between four- and two-body signal widths	1.060 ± 0.024
$\mathcal{N}^{K\pi,1}$	Yield of $K\pi$ in Run 1	643 ± 25
$\mathcal{N}^{K\pi,2}$	Yield of $K\pi$ in Run 2	937 ± 28
$\mathcal{N}^{K\pi\pi\pi,1}$	Yield of $K\pi\pi\pi$ in Run 1	424 ± 20
$\mathcal{N}^{K\pi\pi\pi,2}$	Yield of $K\pi\pi\pi$ in Run 2	713 ± 26
$\overline{B}_s^0 \to DK^{*0}$ decays		
μ_s	Mean of Cruijff in MeV/c^2	5365.69 ± 0.19
σ_s	Width of left side of Cruijff in MeV/c^2	12.01 ± 0.19
$\mathcal{N}_s^{\pi K,1}$	Yield of πK in Run 1	1530 ± 30
$\mathcal{N}_s^{\pi K,2}$	Yield of πK in Run 2	2200 ± 40
$\mathcal{N}_s^{\pi K\pi\pi,1}$	Yield of $\pi K\pi\pi$ in Run 1	862 ± 26
$\mathcal{N}_s^{\pi K\pi\pi,2}$	Yield of $\pi K\pi\pi$ in Run 2	1650 ± 40
$\mathcal{N}_s^{KK,1}$	Yield of KK in Run 1	186 ± 15
$\mathcal{N}_s^{KK,2}$	Yield of KK in Run 2	215 ± 15

Continued on next page

Table 4.13 — *Continued from previous page*

Parameter	Description	Value
$\mathcal{N}_s^{\pi\pi,1}$	Yield of $\pi\pi$ in Run 1	39 ± 7
$\mathcal{N}_s^{\pi\pi,2}$	Yield of $\pi\pi$ in Run 2	90 ± 10
$\mathcal{N}_s^{4\pi,2}$	Yield of 4π in Run 2	151 ± 13
$\mathcal{A}_s^{\pi K}$	*CP* asymmetry in πK mode	0.006 ± 0.017
$\mathcal{A}_s^{\pi K\pi\pi}$	*CP* asymmetry in $\pi K\pi\pi$ mode	-0.007 ± 0.021
$\mathcal{A}_s^{KK}$	*CP* asymmetry in KK mode	0.06 ± 0.05
$\mathcal{A}_s^{\pi\pi}$	*CP* asymmetry in $\pi\pi$ mode	-0.11 ± 0.09
$\mathcal{A}_s^{4\pi}$	*CP* asymmetry in 4π mode	0.12 ± 0.08
$\mathcal{R}_{s,-}^{K\pi}$	Ratio between $K\pi$ and πK yields in $\overline{B}_s^0$ decays	0.007 ± 0.004
$\mathcal{R}_{s,+}^{K\pi}$	Ratio between $K\pi$ and πK yields in B_s^0 decays	0.003 ± 0.004
$\mathcal{R}_{s,-}^{K\pi\pi\pi}$	Ratio between $K\pi\pi\pi$ and $\pi K\pi\pi$ yields in $\overline{B}_s^0$ decays	0.011 ± 0.006
$\mathcal{R}_{s,+}^{K\pi\pi\pi}$	Ratio between $K\pi\pi\pi$ and $\pi K\pi\pi$ yields in B_s^0 decays	0.007 ± 0.005
Combinatorial background		
$c^{K\pi}$	Slope of exponential in $K\pi$ and πK modes	-0.0049 ± 0.0002
c^{KK}	Slope of exponential in KK mode	-0.0057 ± 0.0004
$c^{\pi\pi}$	Slope of exponential in $\pi\pi$ mode	-0.0038 ± 0.0006
$c^{K\pi\pi\pi}$	Slope of exponential in $K\pi\pi\pi$ and $\pi K\pi\pi$ modes	-0.0049 ± 0.0002
$c^{4\pi}$	Slope of exponential in 4π mode	-0.0051 ± 0.0006
$N_{\text{comb}}^{K\pi,1}$	Yield in $K\pi$ mode in Run 1	1050 ± 70
$N_{\text{comb}}^{K\pi,2}$	Yield in $K\pi$ mode in Run 2	500 ± 60
$N_{\text{comb}}^{\pi K,1}$	Yield in πK mode in Run 1	1120 ± 80
$N_{\text{comb}}^{\pi K,2}$	Yield in πK mode in Run 2	1070 ± 90
$N_{\text{comb}}^{KK,2}$	Yield in KK mode in Run 1	250 ± 30
$N_{\text{comb}}^{KK,1}$	Yield in KK mode in Run 2	330 ± 30
$N_{\text{comb}}^{\pi\pi,1}$	Yield in $\pi\pi$ mode in Run 1	81 ± 14
$N_{\text{comb}}^{\pi\pi,2}$	Yield in $\pi\pi$ mode in Run 2	50 ± 16
$N_{\text{comb}}^{K\pi\pi\pi,1}$	Yield in $K\pi\pi\pi$ mode in Run 1	600 ± 50
$N_{\text{comb}}^{K\pi\pi\pi,2}$	Yield in $K\pi\pi\pi$ mode in Run 2	680 ± 60
$N_{\text{comb}}^{\pi K\pi\pi,1}$	Yield in $\pi K\pi\pi$ mode in Run 1	690 ± 60
$N_{\text{comb}}^{\pi K\pi\pi,2}$	Yield in $\pi K\pi\pi$ mode in Run 2	1050 ± 90
$N_{\text{comb}}^{4\pi,2}$	Yield in 4π mode in Run 2	220 ± 40

Continued on next page

Table 4.13 — *Continued from previous page*

Parameter	Description	Value
Partially reconstructed $B^0 \to D^* K^{*0}$ background		
α_{010}	Fraction of 010 helicity state in ADS modes	0.709 ± 0.029
$\alpha_{010}^{\text{GLW}+}$	Fraction of 010 helicity state in B^0 decays in GLW modes	0.62 ± 0.17
$\alpha_{010}^{\text{GLW}-}$	Fraction of 010 helicity state in $\overline{B}^0$ decays in GLW modes	0.57 ± 0.17
R_{low}	Ratio of $B^0 \to D^* K^{*0}$ to $B^0 \to D K^{*0}$ in favoured modes	1.50 ± 0.08
$\mathcal{A}_{\text{low}}^{\text{GLW}}$	*CP* asymmetry in GLW modes	0.03 ± 0.09
$\mathcal{R}_{\text{low}}^{\text{GLW}}$	Normalised ratio between GLW and $K\pi$ yields	1.06 ± 0.16
$\mathcal{R}_{\text{low},+}^{\pi K}$	Ratio between πK and $K\pi$ yields in B^0 decays	0.09 ± 0.06
$\mathcal{R}_{\text{low},-}^{\pi K}$	Ratio between πK and $K\pi$ yields in $\overline{B}^0$ decays	0.06 ± 0.06
$\mathcal{R}_{\text{low},+}^{\pi K\pi\pi}$	Ratio between $\pi K\pi\pi$ and $K\pi\pi\pi$ yields in B^0 decays	0.04 ± 0.06
$\mathcal{R}_{\text{low},-}^{\pi K\pi\pi}$	Ratio between $\pi K\pi\pi$ and $K\pi\pi\pi$ yields in $\overline{B}^0$ decays	0.11 ± 0.07
$\mathcal{A}_{\text{low}}^{K\pi}$	*CP* asymmetry in $K\pi$ mode	0.00 ± 0.03
$\mathcal{A}_{\text{low}}^{K\pi\pi\pi}$	*CP* asymmetry in $K\pi\pi\pi$ mode	0.01 ± 0.03
Partially reconstructed $\overline{B}_s^0 \to D^* K^{*0}$ background		
β_{010}	Fraction of 010 helicity state	0.775 ± 0.021
$R_{s,\text{low}}$	Ratio of $\overline{B}_s^0 \to D^* K^{*0}$ to $\overline{B}_s^0 \to D K^{*0}$ in suppressed modes	1.089 ± 0.023
$\mathcal{A}_{s,\text{low}}^{\pi K}$	*CP* asymmetry in πK mode	0.012 ± 0.021
$\mathcal{A}_{s,\text{low}}^{\pi K\pi\pi}$	*CP* asymmetry in $\pi K\pi\pi$ mode	0.026 ± 0.026
Other		
$R_{DK\pi\pi}$	Ratio of $B^+ \to D K^+\pi^-\pi^+$ to $B^0 \to D K^{*0}$ in favoured modes	0.19 ± 0.06
$R_{D\pi\pi}$	Ratio of $B^0 \to D\pi^+\pi^-$ to $B^0 \to D K^{*0}$ in favoured modes in Run 1	0.038 ± 0.009
Δ	Global shift in MeV/c^2	-1.2 ± 0.5

Chapter 5

Measurement of *CP* observables in $B^0 \to DK^{*0}$ decays with two- and four-body D-meson final states

This chapter presents the measurement of *CP* observables related to the CKM angle γ in $B^0 \to DK^{*0}$ decays with two- and four-body D-meson final states. The observables are measured in the extended maxmimum-likelihood fit to selected data candidates presented in Sect. 4.3. The two-body data samples contain approximately 1543, 123, 144 and 67 signal candidates in the $K\pi$, πK, KK and $\pi\pi$ modes, respectively. The four-body samples contain approximately 1105, 81 and 61 signal candidates in the $K\pi\pi\pi$, $\pi K\pi\pi$ and 4π modes, respectively.

The fit is set up such that the *CP* observables are free parameters and are determined directly, rather than being derived from the raw yields in a later step. This removes the need for a complex combination involving many different correlated variables, but means that any corrections to the raw yields must be included in the fit. These corrections are described in Sect. 5.1. Section 5.2 discusses studies to validate the fit, and Sect. 5.3 discusses the evaluation of systematic uncertainties. The results with their statistical and systematic uncertainties are summarised in Sect. 5.4, and the statistical significances of the signals in previously unobserved modes are discussed in Sect. 5.5.

5.1 Determination of the *CP* observables

In the invariant-mass fit presented in Sect. 4.3, the *CP* observables are free parameters related to the raw yields. The raw yields are affected by various experimental biases in addition to the *CP*-violation effects of interest, which we must correct for when constructing relationships between the yields and the *CP* observables.

Several correction factors are calculated using simulated samples. The simulated data should therefore approximate the real data as closely as possible in order for these corrections to be estimated accurately. Figures 5.1(a) and (b) compare the distributions of the p_{T} and pseudorapidity, η,[1] respectively, of the B^0 meson in real and simulated data. Discrepancies between the two samples can be seen, which are removed using the gradient boosted reweighting technique [75]. A weight is calculated for each simulated event such that the weighted distributions and their correlations in simulation match the data. Figures 5.1(c) and (d) show the weighted distributions; the correction factors determined in this section incorporate these weights.

5.1.1 Asymmetry corrections

The *CP* asymmetries are measured by comparing the yields of the decays of B^0 and $\overline{B}^0$ mesons. The relative yield depends not only on *CP* violation, but also on the following effects:

1. The relative production rate of B^0 and $\overline{B}^0$ mesons within the kinematic acceptance of the measurement;

2. The relative detection efficiency of B^0-meson and $\overline{B}^0$-meson decay products;

3. The relative efficiency of the PID requirements for B^0-meson and $\overline{B}^0$-meson decay products.

Each effect must be corrected for in the asymmetry calculation.

[1]The pseudorapidity of a particle is defined as $\eta = -\ln(\tan\frac{\theta}{2})$, where θ is the angle between the particle's momentum vector and the beam axis.

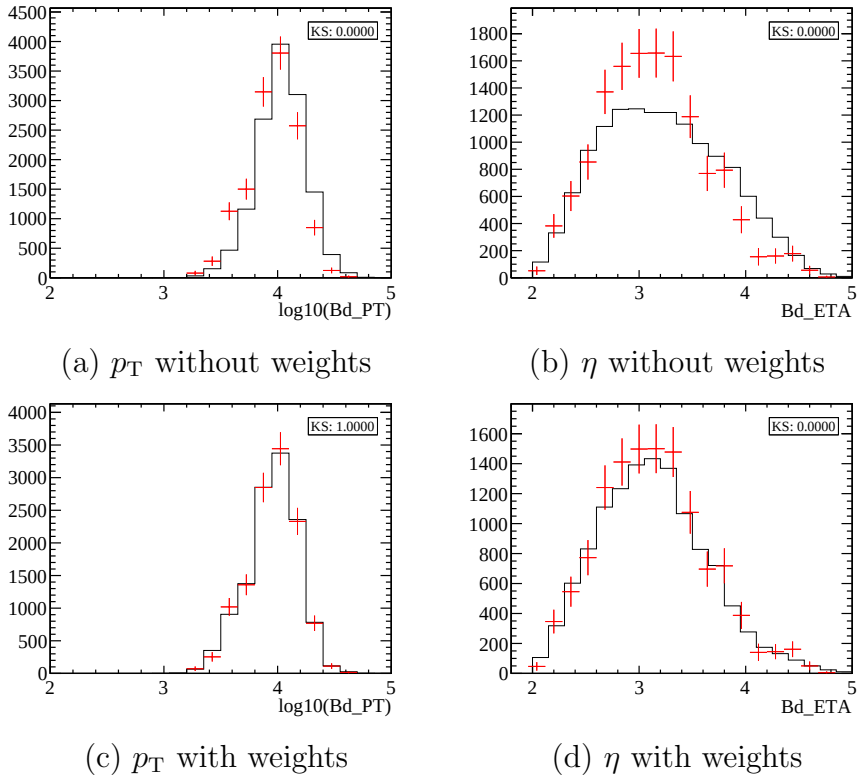

(a) p_{T} without weights

(b) η without weights

(c) p_{T} with weights

(d) η with weights

Figure 5.1: Comparisons of the B^0-meson transverse momentum (p_{T}) and pseudorapidity (η) distributions in background-subtracted data (red points) and simulated events (black histogram), before and after the simulated events are weighted to match the data: (a) p_{T} before weighting; (b) η before weighting; (c) p_{T} after weighting; (d) η after weighting.

Production asymmetry

The B^0–$\overline{B}^0$ production asymmetry at LHCb has been measured in bins of momentum and pseudorapidity using 8 TeV collision data [76]. A weighted-average production asymmetry of $A_{\text{prod}} = (-8 \pm 5) \times 10^{-3}$ is found for this analysis; the negative asymmetry means that B^0 mesons are produced slightly more frequently than $\overline{B}^0$ mesons within the kinematic acceptance of this measurement. No measurement has yet been performed with 13 TeV collisions, so the 8 TeV results are used for the full data set. When the associated systematic uncertainty is computed in Sect. 5.3, the uncertainty on the measurement is doubled for Run 2 in order to account for any small energy dependence.

Detection asymmetry

A detection asymmetry arises due to differences between the interaction cross-sections of matter and antimatter particles as they traverse the detector. It is predominantly caused by the shorter interaction length of K^- mesons compared with K^+ mesons.

The most precise measurements of detection asymmetry at LHCb are of the detection asymmetry between pairs of $K^-\pi^+$ and $K^+\pi^-$ mesons, $A_{K\pi}$. A value of $A_{K\pi}$ for the kinematic phase space used in this analysis is computed following the method used in Ref. [77]. Calibration samples of $D^+ \to K^-\pi^+\pi^+$ and $D^+ \to \overline{K}^0\pi^+$ decays are weighted to match the kinematics of kaons and pions in the signal data set, and used to measure the raw charge asymmetries $A_{\text{raw}}(K^-\pi^+\pi^+)$ and $A_{\text{raw}}(\overline{K}^0\pi^+)$, respectively. The detection asymmetry of $K^\mp\pi^\pm$ pairs is then calculated from

$$A_{K\pi} = A_{\text{raw}}(K^-\pi^+\pi^+) - A_{\text{raw}}(\overline{K}^0\pi^+) + A_{K^0}, \tag{5.1}$$

where A_{K^0} is the measured detection asymmetry in the decay $K^0 \to \pi^+\pi^-$ [77]. This gives $A_{K\pi} = (-1.0 \pm 0.5)\%$; the negative value suggests that $K^-\pi^+$ pairs interact with the detector material more frequently than $K^+\pi^-$ pairs. A correction of $A_{K\pi}$ is applied to the observables for each $K^\pm\pi^\mp$ pair in the final state.

Implementation of asymmetry corrections

For each asymmetry correction A, we can calculate the fractional increase a of the yield of B^0-meson decays with respect to $\overline{B}^0$-meson decays due to this correction from

$$a = \frac{1 - A}{1 + A}. \tag{5.2}$$

Production and detection asymmetry factors a_{prod} and a_{det} are calculated in this way, while a PID correction factor a_{PID} is computed from the ratios of the PID efficiencies for B^0-meson and $\overline{B}^0$-meson decays discussed in Sect. 5.1.2. We can then calculate the total correction factor a_{corr} for each D-meson decay mode:

$$a_{\text{corr}} = a_{\text{prod}} \times a_{\text{det}} \times a_{\text{PID}}. \tag{5.3}$$

The CP asymmetries $\mathcal{A}_{CP}$ are calculated from the raw yields using

$$\mathcal{A}_{CP} = \frac{a_{\text{corr}} N(\overline{B}^0) - N(B^0)}{a_{\text{corr}} N(\overline{B}^0) + N(B^0)}, \tag{5.4}$$

where $N(B^0)$ and $N(\overline{B}^0)$ are the raw yields of B^0-meson and $\overline{B}^0$-meson decays, respectively. We also calculate the total corrected flavour-summed yield, $\mathcal{N}$, for each mode via

$$\mathcal{N} = a_{\text{corr}} N(\overline{B}^0) + N(B^0), \tag{5.5}$$

which is used when calculating the GLW ratios $\mathcal{R}_{CP}$, as discussed in Sect. 5.1.2.

The ADS ratios $\mathcal{R}_{\pm}$ are corrected for a detection asymmetry between the suppressed and favoured modes, which have oppositely charged final-state particles. The ratio $\mathcal{R}^+$ is multiplied by a factor of $\frac{1-A_{K\pi}}{1+A_{K\pi}}$, and the ratio $\mathcal{R}^-$ is multiplied by a factor of $\frac{1+A_{K\pi}}{1-A_{K\pi}}$.

5.1.2 Ratio corrections

The ratios $\mathcal{R}_{CP}$ between the yields of the GLW modes and the favoured ADS modes are calculated using the asymmetry-corrected yields defined in Eq. 5.5. The yield

ratios are normalised using branching fractions and efficiencies:

$$\mathcal{R}_{CP}^{hh(\pi\pi)} = \frac{\mathcal{N}^{hh(\pi\pi)}}{\mathcal{N}^{K\pi(\pi\pi)}} \times \frac{\mathcal{B}(D^0 \to K^+\pi^+(\pi^+\pi^-))}{\mathcal{B}(D^0 \to h^+h^-(\pi^+\pi^-))} \times \frac{\epsilon(B^0 \to D(K^+\pi^-(\pi^+\pi^-))K^{*0})}{\epsilon(B^0 \to D(h^+h^-(\pi^+\pi^-))K^{*0})}, \tag{5.6}$$

where the branching fractions $\mathcal{B}$ are given in Table 5.1, and ϵ is the overall efficiency of the selection including the detector acceptance, selection requirements, and PID cuts.

Table 5.1: Branching fractions for the D-meson decays considered in this analysis, taken from Ref. [71].

D-meson decay	Branching fraction (%)
$D^0 \to K^-\pi^+$	3.89 ± 0.04
$D^0 \to K^+K^-$	0.397 ± 0.007
$D^0 \to \pi^+\pi^-$	0.141 ± 0.003
$D^0 \to K^-\pi^+\pi^-\pi^+$	8.11 ± 0.15
$D^0 \to \pi^+\pi^-\pi^+\pi^-$	0.745 ± 0.020

Selection efficiency

The selection efficiency is the probability that a true signal decay produced at LHCb is detected and passes all of the selection requirements. It is the product of the geometric acceptance efficiency of the LHCb detector and the probability that an accepted candidate passes the reconstruction and selection requirements. Both are calculated with simulated signal events. This calculation does not account for the PID requirements, as the PID variables are poorly modelled in simulation and are dealt with separately using a data-driven method.

The geometric acceptance efficiency, ϵ_{acc}, is the fraction of decay products entering the LHCb detector acceptance. It is calculated at the generation stage of the simulation. The selection efficiency, ϵ_{sel}, is the ratio between the number of selected simulated events and the number of events generated within the detector acceptance. These efficiencies and their product, ϵ_{tot}, are given in Table 5.2 for each D-meson mode and data-taking period, with uncertainties assigned to account for the finite sizes of the simulated samples.

Table 5.2: Geometric acceptance efficiencies, selection efficiencies, and their product, measured with simulated events for each D-meson mode and data-taking period.

Data-taking period	D mode	$\epsilon_{\text{acc}}(\%)$	$\epsilon_{\text{sel}}(\%)$	$\epsilon_{\text{tot}}(\%)$
Run 1	$K\pi$	16.79 ± 0.02	1.147 ± 0.011	0.1926 ± 0.0019
	KK	17.54 ± 0.04	1.049 ± 0.015	0.1841 ± 0.0026
	$\pi\pi$	16.32 ± 0.06	1.114 ± 0.015	0.1818 ± 0.0026
	$K\pi\pi\pi$	15.62 ± 0.02	0.330 ± 0.003	0.0515 ± 0.0005
Run 2	$K\pi$	17.51 ± 0.04	1.290 ± 0.010	0.2259 ± 0.0018
	KK	18.24 ± 0.04	1.137 ± 0.010	0.2073 ± 0.0018
	$\pi\pi$	16.92 ± 0.04	1.271 ± 0.010	0.2151 ± 0.0017
	$K\pi\pi\pi$	16.56 ± 0.03	0.494 ± 0.004	0.0818 ± 0.0007
	$\pi\pi\pi\pi$	15.90 ± 0.03	0.515 ± 0.004	0.0819 ± 0.0007

PID efficiency

The efficiencies of the PID requirements vary between the D-meson modes, and must therefore be included in the normalisation of the yield ratios. The difference in the efficiencies for B^0-meson and $\overline{B}^0$-meson decays is also accounted for when calculating the *CP* asymmetries, although it is found to be very small. The PID efficiencies are calculated using a calibration sample of $D^{*\pm} \to D(K^{\mp}\pi^{\pm})\pi^{\pm}$ decays, which are selected without the use of any PID variables and background-subtracted. The efficiencies of various PID requirements are calculated with these events. The PID efficiency depends on the momentum and pseudorapidity of the final-state tracks, so the calibration sample is binned in these variables, and a weighted average using the kinematics of simulated $B^0 \to DK^{*0}$ decays is used to calculate the efficiencies in this analysis.

Table 5.3 gives the PID efficiencies for each D-meson mode, data-taking period, and B-meson flavour. The uncertainties account for the potential bias due to the choice of binning scheme and the uncertainty associated with the background-subtraction procedure used on the calibration sample. The efficiencies are larger in Run 2 due to the increased collision energy, improved trigger scheme, and intrinsic improvements to the RICH detector through the removal of the aerogel radiator [61].

Table 5.3: PID efficiencies in % for each D-meson-decay, data-taking-period, and B-meson-flavour category, calculated using calibration samples weighted to match the momentum and pseudorapidity distributions of simulated events.

***D* mode**	**Run 1**		**Run 2**	
	B^0	$\overline{B}^0$	B^0	$\overline{B}^0$
$K\pi$	66.3 ± 0.4	66.8 ± 0.4	77.5 ± 0.2	77.3 ± 0.2
KK	73.0 ± 0.4	71.9 ± 0.5	79.9 ± 0.2	79.9 ± 0.2
$\pi\pi$	60.7 ± 0.3	60.6 ± 0.1	75.0 ± 0.1	75.1 ± 0.1
$K\pi\pi\pi$	56.9 ± 0.6	56.4 ± 0.5	73.8 ± 0.5	73.8 ± 0.3
4π	n/a	n/a	75.9 ± 0.2	76.1 ± 0.3

5.2 Validation of the invariant-mass fit

To validate the fitting procedure, 3000 pseudoexperiments are generated according to the model in Sect. 4.2 with all free parameters fixed to the values found in the fit to data and fitted using the same model. Around 95% of the fits converge and have good-quality covariance matrices.

The validity of the fit is tested by examining the distribution of the pull P_x for each parameter x, defined as

$$P_x = \frac{x_{\text{fit}} - x_{\text{gen}}}{\sigma_x}, \tag{5.7}$$

where x_{gen} is the value used to generate the pseudoexperiment, and x_{fit} and σ_x are the central value and statistical uncertainty, respectively, obtained from the fit. In an unbiased fit, the pull distribution should obey a Gaussian function centred at zero with unit width. Figure 5.2 shows the distributions of x_{fit}, σ_x, and P_x for the *CP* asymmetries in the GLW modes. The pull distributions are fit with Gaussian functions, which in all cases are found to have means consistent with zero and widths consistent with unity.

5.3 Systematic uncertainties

The measured observables are either asymmetries or ratios of yields between similar final states, and are thus robust against systematic biases. Nonetheless, small uncer-

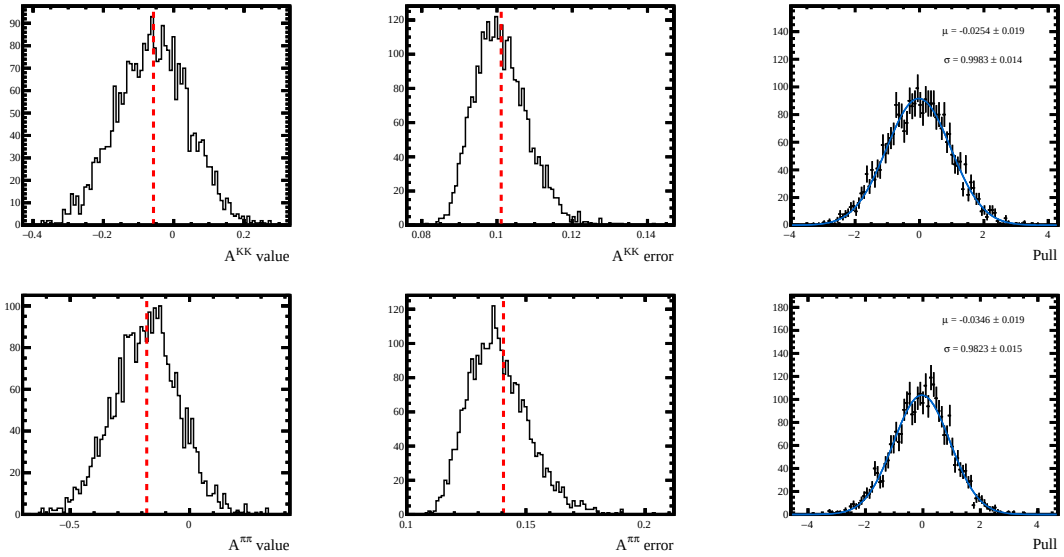

Figure 5.2: Distributions of (left) central value, (centre) statistical uncertainty and (right) pull of the *CP* observables (top) $\mathcal{A}_{CP}^{KK}$ and (bottom) $\mathcal{A}_{CP}^{\pi\pi}$ from fits to 3000 pseudoexperiments. The red dotted lines indicate the central values and statistical uncertainties found in the fit to real data.

tainties arise due to the input of correction factors, assumptions in the fit, and the possibility of charmless backgrounds.

Each systematic uncertainty is evaluated using a data-driven method, unless otherwise stated. For each fixed parameter, the data are fit many times with the value of the parameter randomly shifted around its central value. The shifts are generated according to a Gaussian function centred at zero, with a width equal to the uncertainty of the parameter. If several fixed parameters are correlated, shifts are generated simultaneously using their covariance matrix. The distribution of each observable in 1000 fits to data with smeared parameters is fitted with a Gaussian function, whose width is taken to be the systematic uncertainty.

Correction factors

As discussed in Sect. 5.1, the calculation of the *CP* observables involves correcting the raw yield ratios and asymmetries using the relative branching fractions, selection efficiencies, PID efficiencies, production asymmetries, and detection asymmetries. The

uncertainty of each correction factor is propagated to the observables. The branching fractions produce to the largest systematic uncertainties on the GLW ratios, while the production and detection asymmetries produce the largest uncertainties on the asymmetry observables; however, these uncertainties are at least an order of magnitude smaller than the statistical uncertainties.

Fit-related systematics

Systematic uncertainties are assigned for the fixed shape parameters in the invariant-mass model. The central values and uncertainties of these parameters are derived from fits to simulated samples, as discussed in Sect. 4.2. The fixed tail parameters of the signal shape are treated as a single source of systematic uncertainty. The uncertainties due to all fixed parameters related to the background shapes are treated simultaneously, apart from those for the partially reconstructed $\overline{B}{}^0_s \to D^* K^{*0}$ background, which is an important source of contamination that overlaps with the signal region and is therefore treated separately.

Various asymmetries and ratios between yields in different fit categories are fixed. The relative proportion of partially reconstructed $D^* \to D\pi^0$ and $D^* \to D\gamma$ decays is fixed from branching fractions and efficiencies, as discussed in Sect. 4.2.4. A correction to the relative yield of misidentified $B^0 \to D\pi^+\pi^-$ decays between Run 1 and Run 2 is calculated in Sect. 4.2.6. The relative yields and *CP* asymmetries of the partially reconstructed $B^+ \to DK^+\pi^-\pi^+$ background are fixed to the values measured in Ref. [74], with the uncertainties doubled to account for the fact that there are possible differences in the phase-space acceptance between the two analyses.

The selection requirements for the ADS modes are chosen such that the ratios $\mathcal{R}_\pm$ require minimal corrections. Their total systematic uncertainties are thus smaller than those of the other observables, and are dominated by the uncertainties due to the fixed shape and yield parameters in the fit.

Charmless background

The study of charmless decays reported in Sect. 4.1.4 finds evidence of a charmless background in some D-meson modes before the final selection is applied. While this background appears to be reduced to a negligible level by a requirement on the flight-distance significance (FDS) of the D meson, the uncertainties of the background yields are relatively large due to the limited sizes of the sideband samples used in the study. The possibility of residual charmless events is therefore considered as a source of systematic uncertainty.

Random numbers of charmless decays are generated in each affected D-meson mode, according a Gaussian function with a mean equal to the expected number of charmless candidates after the FDS cut and a width equal to the corresponding uncertainty. The generated values are rounded to whole numbers and distributed randomly between the B^0 and $\overline{B}^0$ categories, where they are added to the signal yields. Events are added to the B_s^0 and $\overline{B}_s^0$ signal peaks in the same way in the πK and $\pi K\pi\pi$ modes, where evidence of charmless B_s^0 decays was observed prior to the FDS cut. 1000 pseudoexperiments are generated in this way and fitted with the default invariant-mass model, which does not include a charmless component. The difference in the mean value of each observable in pseudoexperiments generated with and without the charmless contamination is taken to be the systematic uncertainty.

Summary of systematic uncertainties

Table 5.4 gives the systematic uncertainties for each observable. Systematic uncertainties that are more than two orders of magnitude smaller than the statistical uncertainty are considered to be negligible and ignored. The non-negligible uncertainties are added in quadrature to give the total systematic uncertainty, which in all cases is considerably smaller than the statistical uncertainty.

Table 5.4: Systematic uncertainties for the observables. Uncertainties are shown if they are larger than 1% of the statistical uncertainty. The total systematic uncertainty is calculated by summing all sources in quadrature. Statistical uncertainties are given for reference.

Source	$\mathcal{A}_{CP}^{KK}$	$\mathcal{A}_{CP}^{\pi\pi}$	$\mathcal{R}_{CP}^{KK}$	$\mathcal{R}_{CP}^{\pi\pi}$	$\mathcal{A}_{CP}^{4\pi}$	$\mathcal{R}_{CP}^{4\pi}$	$\mathcal{R}_{+}^{\pi K}$	$\mathcal{R}_{-}^{\pi K}$	$\mathcal{R}_{+}^{\pi K\pi\pi}$	$\mathcal{R}_{-}^{\pi K\pi\pi}$	$\mathcal{A}_{\rm ADS}^{K\pi}$	$\mathcal{A}_{\rm ADS}^{K\pi\pi\pi}$
Selection efficiency	-	-	0.008	0.011	-	0.012	-	-	-	-	-	-
PID efficiency	0.002	-	0.004	0.004	0.002	0.007	-	-	-	-	0.002	0.003
Branching fractions	-	-	0.017	0.025	-	0.031	-	-	-	-	-	-
Production asymmetry	0.006	0.006	-	-	0.010	-	-	-	-	-	0.006	0.006
Detection asymmetry	0.004	0.004	0.004	0.007	0.007	0.007	< 0.001	< 0.001	< 0.001	< 0.001	0.008	0.008
Signal shape parameters	-	-	-	-	-	-	< 0.001	< 0.001	< 0.001	< 0.001	-	-
$B_s^0 \to D^* K^{*0}$ shape parameters	-	-	0.001	-	-	-	< 0.001	< 0.001	< 0.001	< 0.001	-	-
Other background shape parameters	-	-	-	0.003	-	0.003	< 0.001	0.001	0.001	0.002	-	-
$D^* \to D^0\gamma/\pi^0$ inputs	-	-	0.002	-	-	0.002	0.002	0.002	0.002	0.002	-	-
$B \to D\pi\pi$ PID correction	-	-	-	-	0.006	-	< 0.001	< 0.001	-	-	-	< 0.001
$B \to DK\pi\pi$ inputs	-	-	0.001	0.002	-	0.002	-	-	-	-	-	-
Charmless background	0.003	0.002	-	0.003	0.004	0.011	< 0.001	< 0.001	-	< 0.001	0.002	0.001
Total systematic	0.01	0.01	0.02	0.03	0.01	0.04	0.002	0.003	0.002	0.003	0.010	0.010
Statistical	0.10	0.14	0.10	0.19	0.15	0.16	0.021	0.021	0.026	0.025	0.027	0.032

5.4 Summary of measured observables

The measured *CP* observables are

$$\begin{aligned}
\mathcal{A}_{CP}^{KK} &= -0.05 \pm 0.10 \pm 0.01, \\
\mathcal{A}_{CP}^{\pi\pi} &= -0.18 \pm 0.14 \pm 0.01, \\
\mathcal{R}_{CP}^{KK} &= 0.92 \pm 0.10 \pm 0.02, \\
\mathcal{R}_{CP}^{\pi\pi} &= 1.32 \pm 0.19 \pm 0.03, \\
\mathcal{A}_{CP}^{4\pi} &= -0.03 \pm 0.15 \pm 0.01, \\
\mathcal{R}_{CP}^{4\pi} &= 1.01 \pm 0.16 \pm 0.04, \\
\mathcal{R}_{+}^{\pi K} &= 0.064 \pm 0.021 \pm 0.002, \\
\mathcal{R}_{-}^{\pi K} &= 0.095 \pm 0.021 \pm 0.003, \\
\mathcal{R}_{+}^{\pi K\pi\pi} &= 0.074 \pm 0.026 \pm 0.002, \\
\mathcal{R}_{-}^{\pi K\pi\pi} &= 0.072 \pm 0.025 \pm 0.003, \\
\mathcal{A}_{\rm ADS}^{K\pi} &= 0.047 \pm 0.027 \pm 0.010, \\
\mathcal{A}_{\rm ADS}^{K\pi\pi\pi} &= 0.037 \pm 0.032 \pm 0.010,
\end{aligned}$$

where the first uncertainty is statistical and the second is systematic. Table 5.5 gives the combined statistical and systematic correlation coefficients. The values of $\mathcal{R}_{\pm}^{\pi K}$ and $\mathcal{R}_{\pm}^{\pi K\pi\pi}$ are used to calculate the suppressed-mode ADS observables, which are found to be

$$\begin{aligned}
\mathcal{A}_{\rm ADS}^{\pi K} &= 0.19 \pm 0.19 \pm 0.01, \\
\mathcal{R}_{\rm ADS}^{\pi K} &= 0.080 \pm 0.015 \pm 0.002, \\
\mathcal{A}_{\rm ADS}^{\pi K\pi\pi} &= -0.01 \pm 0.24 \pm 0.01, \\
\mathcal{R}_{\rm ADS}^{\pi K\pi\pi} &= 0.073 \pm 0.018 \pm 0.002.
\end{aligned}$$

All of the measured *CP* asymmetries are compatible with zero to within two standard deviations. The values of the two-body GLW asymmetries and ratios, $\mathcal{A}_{CP}^{hh}$ and $\mathcal{R}_{CP}^{hh}$, are found to be consistent between the two modes to within 0.8 and 1.8 standard deviations, respectively. The results for $D \to \pi^+\pi^-\pi^+\pi^-$ decays are in agreement with these values after correcting for the known *CP*-even content of this final state. The interpretation of the results in terms of γ is discussed in Chap. 8.

Table 5.5: Combined statistical and systematic correlation matrix for the *CP* observables.

	$\mathcal{A}_{CP}^{KK}$	$\mathcal{A}_{CP}^{\pi\pi}$	$\mathcal{R}_{CP}^{KK}$	$\mathcal{R}_{CP}^{\pi\pi}$	$\mathcal{A}_{CP}^{4\pi}$	$\mathcal{R}_{CP}^{4\pi}$	$\mathcal{R}_{+}^{\pi K}$	$\mathcal{R}_{-}^{\pi K}$	$\mathcal{R}_{+}^{\pi K\pi\pi}$	$\mathcal{R}_{-}^{\pi K\pi\pi}$	$\mathcal{A}_{\rm ADS}^{K\pi}$	$\mathcal{A}_{\rm ADS}^{K\pi\pi\pi}$
$\mathcal{A}_{CP}^{KK}$	1.00	0.00	0.03	−0.01	0.00	0.00	0.00	−0.01	−0.01	−0.01	−0.01	−0.01
$\mathcal{A}_{CP}^{\pi\pi}$	0.00	1.00	0.01	0.06	0.00	0.00	0.00	0.00	0.00	0.00	−0.01	−0.01
$\mathcal{R}_{CP}^{KK}$	0.03	0.01	1.00	0.04	0.00	0.03	0.02	0.02	0.00	0.00	−0.04	−0.03
$\mathcal{R}_{CP}^{\pi\pi}$	−0.01	0.06	0.04	1.00	0.00	0.04	0.01	0.03	0.02	0.02	0.03	0.03
$\mathcal{A}_{CP}^{4\pi}$	0.00	0.00	0.00	0.00	1.00	0.01	0.00	0.00	0.00	0.00	0.00	0.00
$\mathcal{R}_{CP}^{4\pi}$	0.00	0.00	0.03	0.04	0.01	1.00	0.01	0.02	0.02	0.03	0.02	0.01
$\mathcal{R}_{+}^{\pi K}$	0.00	0.00	0.02	0.01	0.00	0.01	1.00	0.05	0.01	0.01	0.08	0.00
$\mathcal{R}_{-}^{\pi K}$	−0.01	0.00	0.02	0.03	0.00	0.02	0.05	1.00	0.02	0.02	−0.08	0.03
$\mathcal{R}_{+}^{\pi K\pi\pi}$	−0.01	0.00	0.00	0.02	0.00	0.02	0.01	0.02	1.00	0.06	0.02	0.11
$\mathcal{R}_{-}^{\pi K\pi\pi}$	−0.01	0.00	0.00	0.02	0.00	0.03	0.01	0.02	0.06	1.00	0.03	−0.06
$\mathcal{A}_{\rm ADS}^{K\pi}$	−0.01	−0.01	−0.04	0.03	0.00	0.02	0.08	−0.08	0.02	0.03	1.00	0.08
$\mathcal{A}_{\rm ADS}^{K\pi\pi\pi}$	−0.01	−0.01	−0.03	0.03	0.00	0.01	0.00	0.03	0.11	−0.06	0.08	1.00

5.5 Statistical significance of previously unobserved decays

The πK, $\pi K\pi\pi$ and 4π modes had not been observed in $B^0 \to DK^{*0}$ decays prior to this analysis. The significances of the signal yields in these modes are calculated using Wilks' theorem [78], which defines the significance as

$$\text{Significance} = \sqrt{2\log(L^{\max}) - 2\log(L_0^{\max})}, \tag{5.8}$$

where $L^{\max}$ is the maximised likelihood in a fit that includes the decay of interest, and $L_0^{\max}$ is the maximised likelihood in the same fit with the yield of the decay of interest fixed to zero. This calculation only accounts for the statistical uncertainty of the yield; to account for the systematic uncertainty, the likelihood profile of the yield is convolved with a Gaussian function with a standard deviation equal to the systematic uncertainty, and the significance is calculated from the convolved profile.

This procedure yields a significance of 8.4σ for $B^0 \to D(\pi^+\pi^-\pi^+\pi^-)K^{*0}$ decays, 5.8σ for $B^0 \to D(\pi^+K^-)K^{*0}$ decays, and 4.4σ for $B^0 \to D(\pi^+K^-\pi^+\pi^-)K^{*0}$ decays, constituting the first observations of the first two modes and strong evidence for the presence of the suppressed four-body ADS mode.

Chapter 6

Selection and parametrisation of $B^0 \to DK^{*0}$ decays with three-body D-meson final states

A measurement complementary to the ADS/GLW analysis is performed using the three-body self-conjugate D-meson decays $D \to K^0_S\pi^+\pi^-$ and $D \to K^0_S K^+ K^-$. This measurement uses $9\,\text{fb}^{-1}$ of pp collision data collected by the LHCb experiment from 2011–2012 and 2015–2018. The GGSZ observables $x_\pm \equiv r_{B^0}\cos(\delta_{B^0} \pm \gamma)$ and $y_\pm \equiv r_{B^0}\sin(\delta_{B^0} \pm \gamma)$ are measured, which depend on the relative decay rates of B^0 and $\overline{B}^0$ mesons in bins of the D-meson Dalitz plot.

6.1 Analysis strategy

The yields of the decays of B^0 and $\overline{B}^0$ mesons in bin i of the Dalitz plot are related to the integrated squared amplitudes of D-meson decays in that bin, $T_{\pm i}$, via Eqs. 2.58 and 2.59. In practice, the Dalitz plot distributions are distorted by variations in selection efficiency across the phase space. Writing the efficiency profile as $\eta(m^2_-, m^2_+)$, we replace $T_{\pm i}$ with new quantities

$$F_{\pm i} \equiv \frac{\int_{\pm i} \mathrm{d}m^2_- \mathrm{d}m^2_+ \, a^2(m^2_-, m^2_+)\eta(m^2_-, m^2_+)}{\sum_j \int_j \mathrm{d}m^2_- \mathrm{d}m^2_+ \, a^2(m^2_-, m^2_+)}, \tag{6.1}$$

where the sum $\sum_j$ is over all bins. The parameter F_i is the fraction of selected events involving a D^0 meson in bin i, accounting for all amplitude and efficiency effects. The amplitudes for D^0 and $\overline{D}^0$ mesons are related under the transformation $m^2_- \leftrightarrow m^2_+$,

and we can reasonably assume that the efficiency profile $\eta(m_-^2, m_+^2)$ is symmetric under this transformation[1], so the fraction of selected events involving a $\overline{D}^0$ meson in bin i is F_{-i}. In the absence of interference and CP violation, the fraction of selected $\overline{B}^0$-meson decays in bin i would be F_i, and the fraction of selected B^0-meson decays in bin i would be F_{-i}.

In the case of non-negligible interference and CP violation, the yields of the decays of B^0 and $\overline{B}^0$ mesons in each bin are given by

$$N_{\pm i}(B^0) = n\left[F_{\mp i} + (x_+^2 + y_+^2)F_{\pm i} + 2\kappa\sqrt{F_{+i}F_{-i}}(x_+c_{\pm i} + y_+s_{\pm i})\right], \tag{6.2}$$

$$N_{\pm i}(\overline{B}^0) = \overline{n}\left[F_{\pm i} + (x_-^2 + y_-^2)F_{\mp i} + 2\kappa\sqrt{F_{+i}F_{-i}}(x_-c_{\pm i} + y_-s_{\pm i})\right], \tag{6.3}$$

where n and $\overline{n}$ are normalisation constants for the decays of B^0 and $\overline{B}^0$ mesons, respectively. The strong-phase parameters c_i and s_i have been measured by the CLEO and BESIII experiments [42, 43], as discussed in Sect. 2.7.3.

In principle, the F_i values could be measured in a fit today; however, this is not feasible due to the limited statistics of $B^0 \to DK^{*0}$ decays. In previous model-independent GGSZ analyses, such as the study presented in Ref. [51], the F_i values were measured using flavour-tagged decays in a semileptonic control channel, $B^0 \to D^{*-}(\overline{D}^0\pi^-)\mu^+\nu_\mu$. No interference occurs in these decays, so the Dalitz plot distribution depends only on the D-meson amplitude and efficiency profile, and the fraction of B^0-meson decays in bin i is equal to F_{-i}. However, it was necessary to correct the semileptonic F_i values for efficiency differences between $B^0 \to D^{*-}\mu^+\nu_\mu$ and $B^0 \to DK^{*0}$ decays. The calculation of this correction required very large simulated samples of both decays, which were expensive and time-consuming to produce. The uncertainty associated with this correction procedure was the dominant systematic uncertainty on the results in Ref. [51].

In the most recent GGSZ analysis of $B^+ \to Dh^+$ decays [79], an alternative

[1] In principle, the efficiency profile maybe not be exactly symmetric; for example, due to the different interaction lengths of K^- and K^+ mesons. Differences between $\eta(m_-^2, m_+^2)$ and $\eta(m_+^2 m_-^2)$ have been studied in the analysis of $B^+ \to DK^+$ decays [79], and are found to be negligible even in large data samples.

method is used for the first time. A simultaneous fit is performed to $B^+ \to DK^+$ decays, which are sensitive to γ with $r_{B^+} \sim 0.1$, and $B^+ \to D\pi^+$ decays, which are less sensitive with $r_{B^+} \sim 0.005$. The $B^+ \to D\pi^+$ decay has a large yield of around 200 000 events, which is sufficient to determine the F_i values from the fit in addition to the *CP*-violation parameters for both decays.

This technique assumes that the efficiency profiles of $B^+ \to DK^+$ and $B^+ \to D\pi^+$ decays are identical, allowing the same F_i values to be used for both. This is verified using samples of simulated events for each decay that pass the selection requirements. The Dalitz plot distributions of the samples are found to be extremely similar, which suggests that the efficiency profile has little dependence on the initial B-meson decay. We might therefore assume that $B^0 \to DK^{*0}$ decays have the same efficiency profile, provided that very similar selection requirements are used. If this is the case, we can use the F_i values measured with $B^+ \to Dh^+$ decays in our $B^0 \to DK^{*0}$ analysis without applying any efficiency corrections. This removes the need for large simulated samples and reduces the systematic uncertainty on our measurement.

Figures 6.1 and 6.2 show the Dalitz plot distributions of simulated $B^0 \to DK^{*0}$ and $B^+ \to D\pi^+$ decays selected with the requirements discussed in Sect. 6.2, and the ratio between them. The decays are generated uniformly across the Dalitz plot without the inclusion of any intermediate resonances, so any variation in the Dalitz plot distribution after the selection requirements corresponds to the efficiency profile, $\eta(m_-^2, m_+^2)$. For each distribution, the p-value from a χ^2 comparison test is shown. All of the p-values are reasonably large, and no clear trends are seen in the ratio plots.

The compatibility of the samples is further tested in the one-dimensional distributions of $m^2(K^0_S h^+)$, $m^2(K^0_S h^-)$, and $m^2(h^+h^-)$, shown in Figs 6.3 and 6.4. The Kolmogorov-Smirnov test is used to estimate the p-values, which indicate reasonable agreement. Based on these studies, the use of F_i values measured in $B^+ \to Dh^+$ decays in our analysis of $B^0 \to DK^{*0}$ decays is deemed to be valid. Small discrepancies in the distributions of $m^2(h^+h^-)$ are accounted for as a source of systematic uncertainty.

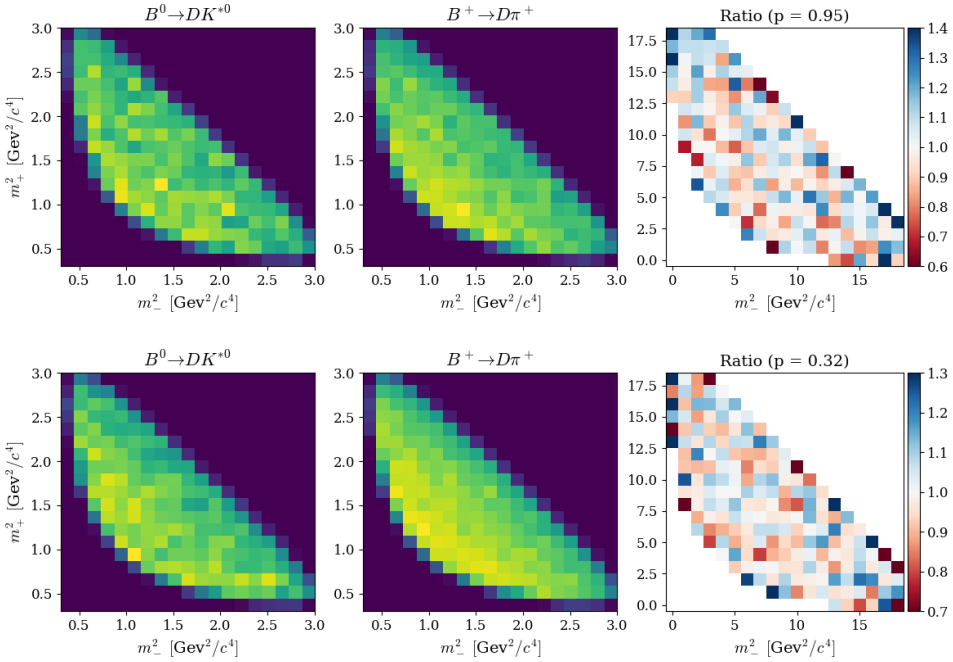

Figure 6.1: Efficiency profiles of selected simulated (left) $B^0 \to DK^{*0}$ and (centre) $B^+ \to D\pi^+$ decays with $D \to K^0_S\pi^+\pi^-$, and (right) the ratio of the two distributions. The K^0_S meson is reconstructed from (top) long tracks and (bottom) downstream tracks.

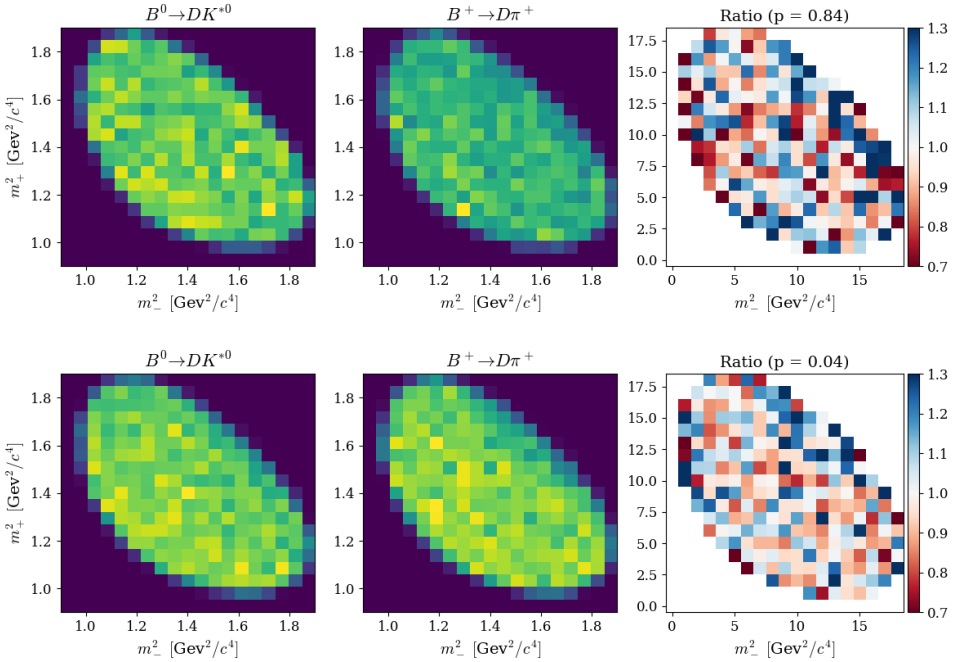

Figure 6.2: Efficiency profiles of selected simulated (left) $B^0 \to DK^{*0}$ and (centre) $B^+ \to D\pi^+$ decays with $D \to K^0_S K^+ K^-$, and (right) the ratio of the two distributions. The K^0_S meson is reconstructed from (top) long tracks and (bottom) downstream tracks.

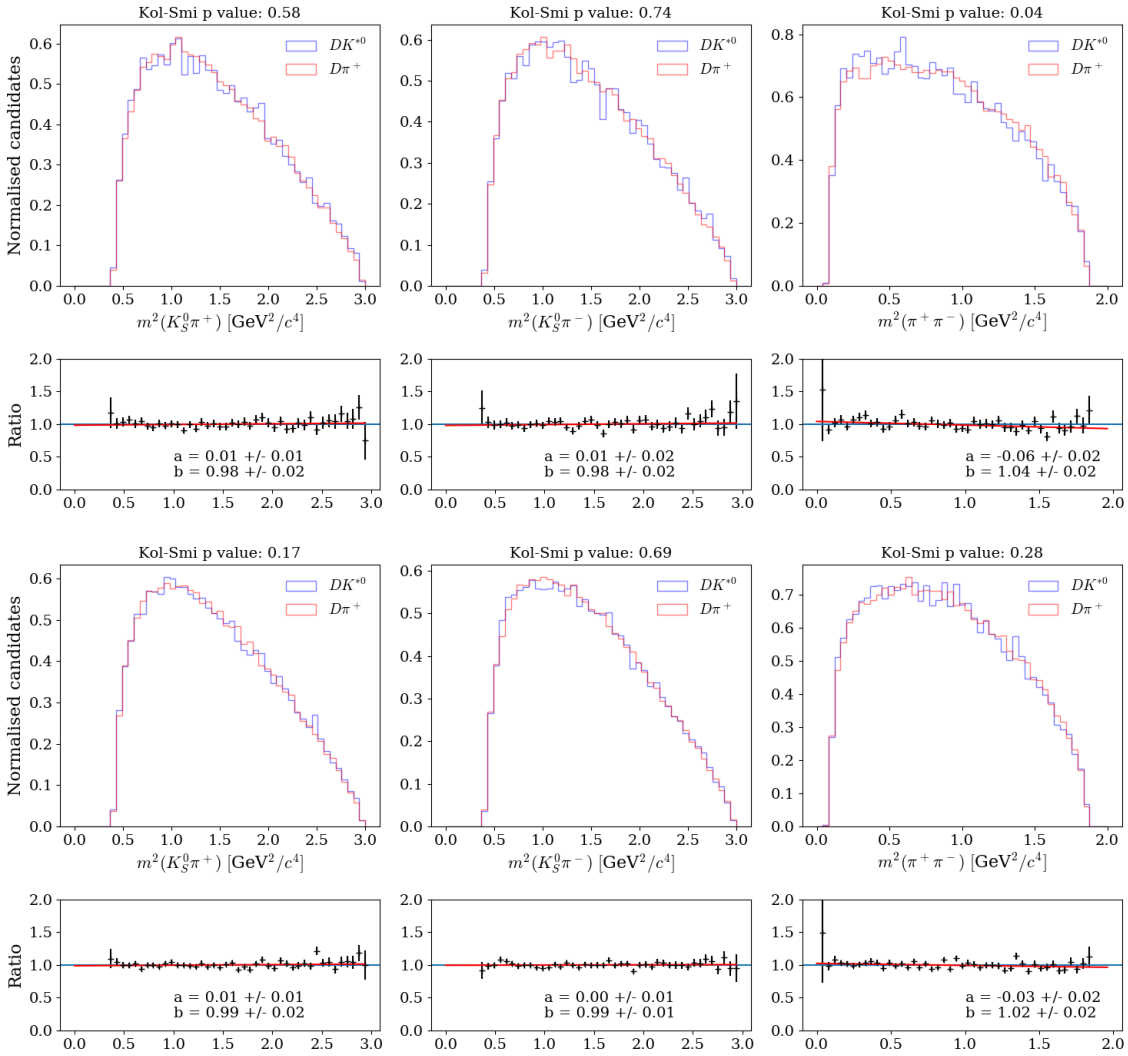

Figure 6.3: Comparisons of the distributions of the invariant masses of two-body combinations of D-meson products in simulated $B^0 \to DK^{*0}$ (blue) and $B^+ \to D\pi^+$ (red) decays with $D \to K^0_S\pi^+\pi^-$. The K^0_S meson is reconstructed from (top) long tracks and (bottom) downstream tracks. The ratios between the distributions are fitted with straight lines.

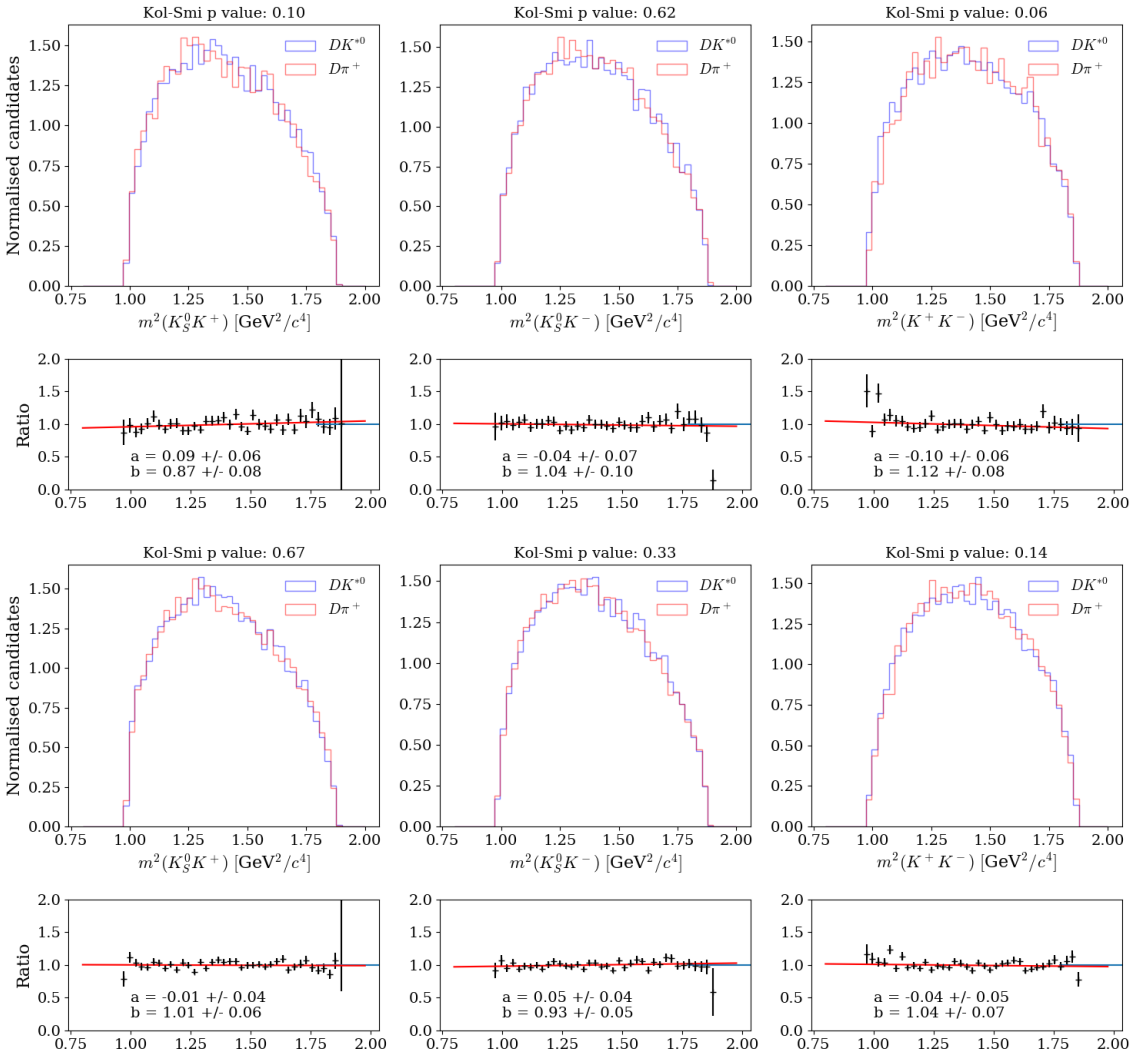

Figure 6.4: Comparisons of the distributions of the invariant masses of two-body combinations of D-meson products in simulated $B^0 \to DK^{*0}$ (blue) and $B^+ \to D\pi^+$ (red) decays with $D \to K^0_S K^+ K^-$. The K^0_S meson is reconstructed from (top) long tracks and (bottom) downstream tracks. The ratios between the distributions are fitted with straight lines.

The analysis method is as follows:

1. Select $B^0 \to D(K^0_S h^+ h^-)K^{*0}$ candidates using kinematic requirements similar to those used in the $B^+ \to Dh^+$ analysis;

2. Perform a global invariant-mass fit to selected candidates in all Dalitz bins at once, using a PDF based on the model developed in Chap. 4 for the ADS/GLW modes;

3. Split the candidates by B-meson flavour and D-meson Dalitz plot bin, and fit the invariant-mass distribution in each category to determine $x_\pm$ and $y_\pm$;

4. Correct $x_\pm$ and $y_\pm$ for any bias in the fit and evaluate systematic uncertainties.

Candidate selection is summarised in Sect. 6.2, and the global invariant-mass fit is discussed in Sect. 6.3. Chapter 7 presents the binned invariant-mass fit and measured observables.

6.2 Candidate selection

Candidate decays are formed in a reconstruction and stripping procedure similar to that of the ADS/GLW candidates, and are required to satisfy the trigger requirements discussed in Sect. 4.1.1. The K^0_S meson is reconstructed in the decay $K^0_S \to \pi^+\pi^-$, and is categorised as "long-long" (LL) if two long pion tracks are used, or "down-down" (DD) if two downstream pion tracks are used; the types of tracks are defined in Sect. 3.4. The track-type categories are treated separately, as LL candidates have a better momentum resolution than DD candidates.

The DecayTreeFitter framework is used to refit the decay chain with the masses of the D and K^0_S mesons fixed to their known values (labelled the `D0const` and `KS0const` constraints, respectively) and the momentum vector of the B^0 meson constrained to be parallel to a vector connecting the PV to its decay vertex (labelled the `PVconst` constraint). The refit improves the resolution of the B^0-meson invariant

mass and Dalitz plot coordinates, and the `D0const` constraint ensures that candidates fall within the kinematically allowed phase space of $D \to K^0_S h^+ h^-$ decays. Separate refits are performed with only the `D0const` and `PVconst` constraints to improve the resolution of the K^0_S-meson-mass variable, and with only the `KS0const` and `PVconst` constraints to improve the resolution of the D-meson-mass variable.

6.2.1 Rectangular cuts

Candidate K^{*0} mesons are selected within $\pm 50\,\text{MeV}/c^2$ of the nominal K^{*0}-meson mass, with a helicity angle requirement of $|\cos(\theta^*)| > 0.4$; this matches the kinematic selection used to determine the coherence factor in Ref. [45]. The kaon from the decay of the K^{*0} meson must satisfy $\text{DLL}_K > 5$, and the pion must satisfy $\text{DLL}_K < 3$.

All further rectangular cuts are based on the selection of $B^+ \to Dh^+$ decays in Ref. [79]. Any cuts applied to the h^+ meson (known as the "bachelor" particle) are here applied to the kaon from the decay of the K^{*0} meson. The rectangular cuts are summarised in Table. 6.1, and include:

- Cuts on the refit invariant masses of the D and K^0_S mesons;
- Loose cuts on the kaons in the $D \to K^0_S K^+ K^-$ mode to suppress cross-feed from misidentified $D \to K^0_S \pi^+ \pi^-$ decays;
- A cut on the flight-distance significance of the D meson to suppress charmless background;
- A cut on the flight-distance χ^2 of the K^0_S meson, which is a measure of the compatibility of its production and decay vertices, to suppress backgrounds from $D \to 4\pi$ and $D \to \pi\pi KK$ decays.

6.2.2 Boosted decision tree

To suppress combinatorial background, weights from a gradient boosted decision tree developed by Mikkel Bjørn for the $B^+ \to Dh^+$ analysis [79] are applied to the $B^0 \to$

Table 6.1: Summary of the rectangular cuts used to select $B^0 \to D(K^0_S h^+ h^-)K^{*0}$ decays. The parameters $m_{\rm PDG}$ represent known particle masses taken from Ref. [71]. All cuts except those used for the selection of the K^{*0} meson are taken from Ref. [79].

Variable	Selection requirement
K^{*0}-meson selection cuts	
$\lvert m(K^{*0}) - m_{\rm PDG}(K^{*0})\rvert$	$< 50\,{\rm MeV}/c^2$
$\lvert\cos(\theta^*)\rvert$	> 0.4
$K^{\pm}_{K^{*0}}$ DLL$_K$	> 5
$\pi^{\pm}_{K^{*0}}$ DLL$_K$	< 3
Base cuts	
$\lvert m(D) - m_{\rm PDG}(D^0)\rvert$	$< 25\,{\rm MeV}/c^2$
$\lvert m(K^0_S) - m_{\rm PDG}(K^0_S)\rvert$	$< 15\,{\rm MeV}/c^2$
DecayTreeFit converged	*true*
$K^{\pm}_{K^{*0}}$ momentum	$< 100\,{\rm GeV}/c$
$K^{\pm}_{D}$ momentum	$< 100\,{\rm GeV}/c$
$K^{\pm}_{D}$ DLL$_K$	> -5
Background suppressing cuts	
D-meson flight-distance significance	> 0.5
K^0_S-meson flight-distance χ^2	> 49 (LL only)

DK^{*0} candidates. The variables used in the BDT are listed in Table. 6.2; any variables related to the bachelor particle are applied to the kaon from the decay of the K^{*0} meson. The BDT is trained on the $B^+ \to D(K^0_S\pi^+\pi^+)\pi^+$ channel, with a separate BDT trained in the LL and DD track categories, and is applied to both the $D \to K^0_S\pi^+\pi^-$ and $D \to K^0_S K^+ K^-$ modes. The signal training sample consists of simulated events, and the background sample consists of candidates from the upper B^+-meson invariant-mass sideband ($m(B^+) > 5800\,{\rm MeV}/c^2$) in data.

The BDT response is calculated for each $B^0 \to DK^{*0}$ candidate, and candidates with a response below a chosen threshold are rejected. To choose this threshold, the statistical uncertainty of γ is estimated for a range of BDT requirements using the following method:

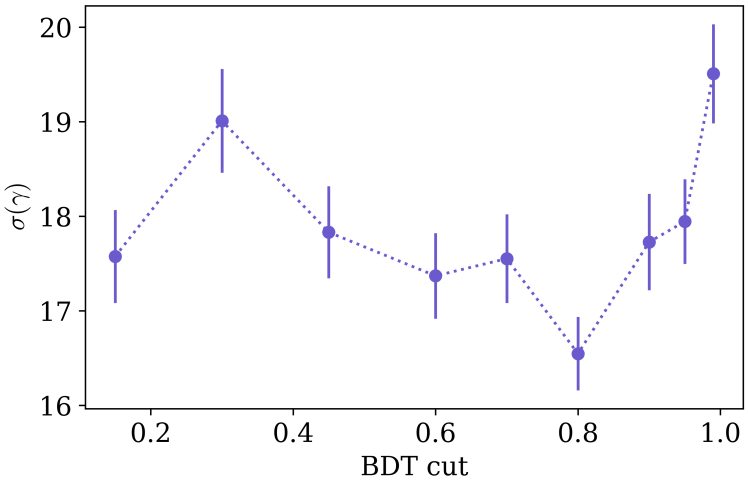

Figure 6.5: Predicted statistical uncertainty of γ at various BDT cuts, calculated from the mean uncertainty of 1800 pseudoexperiments.

1. Perform a global invariant-mass fit to selected candidates with a range of BDT requirements using the model outlined in Sect. 6.3.

2. Generate pseudoexperiments using the outputs of these fits (the setup of pseudoexperiments is described further in Sect. 7.1.2) and perform binned fits to measure $x_\pm$ and $y_\pm$.

3. Use the $x_\pm$ and $y_\pm$ values and statistical uncertainties from each pseudoexperiment to obtain γ and its uncertainty, $\sigma(\gamma)$ (the process for determining γ is described in Chap. 8). For each BDT requirement, calculate the mean value of $\sigma(\gamma)$ from all pseudoexperiments.

The mean value of $\sigma(\gamma)$ for each BDT requirement is shown in Fig. 6.5. A threshold of 0.8 is chosen, which minimises the predicted uncertainty.

Table 6.2: Variables used in a boosted decision tree trained to select $B^+ \to Dh^+$ decays. When applied to $B^0 \to DK^{*0}$ decays, the B^0 meson is used in place of the B^+ meson, and the kaon from the K^{*0}-meson decay is used in place of the bachelor particle.

Variable	Description
log10(1-Ks_DIRA_BPV)	Direction angle of K^0_S meson
log(Bu_RHO_BPV)	Radial distance from B-meson vertex to beam line
log(Bach_PT)	p_T of bachelor particle
log10(1-D0_DIRA_BPV)	Direction angle of D meson
log10(1-Bu_DIRA_BPV)	Direction angle of B meson
log(D0_RHO_BPV)	Radial distance from D-meson vertex to beam line
Bu_PTASY_1.5	p_T asymmetry of B meson
log(D0_PT)	p_T of D meson
log(Bu_constD0KSPV_CHI2NDOF)	χ^2/ degrees-of-freedom of DecayTreeFitter refit
log(Bu_FDCHI2_OWNPV)	Flight-distance χ^2 of B meson
log(max_Ksh1h2_IPCHI2_OWNPV)	Largest χ^2_{IP} of K^0_S-meson products
log(min_Ksh1h2_IPCHI2_OWNPV)	Smallest χ^2_{IP} of K^0_S-meson products
log(D0_IPCHI2_OWNPV)	χ^2_{IP} of D meson
log(Bu_P)	p of B meson
log(Bu_IPCHI2_OWNPV)	χ^2_{IP} of B meson
Bu_MAXDOCA	Distance-of-closest-approach of B-meson products
log(Bach_IPCHI2_OWNPV)	χ^2_{IP} of bachelor particle
log(Bu_PT)	p_T of B meson
log(max_h1h2_IPCHI2_OWNPV)	Largest χ^2_{IP} of D-meson products
log(min_h1h2_IPCHI2_OWNPV)	Smallest χ^2_{IP} of D-meson products
log(Ks_VTXCHI2DOF)	Vertex-fit χ^2/ degrees-of-freedom of K^0_S meson
D0_MAXDOCA	Distance-of-closest-approach of D-meson products
log(D0_VTXCHI2DOF)	Vertex-fit χ^2/ degrees-of-freedom of D meson
log(D0_P)	p of D meson
log(Bach_P)	p of bachelor particle
log(Bu_VTXCHI2DOF)	Vertex-fit χ^2/ degrees-of-freedom of B meson

6.2.3 Dalitz plots of selected candidates

Dalitz plots of selected candidates within 30 MeV/c^2 of the nominal B^0-meson mass are shown in Fig. 6.6. The candidates are separated into B^0 and $\overline{B}^0$ mesons using the charge of the kaon from the decay of the K^{*0} meson.

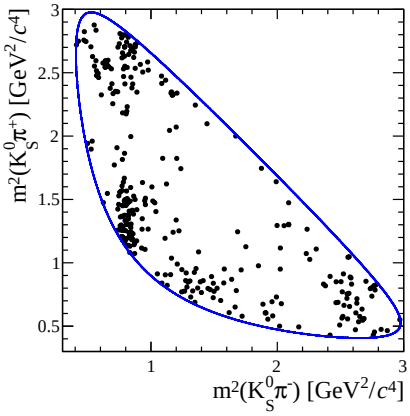

(a) $\overline{B}^0 \to D(K^0_S\pi^+\pi^-)K^{*0}$

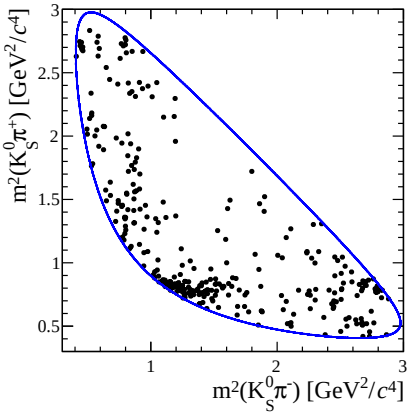

(a) $B^0 \to D(K^0_S\pi^+\pi^-)K^{*0}$

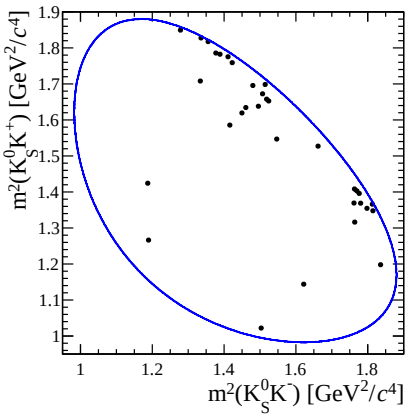

(c) $\overline{B}^0 \to D(K^0_S K^+K^-)K^{*0}$

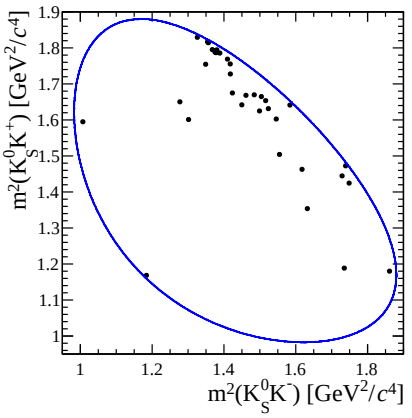

(d) $B^0 \to D(K^0_S K^+K^-)K^{*0}$

Figure 6.6: Dalitz plots of selected candidates in the signal region: (a) $\overline{B}^0 \to D(K^0_S\pi^+\pi^-)\overline{K}^{*0}$ decays, (b) $B^0 \to D(K^0_S\pi^+\pi^-)K^{*0}$ decays, (c) $\overline{B}^0 \to D(K^0_S K^+K^-)\overline{K}^{*0}$ decays, and (d) $B^0 \to D(K^0_S K^+K^-)K^{*0}$ decays. The kinematic boundary is shown in blue.

6.3 Global invariant-mass fit

Before the *CP* observables are determined from a simultaneous invariant-mass fit in each Dalitz bin and B-meson-flavour category, a global fit is performed so that some fit parameters can be fixed in the later fits on the subsamples. The data in the global fit are split by D-meson decay ($K^0_S\pi^+\pi^-$ and $K^0_S K^+ K^-$) and K^0_S-meson-track type (LL and DD). Many fit parameters are shared between the categories. The PDFs used in the fit are based on those developed for the ADS/GLW analysis in Chap. 4.

The invariant-mass range used in the fit is 5200–5800 MeV/c^2. The limited range with respect to the ADS/GLW analysis, which uses the range 5000–5800 MeV/c^2, significantly reduces the yield of the partially reconstructed $B^0 \to D^* K^{*0}$ background; this is desirable because the *CP*-violation parameters of this background, and hence its distribution across the Dalitz plot, are unknown. The partially reconstructed $B^+ \to DK^+\pi^-\pi^+$ background is reduced to a negligible level and can be ignored.

The invariant-mass model contains the following components:

1. Signal $B^0 \to DK^{*0}$ and $\overline{B}^0_s \to DK^{*0}$ decays;
2. Combinatorial background;
3. Partially reconstructed $B^0 \to D^* K^{*0}$ and $\overline{B}^0_s \to D^* K^{*0}$ decays;
4. Misidentified $B^0 \to D\pi^+\pi^-$ decays;
5. Background from $B^+ \to DK^+$ decays combined with a random pion.

The final component is not included in the ADS/GLW model, as $B^+ \to DK^+$ decays are removed from the ADS/GLW samples with a veto. Previous analyses of the GGSZ modes found that such a veto sculpts the distribution of the combinatorial background in an undesirable way, so it is better to fit this background than to remove it.

Table 6.3: Relative fractions of each component of the partially reconstructed $B^0 \to D^* K^{*0}$ and $\overline{B}{}^0_s \to D^* K^{*0}$ backgrounds in the invariant-mass range 5200–5800 MeV/c^2.

Parameter	$B^0 \to DK^{*0}$	$\overline{B}{}^0_s \to DK^{*0}$
α_{010}	0.903 ± 0.013	0.729 ± 0.024
g_{010}	0.865 ± 0.008	0.523 ± 0.009
g_{101}	0.9837 ± 0.0021	0.843 ± 0.005

6.3.1 Invariant-mass fit setup

The PDFs described in Sect. 4.2 are used for all components of the fit model except the $B^+ \to DK^+$ background. The mean of the $\overline{B}{}^0_s \to DK^{*0}$ peak is a free parameter, with respect to which the B^0-meson signal mean is fixed using the known B^0_s–B^0 meson mass difference of 87.26 MeV/c^2 [71]. The widths of the signal peaks are shared for B^0_s and B^0 mesons, but are allowed to be different for different K^0_S-meson-track types to account for the better precision of LL tracks.

Partially reconstructed background shape

Partially reconstructed $B^0 \to D^* K^{*0}$ and $\overline{B}{}^0_s \to D^* K^{*0}$ decays are modelled with the superposition of Horns, Hill and LittleHorns PDFs given in Eq. 4.13. In the ADS/GLW invariant-mass fit, the relative fractions of $D^* \to D^0\gamma$ decays in each helicity state, g_{010} and g_{101}, are fixed, while the helicity fraction, α_{010}, is a free parameter. As the four contributing decays have different invariant-mass shapes, their relative yields in the GGSZ fit are affected by the limited invariant-mass range. The values of g_{010}, g_{101}, and α_{010} in this range are calculated from the ADS/GLW values using the ratios of the integrals of each shape in the two mass ranges. The calculated values, given in Table 6.3, are fixed in the GGSZ invariant-mass fit.

Modelling of $B^+ \to DK^+$ decays

The background from $B^+ \to DK^+$ decays combined with a random pion from elsewhere in the event is modelled with a Crystal Ball function used in the study in Ref. [51]. The projection of a fit to simulated events is shown in Fig. 6.7.

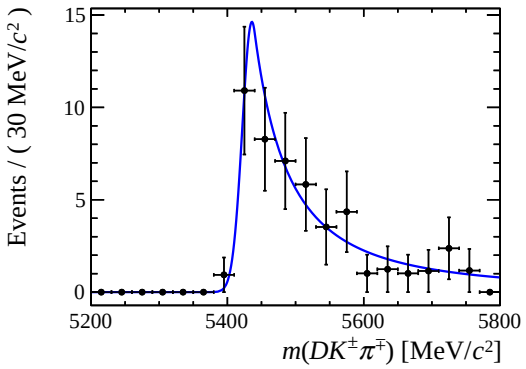

Figure 6.7: A fit to simulated $B^+ \to DK^+$ decays reconstructed as $B^0 \to DK^{*0}$ decays using a Crystal Ball function, reproduced from Ref. [39].

Fixed background yields

As the GGSZ data samples contain significantly fewer candidates than the ADS/GLW samples, it is beneficial to fix the relative yields of the peaking physics backgrounds using the results of the ADS/GLW fit in Sect. 4.3. These values are adjusted to account for the limited invariant-mass range. The relative yield of the $B^+ \to DK^+$ background is taken from Ref. [39].

The yields of the $B^0 \to D^*K^{*0}$, $\overline{B}{}^0_s \to D^*K^{*0}$, $B^0 \to D\pi^+\pi^-$ and $B^+ \to DK^+$ backgrounds are fixed with respect to the yield of $\overline{B}{}^0_s \to DK^{*0}$ decays via the ratios $R_{\rm low}$, $R_{s,\rm low}$, $R_{D\pi\pi}$ and R_{DK}, respectively, where

$$\begin{aligned} R_{\rm low} &= 0.014 \pm 0.001, \\ R_{s,\rm low} &= 0.219 \pm 0.005, \\ R_{D\pi\pi} &= 0.016 \pm 0.004, \\ R_{DK} &= 0.043 \pm 0.010. \end{aligned}$$

6.3.2 Results of global invariant-mass fit

The invariant-mass distributions and fitted PDFs are shown in Figs. 6.8 and 6.9. The results for the free parameters are given in Table 6.4. The distributions are similar to those of the GLW modes in Sect. 4.3, containing clear peaks from both B^0-meson and B^0_s-meson decays. The low combinatorial-background levels indicate that the BDT from the $B^+ \to Dh^+$ analysis performs very well for $B^0 \to DK^{*0}$ decays.

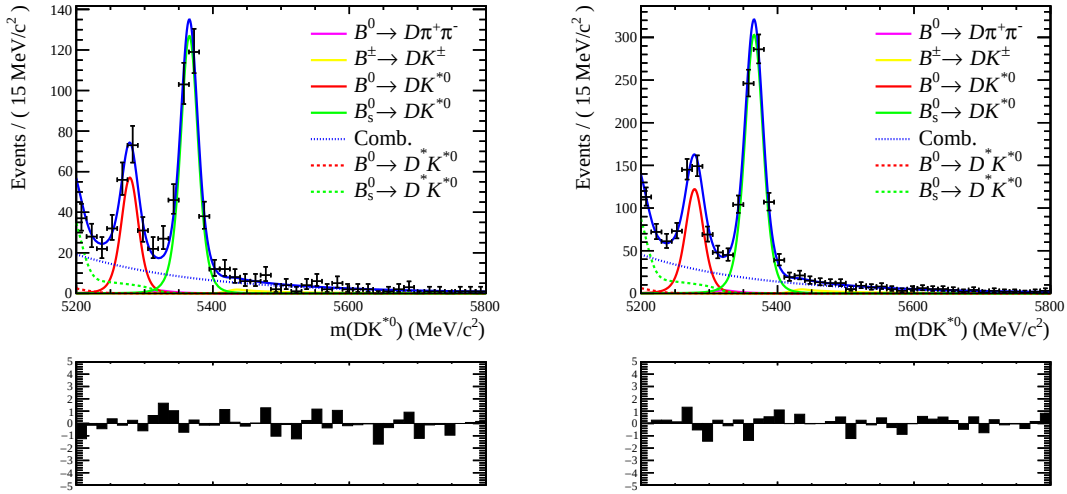

(a) LL tracks (b) DD tracks

Figure 6.8: Invariant-mass distributions (data points with error bars) and fit results (solid blue line) for $B^0 \to DK^{*0}$ and $\overline{B}^0 \to D\overline{K}^{*0}$ decays with $D \to K^0_S\pi^+\pi^-$, in (a) the LL category and (b) the DD category. Different components of the fit are shown with coloured lines according to the legend. The residuals are shown below.

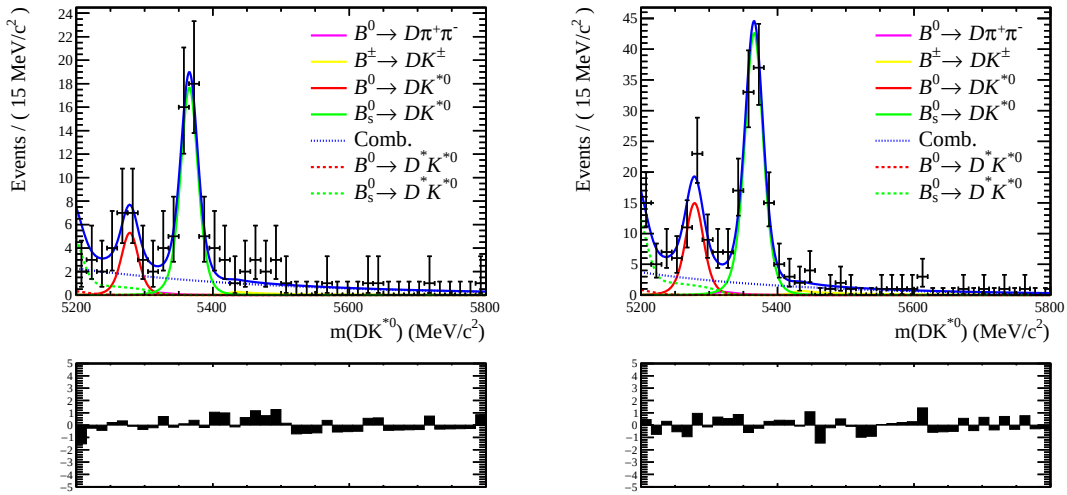

(a) LL tracks (b) DD tracks

Figure 6.9: Invariant-mass distributions (data points with error bars) and fit results (solid blue line) for $B^0 \to DK^{*0}$ and $\overline{B}^0 \to D\overline{K}^{*0}$ decays with $D \to K^0_S K^+K^-$, in (a) the LL category and (b) the DD category. Different components of the fit are shown with coloured lines according to the legend. The residuals are shown below.

Table 6.4: Values obtained for the free parameters in a fit to the invariant-mass distributions of selected data candidates summed over B-meson flavour and D-meson Dalitz bin.

Parameter	Description	Value
Signal $B^0 \to DK^{*0}$ decays		
σ_{LL}	Left-hand width of Cruijff in LL category in MeV/c^2	12.2 ± 0.9
σ_{DD}	Left-hand width of Cruijff in DD category in MeV/c^2	12.8 ± 0.5
$N(K^0_{\mathrm{S}}\pi^+\pi^-,\ \mathrm{LL})$	Yield of $D \to K^0_{\mathrm{S}}\pi^+\pi^-$ in LL category	130 ± 17
$N(K^0_{\mathrm{S}}\pi^+\pi^-,\ \mathrm{DD})$	Yield of $D \to K^0_{\mathrm{S}}\pi^+\pi^-$ in DD category	293 ± 26
$N(K^0_{\mathrm{S}}K^+K^-,\ \mathrm{LL})$	Yield of $D \to K^0_{\mathrm{S}}K^+K^-$ in LL category	12 ± 5
$N(K^0_{\mathrm{S}}K^+K^-,\ \mathrm{DD})$	Yield of $D \to K^0_{\mathrm{S}}K^+K^-$ in DD category	36 ± 8
$\overline{B}^0_s \to DK^{*0}$ decays		
μ_s	Mean of Cruijff in MeV/c^2	5365.6 ± 0.5
$N_s(K^0_{\mathrm{S}}\pi^+\pi^-,\ \mathrm{LL})$	Yield of $D \to K^0_{\mathrm{S}}\pi^+\pi^-$ in LL category	290 ± 21
$N_s(K^0_{\mathrm{S}}\pi^+\pi^-,\ \mathrm{DD})$	Yield of $D \to K^0_{\mathrm{S}}\pi^+\pi^-$ in DD category	730 ± 33
$N_s(K^0_{\mathrm{S}}K^+K^-,\ \mathrm{LL})$	Yield of $D \to K^0_{\mathrm{S}}K^+K^-$ in LL category	40 ± 7
$N_s(K^0_{\mathrm{S}}K^+K^-,\ \mathrm{DD})$	Yield of $D \to K^0_{\mathrm{S}}K^+K^-$ in DD category	103 ± 12
Combinatorial background		
$N_{\mathrm{comb}}(K^0_{\mathrm{S}}\pi^+\pi^-,\ \mathrm{LL})$	Yield of $D \to K^0_{\mathrm{S}}\pi^+\pi^-$ in LL category	224 ± 32
$N_{\mathrm{comb}}(K^0_{\mathrm{S}}\pi^+\pi^-,\ \mathrm{DD})$	Yield of $D \to K^0_{\mathrm{S}}\pi^+\pi^-$ in DD category	494 ± 47
$N_{\mathrm{comb}}(K^0_{\mathrm{S}}K^+K^-,\ \mathrm{LL})$	Yield of $D \to K^0_{\mathrm{S}}K^+K^-$ in LL category	38 ± 10
$N_{\mathrm{comb}}(K^0_{\mathrm{S}}K^+K^-,\ \mathrm{DD})$	Yield of $D \to K^0_{\mathrm{S}}K^+K^-$ in DD category	52 ± 15

Chapter 7

Measurement of *CP* observables in $B^0 \to DK^{*0}$ decays with three-body D-meson final states

This chapter presents a simultaneous fit to selected $B^0 \to D(K^0_S h^+ h^-)K^{*0}$ decays in bins of the D-meson Dalitz plane, from which the CP observables $x_\pm$ and $y_\pm$ are determined. The $D \to K^0_S \pi^+ \pi^-$ and $D \to K^0_S \pi^+ \pi^-$ data samples contain approximately 423 and 48 signal candidates, respectively, with around two-thirds of the K^0_S-meson candidates reconstructed from two downstream pion tracks (DD) and one-third reconstructed from long pion tracks (LL). The observables are corrected for small biases in the fit, and systematic uncertainties are assigned.

7.1 Binned Dalitz plot invariant-mass fit

7.1.1 Configuration of the binned fit

The PDFs used for each signal and background component in the binned fit are the same as those used in the global invariant-mass fit discussed in Sect. 6.3, with all means and widths fixed to the values found in the global fit. We assume that there is no significant variation in shapes between Dalitz bins with the current small sample size.

Signal and background yields

The total signal yield is a free parameter in each of the eight D-meson-decay, K^0_S-meson-track-type, and B-meson-flavour categories. The signal yield in each bin of the Dalitz plot is calculated using Eqs. 6.2 and 6.3, where the *CP* observables $x_\pm$ and $y_\pm$ are free parameters shared between all bins.

The total yield of $\overline{B}^0_s \to DK^{*0}$ decays is also a free parameter in each mode, track, and flavour category. The interference in these decays is negligible, as the decay $B^0_s \to D^0\overline{K}^{*0}$ requires very suppressed quark flavour transitions. We therefore assume that B^0_s mesons decay only to $\overline{D}^0$ mesons, and $\overline{B}^0_s$ mesons decay only to D^0 mesons. As the B^0-meson category contains the decays of $\overline{B}^0_s$ mesons, and vice versa, the B^0_s-meson yield in bin i of the B^0-meson category is calculated by multiplying the total yield by F_i, while the yield in bin i of the $\overline{B}^0$-meson category is calculated using F_{-i}.

The total yields of the backgrounds from $B^0 \to D^*K^{*0}$, $\overline{B}^0_s \to D^*K^{*0}$, $B^0 \to D\pi^+\pi^-$, and $B^+ \to DK^+$ decays are determined by multiplying the total $\overline{B}^0_s \to DK^{*0}$ yields by the fractions R_{low}, $R_{s,\text{low}}$, R_{misID}, and R_{DK}, respectively. The values of these fractions are given in Sect. 6.3.1.

The yields of partially reconstructed $\overline{B}^0_s \to D^*K^{*0}$ decays in each bin are calculated in the same way as the yields of fully reconstructed $\overline{B}^0_s \to DK^{*0}$ decays, as they are also expected to contain negligible interference. The amount of interference in partially reconstructed $B^0 \to D^*K^{*0}$ decays is unknown, but can be ignored as the yield of this background is very small; the yields of this background in bin i of the B^0 and $\overline{B}^0$ categories are therefore calculated by multiplying the total yields by F_{-i} and F_i, respectively. This assumption leads to a small systematic uncertainty.

In misidentified $B^0 \to D\pi^+\pi^-$ decays, the D meson is assumed to be an equal mixture of D^0 and $\overline{D}^0$ states. The yields in bins i and $-i$ are therefore both calculated from the total yield multiplied by $(F_i + F_{-i})/2$. The interference parameters for $B^+ \to DK^+$ decays are well measured, so the binned yields of this background are

calculated using Eqs. 6.2 and 6.3 with values for $x_\pm$, $y_\pm$ calculated using values of γ, r_{B^+}, and δ_{B^+} from the most recent LHCb combination [24].

The Dalitz plot distribution of the combinatorial background is unknown and may not be uniform, so its yield in each bin is a free parameter in the fit. In some bins, the combinatorial background is negligible; these bins are identified in an auxiliary fit, and their yields are fixed to zero in the final fit, which allows the covariance matrix of the fit results to be calculated correctly.

External inputs

The yields of the decays of B^0 and $\overline{B}^0$ mesons in each bin depend on the strong-phase parameters c_i and s_i, the D-meson-decay fractions F_i, and the K^{*0} coherence factor κ. These parameters are fixed from external inputs in order to increase the precision of the measured CP observables.

The strong-phase parameters are taken from measurements by the CLEO and BESIII experiments [42,43], given in Table 7.1. The F_i values are measured separately for each K^0_S-meson-track type in an analysis of $B^+ \to Dh^+$ decays [79] and are given in Tables 7.2 and 7.3. The coherence factor is determined in an amplitude analysis of $B^0 \to DK^+\pi^-$ decays to be $\kappa = 0.958\,^{+0.005}_{-0.046}$ for the K^{*0}-meson selection criteria used in this measurement [45].

Table 7.1: Values of the strong-phase inputs. The values for $D \to K^0_S\pi^+\pi^-$ decays are taken from a combination of measurements by the BESIII and CLEO experiments [43], and the values for $D \to K^0_S K^+ K^-$ decays are taken from the CLEO measurement [42].

$D \to K^0_S\pi^+\pi^-$ (optimal binning)			$D \to K^0_S K^+ K^-$ (2 bins)		
i	c_i	s_i	i	c_i	s_i
1	-0.04 ± 0.05	0.83 ± 0.10	1	0.82 ± 0.11	-0.45 ± 0.26
2	0.84 ± 0.07	0.29 ± 0.15	2	-0.75 ± 0.09	-0.23 ± 0.23
3	0.15 ± 0.07	0.79 ± 0.15		-	
4	-0.91 ± 0.02	0.08 ± 0.06		-	
5	-0.29 ± 0.04	-1.02 ± 0.06		-	
6	0.27 ± 0.08	-0.98 ± 0.18		-	
7	0.92 ± 0.02	-0.18 ± 0.07		-	
8	0.77 ± 0.03	0.28 ± 0.12		-	

Table 7.2: Values of F_i in the LL tracks category, taken from a study of $B^+ \to Dh^+$ decays [79].

$D \to K^0_S\pi^+\pi^-$ (optimal binning)		$D \to K^0_S K^+ K^-$ (2 bins)	
i	F_i	i	F_i
1	0.0204 ± 0.0005	1	0.2650 ± 0.0045
2	0.0040 ± 0.0003	2	0.2946 ± 0.0046
3	0.0035 ± 0.0002	-1	0.2399 ± 0.0043
4	0.0567 ± 0.0009	-2	0.2005 ± 0.0040
5	0.0279 ± 0.0006		-
6	0.0042 ± 0.0003		-
7	0.0543 ± 0.0009		-
8	0.0679 ± 0.0009		-
-1	0.0939 ± 0.0011		-
-8	0.0251 ± 0.0006		-
-7	0.1280 ± 0.0013		-
-6	0.0615 ± 0.0009		-
-5	0.0480 ± 0.0008		-
-4	0.0974 ± 0.0011		-
-3	0.1597 ± 0.0014		-
-2	0.1474 ± 0.0013		-

Table 7.3: Values of F_i in the DD tracks category, taken from a study of $B^+ \to Dh^+$ decays [79].

$D \to K^0_S\pi^+\pi^-$ (optimal binning)		$D \to K^0_S K^+ K^-$ (2 bins)	
i	F_i	i	F_i
1	0.0211 ± 0.0004	1	0.2880 ± 0.0031
2	0.0048 ± 0.0002	2	0.2706 ± 0.0030
3	0.0041 ± 0.0002	-1	0.2366 ± 0.0029
4	0.0600 ± 0.0006	-2	0.2048 ± 0.0027
5	0.0249 ± 0.0004		-
6	0.0036 ± 0.0002		-
7	0.0574 ± 0.0006		-
8	0.0704 ± 0.0006		-
-1	0.0955 ± 0.0007		-
-8	0.0234 ± 0.0004		-
-7	0.1272 ± 0.0008		-
-6	0.0626 ± 0.0006		-
-5	0.0422 ± 0.0005		-
-4	0.1017 ± 0.0008		-
-3	0.1520 ± 0.0009		-
-2	0.1493 ± 0.0009		-

7.1.2 Fit results and bias correction

The invariant-mass distributions and fit projections in each bin of the Dalitz plot are shown in Figs. 7.1–7.4. The central values and statistical uncertainties of the *CP* observables determined from the fit are

$$\begin{aligned} x_+ &= 0.045 \pm 0.076, \\ x_- &= -0.248 \pm 0.083, \\ y_+ &= -0.156 \pm 0.106, \\ y_- &= 0.184 \pm 0.098. \end{aligned}$$

A fit to the physics parameters of interest using the method described in Chap. 8 returns the central values $\gamma = 68^\circ$, $r_{B^0} = 0.25$, and $\delta_{B^0} = 213^\circ$.

As the yields in each bin are very low, small biases are seen in fits to pseudoexperiments. The pseudoexperiments are generated using the binned-fit model with the following fixed parameters:

- Global yields and shape parameters are fixed to the values found in the global invariant-mass fit;

- Signal yields in each bin are calculated using Eqs. 6.2 and 6.3 with $x_\pm$ and $y_\pm$ fixed. The values of $x_\pm$ and $y_\pm$ are calculated from the values of γ, r_{B^0}, and δ_{B^0} corresponding to the raw measured observables listed above;

- The combinatorial background is assumed to be distributed uniformly across the Dalitz plane;[1]

- All other binned background yields are calculated from the total yields as described in Sect. 7.1.1.

Each pseudoexperiment is fitted using the default binned-fit model to obtain values of $x_\pm$ and $y_\pm$. The pull of each observable is calculated as defined in Eq. 5.7. Figure 7.5 shows the distributions of the central values, statistical uncertainties, and pulls for each observable in 10 000 pseudoexperiments. The means of the pull distributions differ from zero, which means that there are small differences between the measured values in data and the mean values from the pseudoexperiments. The observables are corrected for this bias according to

$$x_{\text{corr}} = x_{\text{meas}} - \mu_{\text{pull}} \times \sigma_{\text{meas}}, \tag{7.1}$$

where x_{corr} is the corrected observable, μ_{pull} is the mean of the pull distribution, and x_{meas} and σ_{meas} are the central value and statistical uncertainty, respectively, of the observable measured in the fit to real data. The biases $\mu_{\text{pull}} \times \sigma_{\text{meas}}$ are found to be -0.0015, 0.0017, 0.0048, and -0.0033 for x_+, x_-, y_+, and y_-, respectively; these values are small compared with the statistical uncertainties.

The widths of the pull distributions are found to be 1.008 ± 0.009, 1.011 ± 0.009, 1.075 ± 0.010, and 1.066 ± 0.010 for x_+, x_-, y_+, and y_-, respectively. The widths are greater than one, which means that the standard deviations of the central values in pseudoexperiments are larger than the measured statistical uncertainties. This is

[1] In practice this may not be the case, as the combinatorial background can contain true D^0 or $\overline{D}^0$ mesons; however, studies with different combinatorial background configurations show that it has little effect on the measurements of the fitter bias.

corrected for by multiplying each raw statistical uncertainty by the corresponding pull width.

After these corrections are applied, the central values and statistical uncertainties of the *CP* observables are

$$\begin{aligned} x_+ &= 0.046 \pm 0.077, \\ x_- &= -0.249 \pm 0.084, \\ y_+ &= -0.160 \pm 0.114, \\ y_- &= 0.188 \pm 0.105. \end{aligned}$$

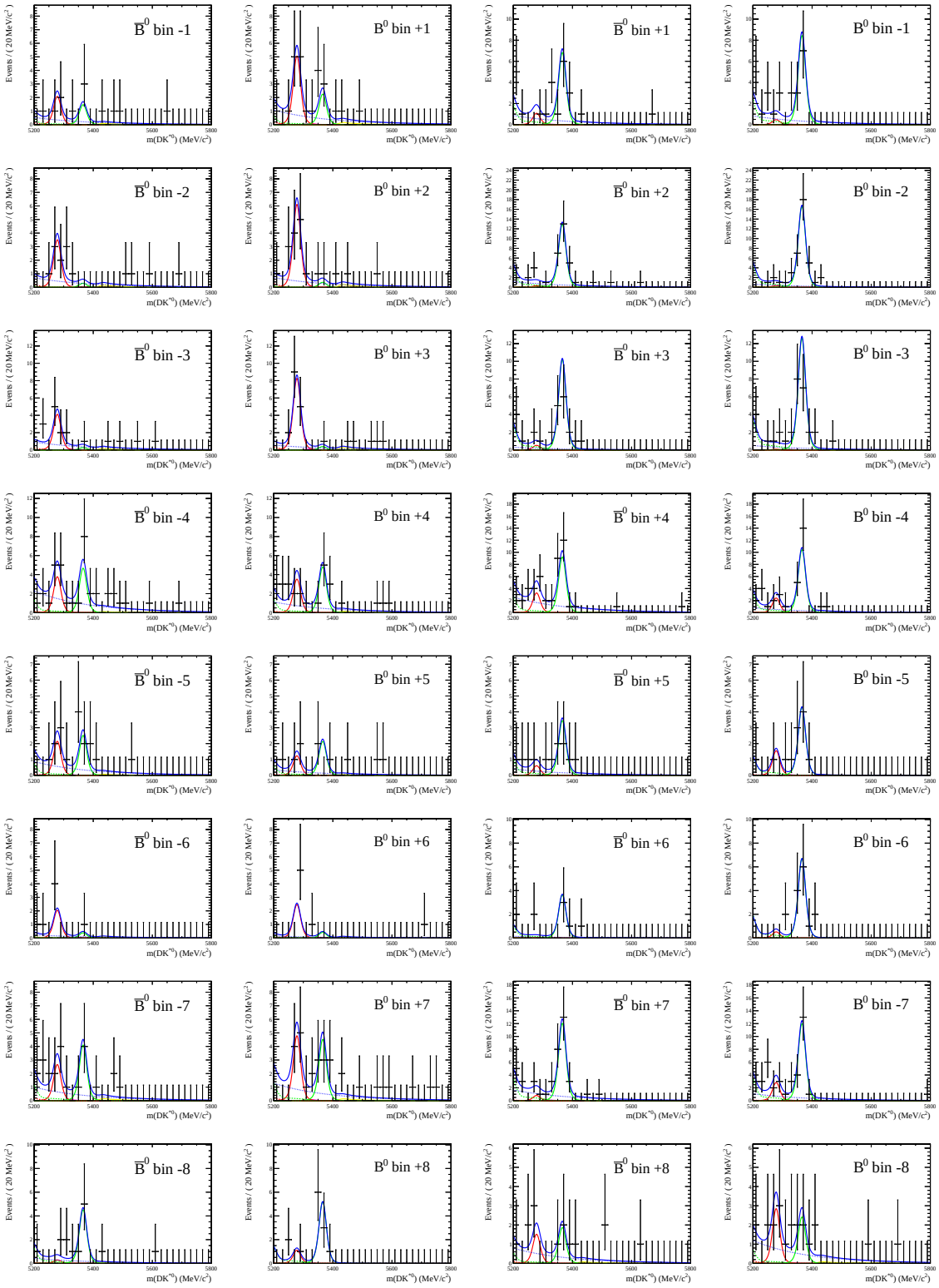

Figure 7.1: Fit projections for $B^0 \to D(K^0_S\pi^+\pi^-)K^{*0}$ decays in each bin of the D-meson Dalitz plane, with the K^0_S meson reconstructed from long tracks.

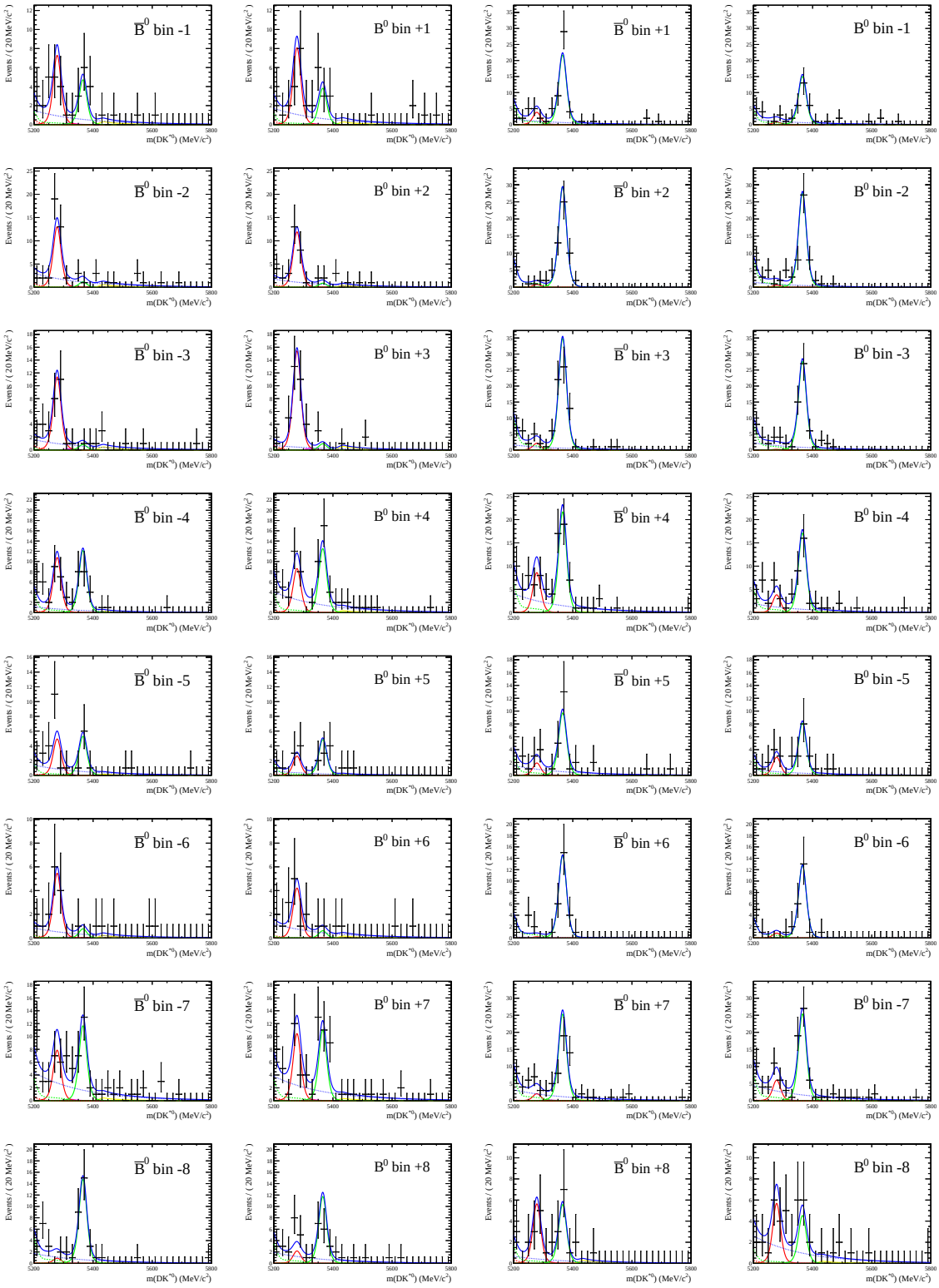

Figure 7.2: Fit projections for $B^0 \to D(K^0_S\pi^+\pi^-)K^{*0}$ decays in each bin of the D-meson Dalitz plane, with the K^0_S meson reconstructed from downstream tracks.

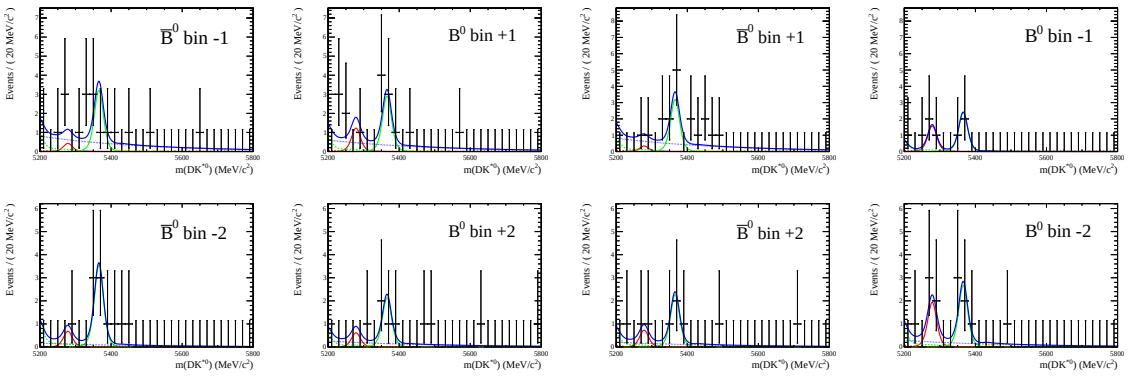

Figure 7.3: Fit projections for $B^0 \to D(K^0_S K^+ K^-)K^{*0}$ decays in each bin of the D-meson Dalitz plane, with the K^0_S meson reconstructed from long tracks.

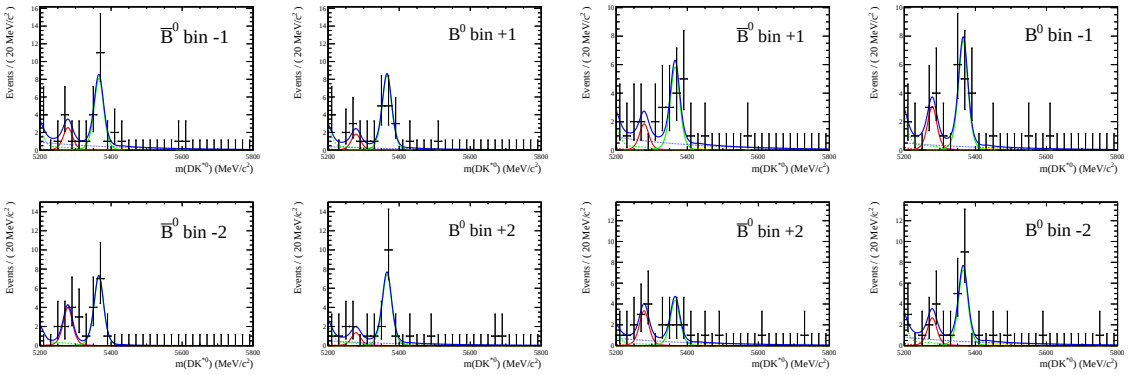

Figure 7.4: Fit projections for $B^0 \to D(K^0_S K^+ K^-)K^{*0}$ decays in each bin of the D-meson Dalitz plane, with the K^0_S meson reconstructed from downstream tracks.

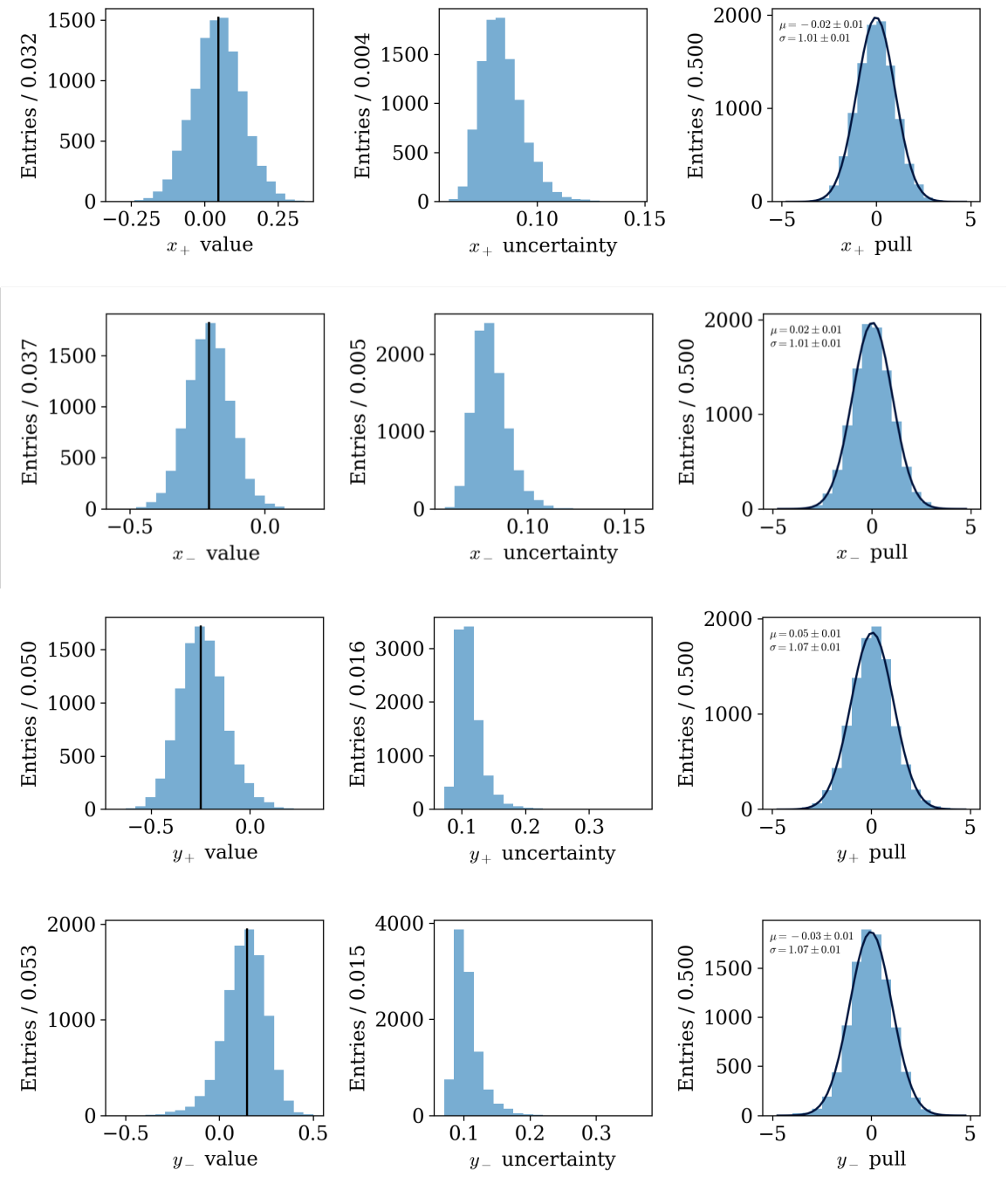

Figure 7.5: Distributions of (left) central values, (centre) statistical uncertainties, and (right) pulls of the *CP* observables in 10 000 pseudoexperiments. The central values from the fit to data are indicated by black lines. Each pull distribution is fitted with a Gaussian function of mean μ and width σ.

7.2 Systematic uncertainties

The *CP* observables are assigned systematic uncertainties to account for various assumptions and uncertainties in the fit. Each uncertainty is evaluated either through the data-driven method discussed in Sect. 5.3, or by comparing the observables in ensembles of pseudoexperiments generated with different assumptions.

Strong-phase inputs

A systematic uncertainty is assigned to account for the uncertainties on the measurements of the strong-phase parameters c_i and s_i, given in Table 7.1. The data are fitted 1000 times with the central values of these parameters smeared. The standard deviations of the observables in these fits are taken to be the systematic uncertainties.

The strong-phase-related uncertainties are found to be 0.005, 0.006, 0.031, and 0.017 for x_+, x_-, y_+, and y_-, respectively. This is the dominant source of systematic uncertainty for y_+ and y_-; for x_+ and x_-, it is of a similar size to the total systematic uncertainty from all other sources.

Input of F_i values from $B^+ \to D\pi^+$ measurement

The uncertainties on the F_i values in Tables 7.2 and 7.3 are very small, so their effects are negligible when propagated to the observables. However, a systematic uncertainty is assigned to account for small differences in the efficiency profiles of $B^+ \to D\pi^+$ and $B^0 \to DK^{*0}$ decays.

In the one-dimensional efficiency comparisons in Fig. 6.3, small discrepancies are seen in the distributions of $m^2_{\pi\pi} \equiv m^2(\pi^+, \pi^-)$. The ratios between the two distributions are fitted with straight lines, which would have gradients of zero and intercepts of one if the samples were in perfect agreement. Some of the fitted straight-line parameters are found to deviate from this by more than one standard deviation. These parameters are used to estimate the relationship between the $B^+ \to D\pi^+$ efficiency

profile $\eta_{D\pi^+}$ and the $B^0 \to DK^{*0}$ efficiency profile $\eta_{DK^{*0}}$ as a function of $m^2_{\pi\pi}$:

$$\eta_{DK^{*0}} = f(m^2_{\pi\pi})\eta_{D\pi} = (a + bm^2_{\pi\pi})\eta_{D\pi}, \tag{7.2}$$

where a and b are the intercept and gradient, respectively. The function $f(m^2_{\pi\pi})$ is used to calculate a weighting factor R_i for each bin. This involves a sum over the pixels, p, in the 500×500 pixel map used to define the binning scheme. The weighting factors are calculated from

$$R_i = \frac{\sum_p \mathcal{A}^2(p)\eta_{D\pi}(p)f(m^2_{\pi\pi}(p))}{\sum_p \mathcal{A}^2(p)\eta_{D\pi}(p)} \tag{7.3}$$

where the sum is performed over each pixel inside bin i; the efficiency $\eta_{D\pi}(p)$ is the fraction of simulated $B^+ \to D\pi^+$ events in pixel p; the amplitude squared $\mathcal{A}^2(p)$ is taken from a model developed by BaBar and Belle [40]; and $m^2_{\pi\pi}(p)$ is calculated from the values of m^2_+ and m^2_- at the centre of each pixel.

An alternative set of F_i values is calculated by multiplying each value in Tables 7.2 and 7.3 by R_i and normalizing the new values F'_i such that $\sum_i F'_i = 1$. Figure 7.6 compares the original and adjusted F_i values. An ensemble of 10 000 pseudoexperiments is generated using the adjusted values and fitted with the default model. The mean value of each observable in this ensemble is compared with the mean value in pseudoexperiments with the default setup, and the difference is taken to be the systematic uncertainty.

This study finds uncertainties of 0.008, 0.007, 0.002 and 0.001 for x_+, x_-, y_+ and y_-, respectively. This is the largest source of systematic uncertainty for x_+ and x_-, but is still an order of magnitude smaller than the statistical uncertainty. For y_+ and y_-, these uncertainties are very small compared with the statistical and strong-phase-related uncertainties. The uncertainties are smaller than those associated with the use of F_i values measured with the semileptonic control channel in Ref. [51], which indicates that using F_i values measured with $B^+ \to Dh^+$ decays is a favourable strategy.

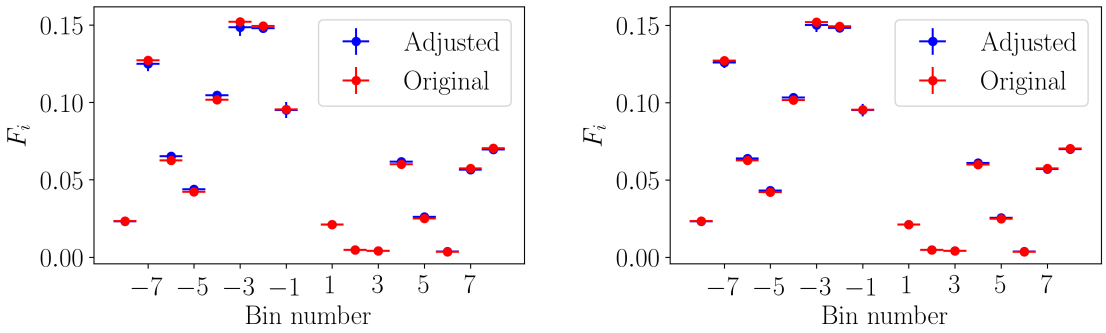

(a) LL tracks (b) DD tracks

Figure 7.6: Original F_i values (red) compared with values adjusted to account for small differences between the efficiency profiles of simulated $B^+ \to D\pi^+$ and $B^0 \to DK^{*0}$ decays (blue), for (a) LL tracks and (b) DD tracks.

Fit-related systematics

The invariant-mass fit contains several fixed parameters related to the background components. The relative contributions of each component of the partially reconstructed backgrounds are fixed via the parameters α, g_{010}, and g_{101}, and the total yield of each background relative to the $\overline{B}{}^0_s \to DK^{*0}$ yield is also fixed. The uncertainties of each of these parameters are propagated to the observables using many fits to data.

The measured observables are affected by the choice of signal shape, which is taken from a fit to simulated $B^0 \to D(K^+\pi^-)K^{*0}$ decays. Pseudoexperiments are generated with signal events distributed according to an alternative shape taken from simulated $B^0 \to D(K^0_S\pi^+\pi^-)K^{*0}$ decays and fitted with the default model. The systematic uncertainties due to the choice of signal shape are taken from the differences in the observables in these pseudoexperiments compared with the default pseudoexperiments.

A further uncertainty arises from the decision to neglect interference in partially reconstructed $B^0 \to D^*K^{*0}$ decays. The effect of this assumption is measured by comparing pseudoexperiments generated with three different *CP*-violation models for this background:

1. No *CP* violation: the yield in bin i is the total yield multiplied by F_{-i}.

2. Same amount of *CP* violation as the signal decay: the yield in bin i is calculated using Eqs. 6.2 and 6.3.

3. Maximal *CP* violation: the yield in bin i is the total yield multiplied by F_i.

Each pseudoexperiment is fitted with the default model. For each observable, the largest difference between the means of the three ensembles of pseudoexperiments is taken to be the systematic uncertainty.

Value of coherence factor

To assign a systematic uncertainty for the fixed value of $\kappa = 0.958\,^{+0.005}_{-0.046}$, pseudoexperiments are generated using $\kappa = 0.912$, which is the central value minus one standard deviation. The pseudoexperiments are fitted using the default value of κ, and the means of the observables are compared with the default pseudoexperiments to obtain the systematic uncertainties.

Charmless background

The background from charmless events is significantly reduced by removing candidates with a D-meson flight-distance significance of less than 0.5. Residual charmless events are searched for in fits to the B^0-meson invariant-mass distribution of candidates in the D-meson invariant-mass sidebands ($> 50\,\mathrm{MeV}/c^2$ from the known D-meson mass). The $K^0_S K^+ K^-$ and $K^0_S \pi^+ \pi^-$ modes can be misidentified and cross-feed into one another, so we study only the lower and upper sidebands for $K^0_S K^+ K^-$ and $K^0_S \pi^+ \pi^-$ decays, respectively. No evidence of charmless decays is seen in the $K^0_S K^+ K^-$ mode, whereas in the $K^0_S \pi^+ \pi^-$ mode an excess of 20 ± 9 events is observed at the known B^0-meson mass, as shown in Fig. 7.7. The effect of this potential charmless contamination is considered as a source of systematic uncertainty.

Some of the "charmless" events may actually be true signal events that have leaked into the sideband region. The rate of sideband leakage with respect to the selection

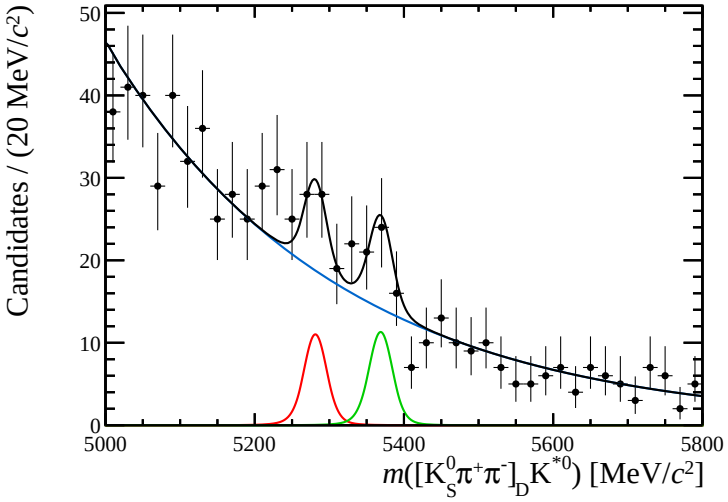

Figure 7.7: A fit to the B^0-meson invariant-mass distribution for candidates in the upper D-meson invariant-mass sideband in the $D \to K^0_S\pi^+\pi^-$ mode. The fit model includes a peak for B^0-meson decays (red), a peak for B^0_s-meson decays (green), and an exponential combinatorial background component (blue).

efficiency of the D-meson invariant-mass requirement is estimated using simulated data to be $\sim 1.3\%$. From the signal yields in Table 6.4, we expect $\mathcal{O}(6)$ signal events to leak into the sideband, which leaves $\mathcal{O}(14)$ potential charmless events.

The distribution of charmless events across the Dalitz plane is estimated from the distribution of sideband events with $m(B^0) > 5200\,\text{MeV}$. Pseudoexperiments are generated with additional charmless events added to the signal yields according to this distribution and fitted with the default model. This produces a small shift in the central values of the observables compared with default pseudoexperiments, which is assigned as a systematic uncertainty.

Bin migration

Measurements of the Dalitz coordinates (m^2_-, m^2_+) are affected by the finite momentum resolution of the detector, which can cause candidates near the bin boundaries to be assigned to the wrong bin. To first order, the use of F_i values measured in data accounts for this migration. However, as the amount of *CP* violation in $B^+ \to D\pi^+$ and $B^0 \to DK^{*0}$ decays is different, the level of bin migration can be slightly different

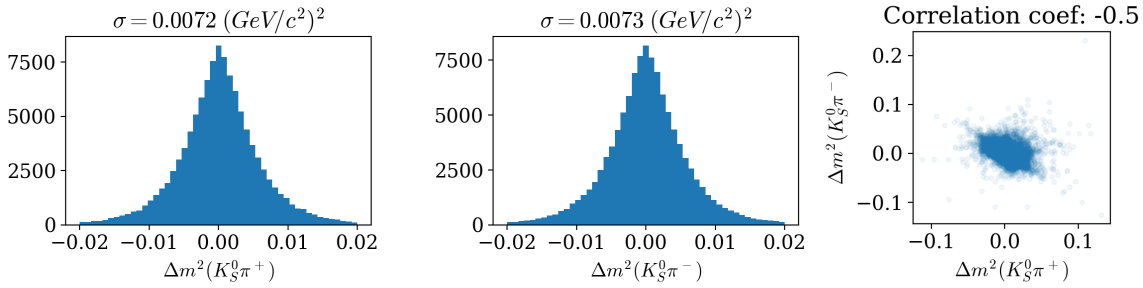

(a) Resolution (b) Correlation

Figure 7.8: (a) Distributions of $\Delta m^2 = m^2_{\text{true}} - m^2_{\text{meas}}$, where m^2_{true} is the true Dalitz coordinate and m^2_{meas} is the measured coordinate, for $m^2(K^0_S\pi^+)$ and $m^2(K^0_S\pi^-)$ in simulated $B^0 \to DK^{*0}$ decays. (b) Correlation between the distributions of $\Delta m^2(K^0_S h^+)$ and $\Delta m^2(K^0_S h^-)$.

in the two samples.

The resolutions of the Dalitz coordinates are estimated by comparing the measured coordinates with the true coordinates in simulated events. The distributions of the coordinate differences in simulated $B^0 \to DK^{*0}$ decays are shown in Fig. 7.8. The resolutions of m^2_- and m^2_+ are found to be approximately $0.007\,\text{MeV}/c^2$ in both $B^+ \to D\pi^+$ and $B^0 \to DK^{*0}$ decays. The correlation between the m^2_- and m^2_+ resolutions is -0.5 due to the mass constraint on the K^0_S meson.

The effects of bin migration are evaluated for both $B^+ \to D\pi^+$ and $B^0 \to DK^{*0}$ decays by generating 10 million events across the Dalitz plane for each decay. The Dalitz plot distributions of the decays of D^0 mesons are taken from an amplitude model [40]. The distributions of the decays of B^+ and B^0 mesons depend on the values of γ, r_B, and δ_B, which are taken from the LHCb combination [24] for $B^+ \to D\pi^+$ decays and from the measurements of γ, r_{B^0}, and δ_{B^0} in this analysis for $B^0 \to DK^{*0}$ decays. The generated (m^2_-, m^2_+) coordinates of each event are smeared using the resolution and correlation found in simulation. Each event is assigned a true bin based on its true coordinates and an alternative bin based on its smeared coordinates.

Figure 7.9 shows the ratio of the number of smeared events to the numbers of true events in each bin in $B^+ \to D\pi^+$ and $B^0 \to DK^{*0}$ decays. Small differences between the two decays can cause their F_i values to be different. The ratios between

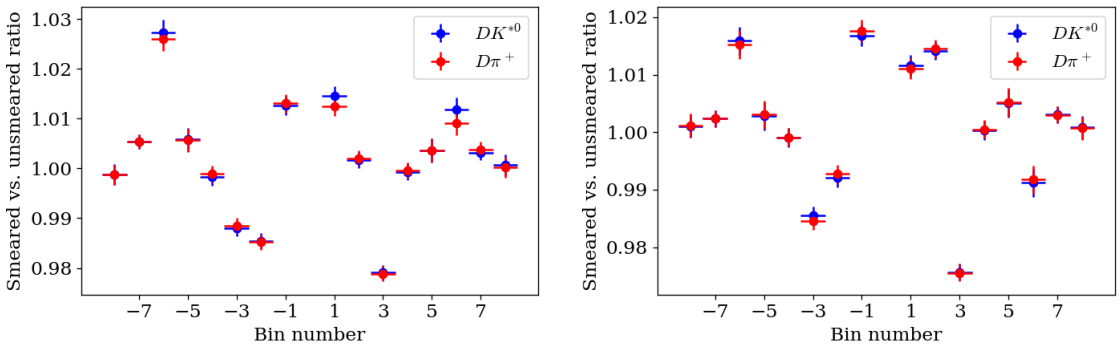

(a) LL tracks (b) DD tracks

Figure 7.9: Ratio between the number of events with smeared Dalitz coordinates and number of events with true coordinates in each bin of the Dalitz plot, for $B^+ \to D\pi^+$ decays (red) and $B^0 \to DK^{*0}$ decays (blue). The ratios are shown for (a) LL tracks and (b) DD tracks.

the $B^0 \to DK^{*0}$ and $B^+ \to D\pi^+$ ratios are used to calculate an alternative set of F_i values. Pseudoexperiments are generated using the alternative values and fitted with the default model. This leads to a small shift in the mean value of each observable compared with default pseudoexperiments, which is assigned as a systematic uncertainty.

Fitter bias correction

Each observable is corrected for small biases in the fit using Eq. 7.1. Due to the finite number of pseudoexperiments used to estimate the mean of the pull distribution, μ_{pull}, there is an associated uncertainty, σ_μ. A systematic uncertainty of $\sigma_\mu \times \sigma_{\text{meas}} \sim 0.001$ is propagated to each observable.

Summary of systematic uncertainties

The systematic uncertainties are summarised in Table. 7.2. The uncertainties from external measurements of the strong-phase parameters are presented separately. The systematic uncertainties from all other sources are added in quadrature to give the total experimental systematic uncertainties, which in all cases are found to be an order of magnitude smaller than the statistical uncertainties.

Table 7.4: Systematic uncertainties for the observables. Statistical uncertainties are given for reference.

Source	$\sigma(x_+)$	$\sigma(x_-)$	$\sigma(y_+)$	$\sigma(y_-)$
Statistical	0.076	0.083	0.106	0.098
Strong phase measurements	0.005	0.006	0.031	0.017
F_i inputs	0.008	0.007	0.002	0.001
Mass fit: α	0.001	0.001	0.001	0.003
Mass fit: g_{010}, g_{101}	0.000	0.000	0.000	0.001
Mass fit: $R_{s,\mathrm{low}}$	0.000	0.001	0.001	0.002
Mass fit: R_{low}	0.000	0.000	0.000	0.000
Mass fit: $R_{D\pi\pi}$	0.000	0.000	0.001	0.000
Mass fit: R_{DK}	0.002	0.002	0.002	0.001
Mass fit: signal shape	0.000	0.002	0.003	0.001
Mass fit: $B^0 \to D^* K^{*0}$ *CP* violation	0.001	0.001	0.004	0.003
Value of κ	0.001	0.000	0.003	0.001
Charmless background	0.002	0.002	0.005	0.006
Bin migration	0.001	0.000	0.004	0.000
Fitter bias	0.001	0.001	0.001	0.001
Total experimental	0.009	0.008	0.009	0.008

7.3 Summary of results

The *CP* violation observables are determined to be

$$\begin{aligned} x_+ &= 0.046 \pm 0.077 \pm 0.005 \pm 0.009, \\ x_- &= -0.249 \pm 0.084 \pm 0.006 \pm 0.008, \\ y_+ &= -0.160 \pm 0.114 \pm 0.031 \pm 0.009, \\ y_- &= 0.188 \pm 0.105 \pm 0.017 \pm 0.008, \end{aligned}$$

where the first uncertainty is statistical, the second is the systematic uncertainty from the strong-phase inputs, and the third is the systematic uncertainty from all other sources. The combined statistical and systematic correlation matrix is given in Table 7.5. Interpretation of the observables in terms of γ is discussed in Chap. 8.

Figure 7.10 shows the central values and 1σ and 2σ likelihood contours of (x_+, y_+) and (x_-, y_-) on a two-dimensional plot. In the absence of *CP* violation ($\gamma = 0$), both points would be at the same position. The points are separated by more than two standard deviations, which hints at the presence of *CP* violation in these decays. The opening angle between the lines joining the two points to the origin is equal to 2γ.

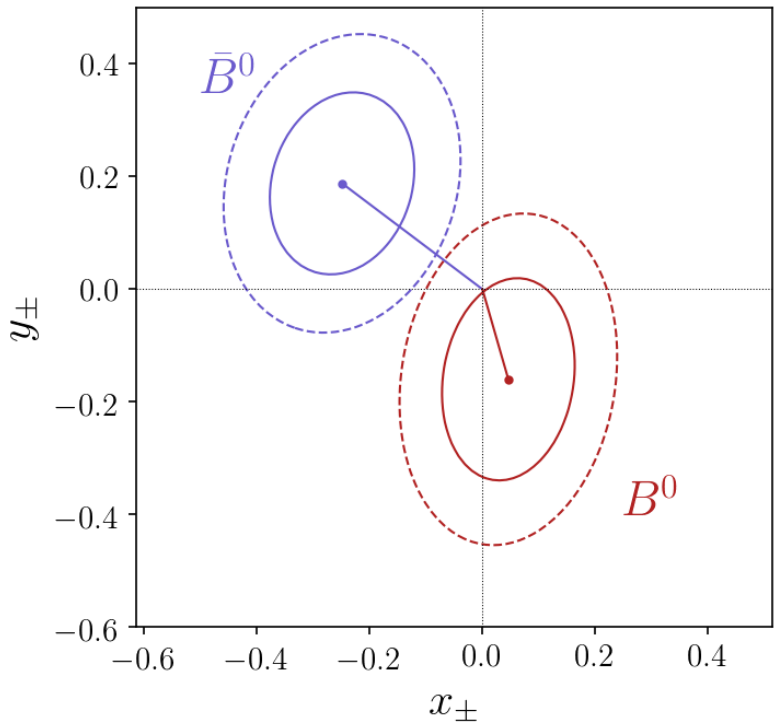

Figure 7.10: Two-dimensional 68.3% (solid line) and 95.5% (dotted line) confidence regions for the measured $(x_\pm, y_\pm)$ values. The red contours correspond to x_+ and y_+, which are measured from decays of B^0 mesons, while the blue contours correspond to x_- and y_-, which are measured from decays of $\overline{B}^0$ mesons.

Table 7.5: Combined statistical and systematic correlation matrix for the observables.

	x_+	x_-	y_+	y_-
x_+	1.00	−0.00	0.14	−0.00
x_-	−0.00	1.00	−0.01	0.16
y_+	0.14	−0.01	1.00	−0.02
y_-	−0.00	0.16	−0.02	1.00

Chapter 8

Determination of the CKM angle γ

In this chapter, the ADS/GLW and GGSZ *CP* observables are used to determine constraints on the CKM angle γ and the hadronic parameters r_{B^0} and δ_{B^0} using a method described in Sect. 8.1. Constraints from the ADS/GLW results alone are presented in Sect. 8.2, and constraints from the GGSZ results alone are presented in Sect. 8.3. The results are combined in Sect. 8.4, and future prospects for studies of γ using the decays of B^0 mesons at LHCb are discussed in Sect. 8.5.

8.1 Method for determining γ

Each analysis measures a set of *CP* observables $\boldsymbol{x}_m$ and a covariance matrix V_0, which includes the statistical and systematic uncertainties and their correlations. The observables are related to the underlying parameters γ, r_{B^0}, and δ_{B^0} through some defining equations. Using these equations, we can take any point in $(\gamma, r_{B^0}, \delta_{B^0})$ space and predict the set of observables at that point, $\boldsymbol{x}(\gamma, r_{B^0}, \delta_{B^0})$. We then calculate the χ^2 at that point using

$$\chi^2(\gamma, r_{B^0}, \delta_{B^0}) = (\boldsymbol{x}(\gamma, r_{B^0}, \delta_{B^0}) - \boldsymbol{x}_m)^T \, V_0^{-1} \, (\boldsymbol{x}(\gamma, r_{B^0}, \delta_{B^0}) - \boldsymbol{x}_m). \tag{8.1}$$

Points in $(\gamma, r_{B^0}, \delta_{B^0})$ space are scanned to find the global minimum, χ^2_{min}. This point represents the best estimate of the underlying parameters.

The confidence in the global minimum is quantified by examining the difference between the χ^2 value at each point in the scan and the global minimum value,

$\Delta\chi^2(\gamma, r_{B^0}, \delta_{B^0}) = \chi^2(\gamma, r_{B^0}, \delta_{B^0}) - \chi^2_{\text{min}}$. If we assume that the parameters are normally distributed, we can draw contours at $\Delta\chi^2 = 2.30$, 6.18, and 11.8 corresponding to confidence levels of 68.3%, 95.5%, and 99.7%, respectively. The quoted uncertainties on γ, r_{B^0}, and δ_{B^0} in this chapter are the 68.3% confidence levels.

There is an irremovable degeneracy of 180° in the value of γ. By convention, we consider only solutions in the range $0 < \gamma < 180°$, which corresponds to the Standard Model expectation.

8.2 Measurement using two- and four-body D-meson final states

The first measurement in this thesis uses $5\,\text{fb}^{-1}$ of data collected from 2011–2012 and 2015–2016 to measure the twelve ADS/GLW observables. The defining equations relating the two-body observables to the underlying parameters are Eqs. 2.31, 2.33, 2.37, and 2.37, which are modified as described in Sect. 2.6.3 to describe the four-body observables. The measured observables are given in Chap. 5.

In addition to the parameters of interest, the observables depend on the following parameters: κ, r_D, δ_D, $F_+^{4\pi}$, $r_D^{K3\pi}$, $\delta_D^{K3\pi}$, and $\kappa_D^{K3\pi}$. These auxiliary parameters are constrained to the values in Table 8.1 and are used when calculating $\boldsymbol{x}(\gamma, r_{B^0}, \delta_{B^0})$ at each point in the χ^2 scan. The calculated observables are also corrected for charm mixing using the parameters x_D and y_D [29], and for CP violation in the D-meson system using the parameter ΔA_{CP} [21], whose values are also given in Table 8.1; the effects of these corrections are very small.

Two-dimensional projections of the scan results with contours drawn at the 68.3%, 95.5%, and 99.7% confidence levels are shown in Fig. 8.1. As expected, there is a degeneracy in the (γ, δ_{B^0}) plane due to the trigonometric form of the relationships between the observables and $\delta_{B^0} \pm \gamma$. There are four favoured solutions in the region $0 < \gamma < 180°$, two of which are compatible with the existing LHCb determination of γ [24].

Table 8.1: Values of the external inputs used as constraints in the fit to determine the parameters of interest.

Parameter	Value	
κ	$0.958\,^{+0.005}_{-0.046}$	[45]
r_D	$(5.87 \pm 0.02) \times 10^{-2}$	[29]
δ_D	$(192.1\,^{+8.6}_{-10.2})^\circ$	[29]
$F_+^{4\pi}$	0.769 ± 0.023	[32]
$r_D^{K3\pi}$	$(5.49 \pm 0.06) \times 10^{-2}$	[35]
$\delta_D^{K3\pi}$	$(128\,^{+28}_{-17})^\circ$	[35]
$\kappa^{K3\pi}$	$0.43\,^{+0.17}_{-0.13}$	[35]
x_D	$(0.39\,^{+0.11}_{-0.12})\%$	[29]
y_D	$(0.651\,^{+0.063}_{-0.069})\%$	[29]
ΔA_{CP}	$(-15.4 \pm 2.9) \times 10^{-4}$	[21]

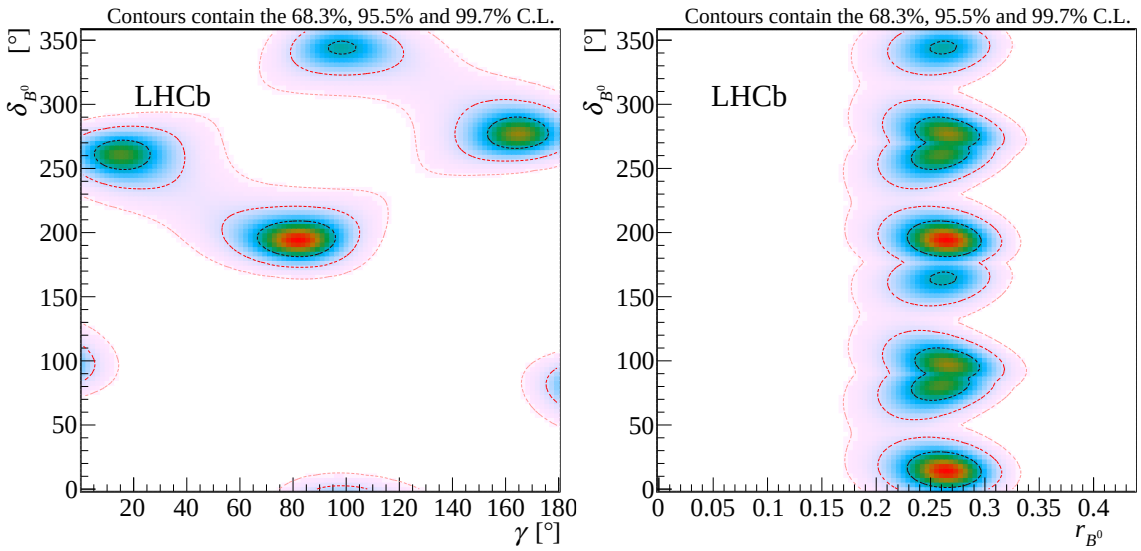

Figure 8.1: Contour plots showing 2D scans of (left) δ_{B^0} versus γ and (right) δ_{B^0} versus r_{B^0} using the ADS/GLW modes.

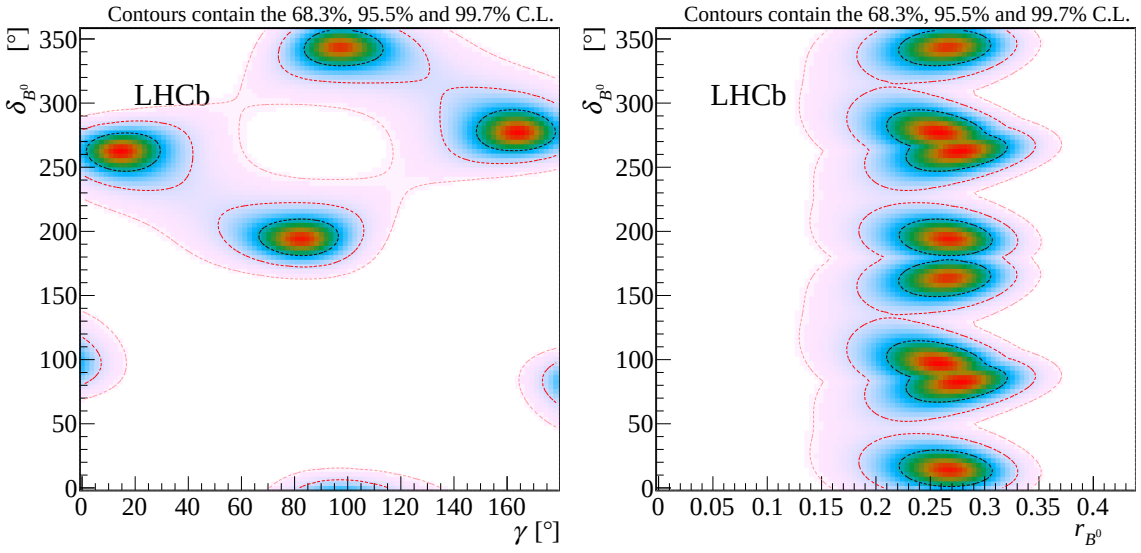

Figure 8.2: Contour plots showing 2D scans of (left) δ_{B^0} versus γ and (right) δ_{B^0} versus r_{B^0} using two-body D-meson decays alone.

A single solution for r_{B^0} is found to be

$$r_{B^0} = 0.265\,^{+0.022}_{-0.023}.$$

This measurement is consistent with, and more accurate than, the previous measurement by LHCb in Ref. [44]. In accordance with expectation, this value of r_{B^0} is almost a factor of three larger than the corresponding parameter in $B^+ \to DK^+$ decays, $r_{B^+} = 0.099 \pm 0.005$ [24].

This is the first study of $B^0 \to DK^{*0}$ decays at LHCb using four-body D-meson final states. The benefits of including the four-body modes are clear when we consider the two-body results alone, shown in Fig. 8.2. The four solutions in (γ, δ_{B^0}) space are equally probable, in contrast to the scans in Fig. 8.1 where the solution at $\gamma \sim 80°$ is favoured. The four-body modes both improve the constraints and provide distinction between the degenerate minima.

8.3 Measurement using three-body D-meson final states

The full LHCb Run 1 and Run 2 data set, corresponding to $9\,\text{fb}^{-1}$ of data collected from 2011–2012 and 2015–2018, is used to measure the GGSZ observables defined in Eqs. 2.56 and 2.57 using a model-independent Dalitz plot analysis. The measured observables are given in Chap. 7. Figure 8.3 shows the results of the χ^2 scan for these observables.

While the GGSZ analysis has lower yields than the ADS/GLW analysis, and therefore produces weaker constraints, the use of Cartesian parameters allows us to measure a single value for each underlying parameter.[1] The parameters at the global minimum χ^2 are

$$\begin{aligned}\gamma &= (68 \pm 14)^\circ,\\ r_{B^0} &= 0.26 \pm 0.07,\\ \delta_{B^0} &= (212 \pm 14)^\circ.\end{aligned}$$

The value of of r_{B^0} is consistent with the more-precise value from the ADS/GLW measurement, while the values of γ and δ_{B^0} are consistent with the favoured solution in the ADS/GLW scan shown in Fig. 8.1.

8.4 Combined measurement

The most powerful constraints are found by combining the two sets of results. Figure 8.4 shows two-dimensional projections of $(\gamma, r_{B^0}, \delta_{B^0})$ space from a scan using both sets of observables. The inclusion of the GGSZ observables completely resolves the degeneracy in the ADS/GLW measurement. The underlying parameters are determined to be

$$\begin{aligned}\gamma &= (77\,^{+8}_{-9})^\circ,\\ r_{B^0} &= 0.258\,^{+0.022}_{-0.023},\\ \delta_{B^0} &= (200 \pm 8)^\circ.\end{aligned}$$

[1] The second solution in (r_{B^0}, δ_{B^0}) space corresponds to the degenerate solution in the region $180^\circ < \gamma < 360^\circ$, which is ignored.

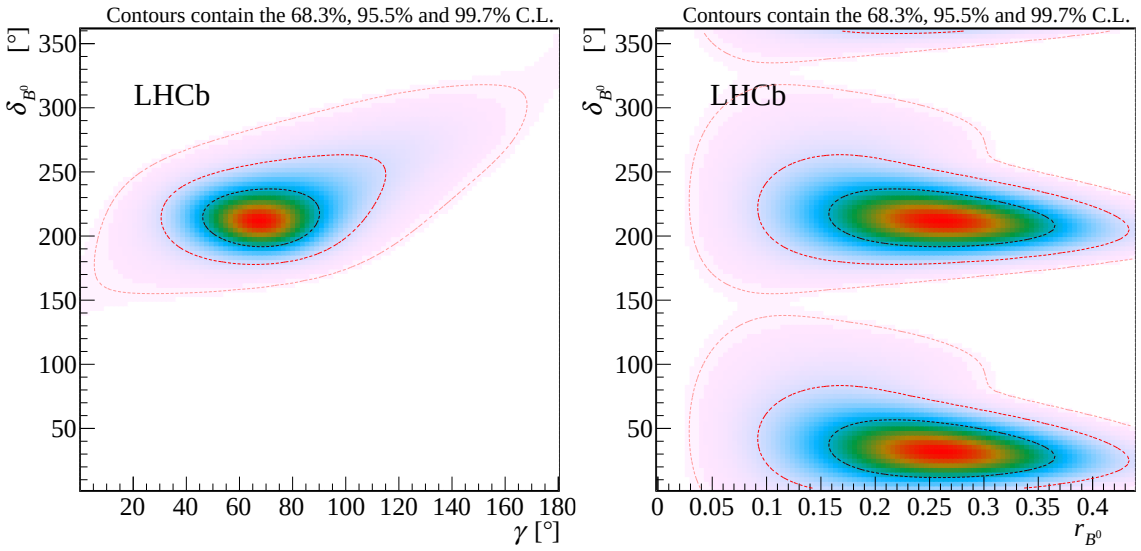

Figure 8.3: Contour plots showing 2D scans of (left) δ_{B^0} versus γ and (right) δ_{B^0} versus r_{B^0} using the GGSZ modes.

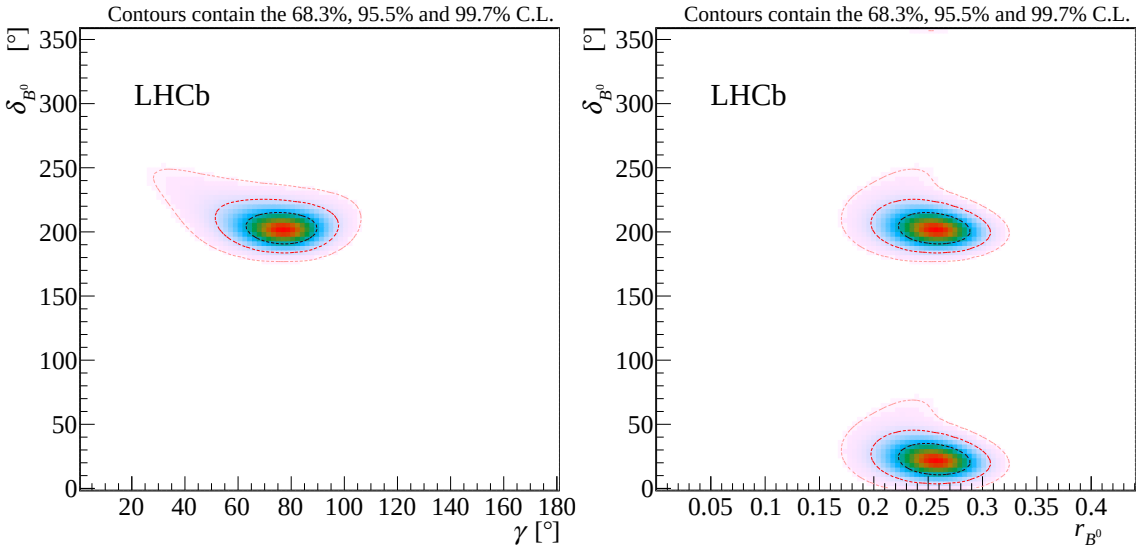

Figure 8.4: Contour plots showing 2D scans of (left) δ_{B^0} versus γ and (right) δ_{B^0} versus r_{B^0} using a combination of the ADS/GLW and GGSZ modes.

These are the world-best measurements of r_{B^0} and δ_{B^0}, and the most precise measurement of γ using only B^0-meson decays. The value of γ is consistent with the LHCb average from decays of B^+ mesons, $\gamma = (69.8\,^{+5.9}_{-7.1})^\circ$ [24]. It is also consistent with the indirect measurement $\gamma = (65.66\,^{+0.90}_{-2.65})^\circ$, and is therefore compatible with the Standard Model prediction.

8.5 Future prospects

The results presented in this thesis use the full $9\,\text{fb}^{-1}$ of LHCb data for the GGSZ measurement, but only $5\,\text{fb}^{-1}$ of data for the ADS/GLW measurement, which was performed before the end of Run 2. Data for the ADS/GLW modes collected from 2017–2018 are now available, and while a dedicated study with accurate correction factors and systematic uncertainties has not yet been completed, a preliminary invariant-mass fit to the full $9\,\text{fb}^{-1}$ of data using the fit model from Chap. 4 has been performed. The fit finds 3370 ± 60 signal candidates in the favoured $D \to K\pi$ mode, which is twice as large as the yield in the 2011–2016 data.

To estimate the improvement from using the full data set, a parameter scan is performed using the statistical uncertainties found in the preliminary $9\,\text{fb}^{-1}$ fit while keeping the central values and systematic uncertainties from the $5\,\text{fb}^{-1}$ analysis. The scan includes both the ADS/GLW and GGSZ results. The two-dimensional confidence plots are shown in Fig. 8.5. The χ^2 minimisation yields the following parameters and uncertainties:

$$\begin{aligned} \gamma &= (79 \pm 6)^\circ, \\ r_{B^0} &= 0.261\,^{+0.015}_{-0.016}, \\ \delta_{B^0} &= (197 \pm 6)^\circ, \end{aligned}$$

therefore the additional data that has already been collected has the potential to reduce the uncertainty on γ by 2–3°.

Following a period of upgrades to the detector, the LHCb experiment will resume data taking in 2021. It is anticipated that around $15\,\text{fb}^{-1}$ of pp collision data will be collected in Run 3 at a centre-of-mass energy of 14 TeV [80]. The increased collision

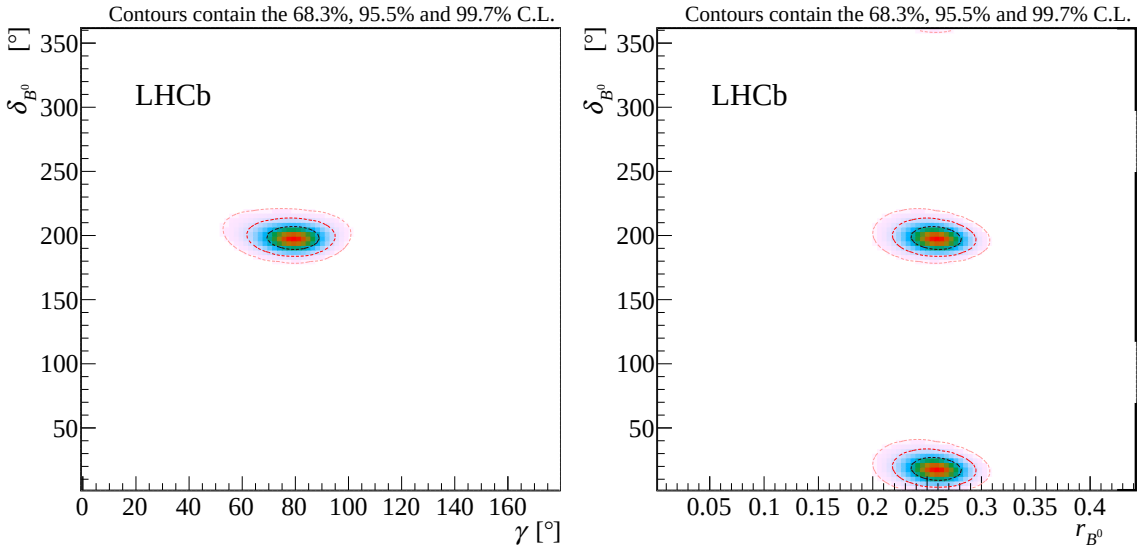

Figure 8.5: Contour plots showing 2D scans of (left) δ_{B^0} versus γ and (right) δ_{B^0} versus r_{B^0} using a combination of the ADS/GLW and GGSZ modes with the full Run 1 and Run 2 data set. The statistical uncertainties for the ADS/GLW modes are estimated using a preliminary fit to the full data set, although a dedicated analysis has not yet been performed.

energy and upgrades to the detector performance and trigger, in particular the switch to a fully software trigger [81], mean that we can expect at least twice as many signal events per fb^{-1} in Run 3 compared with Run 2. Therefore, by the end of Run 3 the number of collected $B^0 \to DK^{*0}$ decays will be around six times as large as the current sample.

The projected uncertainties on the underlying parameters at the end of Run 3 are estimated by performing a χ^2 scan with the uncertainties of the observables reduced by a factor of $1/\sqrt{6}$ and assuming that the central values are unchanged. The scan results are shown in Fig. 8.6. The central values and uncertainties for the underlying parameters are

$$\begin{aligned} \gamma &= (79.4 \pm 2.6)^\circ, \\ r_{B^0} &= 0.260 \pm 0.006, \\ \delta_{B^0} &= (197\ ^{+2.4}_{-2.3})^\circ. \end{aligned}$$

The projected uncertainty on γ is around half the size of the current LHCb uncertainty using all decay channels [24]. The other channels contributing to the global LHCb average will themselves improve in sensitivity following the growing size of the

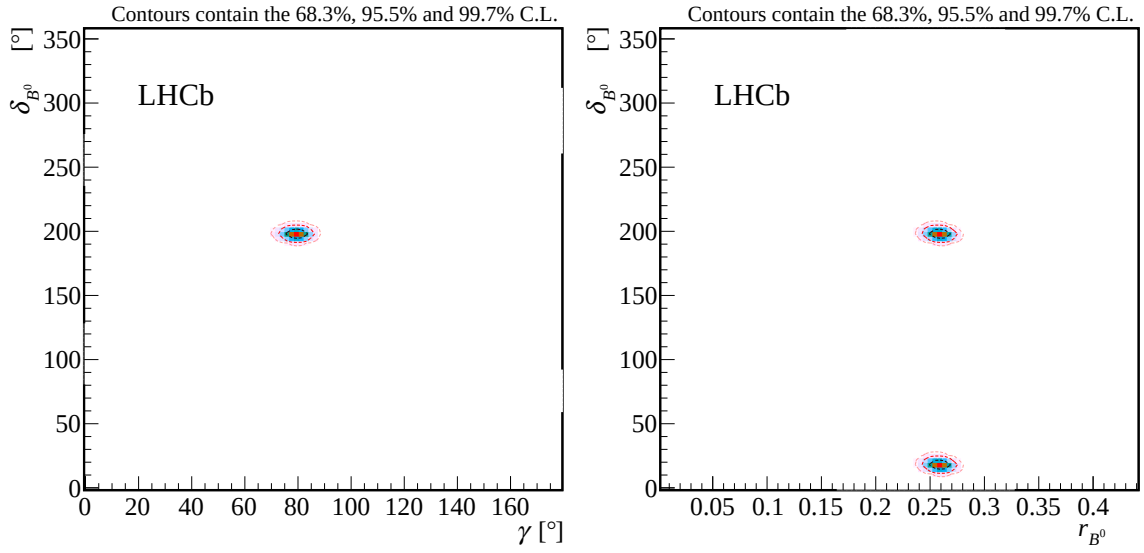

Figure 8.6: Contour plots showing 2D scans of (left) δ_{B^0} versus γ and (right) δ_{B^0} versus r_{B^0} using a combination of the ADS/GLW and GGSZ modes, with the uncertainties on the measured observables reduced to reflect the projected increase in data by the end of Run 3.

data set, and will also be enhanced by improvements to analysis methods, such as performing a binned fit to the $D \to K^{\pm}\pi^{\mp}\pi^{+}\pi^{-}$ modes [36] rather than an inclusive analysis.

Other powerful ways to exploit the $B^0 \to DK^+\pi^-$ system that do not restrict the phase space to the $K^*(892)^0$ region will become increasingly important. Amplitude analyses of the $DK^+\pi^-$ Dalitz plot can be used to obtain more information on γ than is available in the quasi-two-body analysis presented here, in particular from the interference between the $B^0 \to DK^*(892)^0$ and $B^0 \to D_2^*(2460)^-K^+$ amplitudes. A study of the full phase space with two-body D-meson decays has been performed with Run 1 data [45], and a "double Dalitz" analysis of $D \to K^0_S\pi^+\pi$ decays exploiting both the $DK^+\pi^-$ Dalitz space and the $K^0_S\pi^+\pi^-$ Dalitz space has been proposed [82].

Measurements of the decays of B^0 mesons will provide an important contribution to the overall precision at end of Run 3, at which point the overall uncertainty on γ from LHCb measurements is expected to be 1.5° [80]. This is a big step towards our ultimate goal of sub-degree precision, which LHCb aims to achieve by 2030 with an integrated luminosity of $50\,\text{fb}^{-1}$ [80]. The Belle II experiment will also contribute

significantly to the global average, with a projected $50\,\text{ab}^{-1}$ of data collected by 2026 providing a precision of 1.5° on γ [80]. Belle II will be particularly powerful for decays involving K^0_S mesons, such as the GGSZ modes, as it has a high reconstruction efficiency for these modes. However, results from LHCb are expected to continue to dominate the γ world average, with a precision of 0.35° predicted by the end of its lifetime [80]. This will allow us to probe for the effects of New Physics by testing the Standard Model to unprecedented levels.

Chapter 9

Conclusions

Two measurements of *CP* violation in $B^0 \to DK^{*0}$ decays have been made using proton-proton collision data collected by the LHCb experiment. In the first, the D meson is reconstructed in the two-body final states $K^+\pi^-$, π^+K^-, K^+K^-, and $\pi^+\pi^-$, and, for the first time, the four-body final states $K^+\pi^-\pi^+\pi^-$, $\pi^+K^-\pi^+\pi^-$, and $\pi^+\pi^-\pi^+\pi^-$. The analysis uses data corresponding to integrated luminosities of 1, 2, and 2 fb^{-1} collected at centre-of-mass energies of 7, 8, and 13 TeV, respectively. The data are used to measure the ADS/GLW *CP* observables, which are constructed from yield ratios and asymmetries. The results are

$$
\begin{aligned}
\mathcal{A}_{CP}^{KK} &= -0.05 \pm 0.10 \pm 0.01, \\
\mathcal{A}_{CP}^{\pi\pi} &= -0.18 \pm 0.14 \pm 0.01, \\
\mathcal{R}_{CP}^{KK} &= 0.92 \pm 0.10 \pm 0.02, \\
\mathcal{R}_{CP}^{\pi\pi} &= 1.32 \pm 0.19 \pm 0.03, \\
\mathcal{A}_{CP}^{4\pi} &= -0.03 \pm 0.15 \pm 0.01, \\
\mathcal{R}_{CP}^{4\pi} &= 1.01 \pm 0.16 \pm 0.04, \\
\mathcal{R}_{+}^{\pi K} &= 0.064 \pm 0.021 \pm 0.002, \\
\mathcal{R}_{-}^{\pi K} &= 0.095 \pm 0.021 \pm 0.003, \\
\mathcal{R}_{+}^{\pi K\pi\pi} &= 0.074 \pm 0.026 \pm 0.002, \\
\mathcal{R}_{-}^{\pi K\pi\pi} &= 0.072 \pm 0.025 \pm 0.003, \\
\mathcal{A}_{\text{ADS}}^{K\pi} &= 0.047 \pm 0.027 \pm 0.010, \\
\mathcal{A}_{\text{ADS}}^{K\pi\pi\pi} &= 0.037 \pm 0.032 \pm 0.010,
\end{aligned}
$$

where the first uncertainty is statistical and the second is systematic. First observations are obtained for the decays $B^0 \to D(\pi^+K^-)K^{*0}$ and $B^0 \to D(\pi^+\pi^-\pi^+\pi^-)K^{*0}$

with significances of 5.8σ and 8.4σ, respectively. Strong evidence for the decay $B^0 \to D(\pi^+K^-\pi^+\pi^-)K^{*0}$ is also found with a significance of 4.4σ.

A second study is presented with the D meson reconstructed in the self-conjugate three-body final states $K^0_S\pi^+\pi^-$ and $K^0_S K^+K^-$, using an additional $4\,\text{fb}^{-1}$ of 13 TeV collision data with respect to the first analysis. Measurements of the GGSZ *CP*-violation parameters $x_\pm \equiv r_{B^0}\cos(\delta_{B^0} \pm \gamma)$ and $y_\pm \equiv r_{B^0}\sin(\delta_{B^0} \pm \gamma)$ are made, where γ is the complex phase of the CKM matrix, and r_{B^0} and δ_{B^0} are the magnitude ratio and strong-phase difference, respectively, between the amplitudes of $B^0 \to D^0K^{*0}$ and $B^0 \to \overline{D}^0K^{*0}$ decays. This measurement finds

$$\begin{aligned} x_+ &= 0.046 \pm 0.077 \pm 0.005 \pm 0.009, \\ x_- &= -0.249 \pm 0.084 \pm 0.006 \pm 0.008, \\ y_+ &= -0.160 \pm 0.114 \pm 0.031 \pm 0.009, \\ y_- &= 0.188 \pm 0.105 \pm 0.017 \pm 0.008, \end{aligned}$$

where the first uncertainty is statistical, the second is the systematic uncertainty related to the knowledge of the D-meson strong-phase parameters, and the third is the systematic uncertainty from all other sources.

The two sets of measurements comprise the world's most precise determinations of the ADS/GLW and GGSZ *CP*-violation parameters in $B^0 \to DK^{*0}$ decays. The results are combined in a χ^2 minimisation to find

$$\begin{aligned} \gamma &= (77\,^{+8}_{-9})^\circ, \\ r_{B^0} &= 0.258\,^{+0.022}_{-0.023}, \\ \delta_{B^0} &= (200 \pm 8)^\circ. \end{aligned}$$

constituting the world-best measurements of r_{B^0} and δ_{B^0}, and the most precise determination of γ using only B^0-meson decays. The uncertainty on γ is expected to decrease by 2–3° once the additional $4\,\text{fb}^{-1}$ of collected LHCb data are included in the ADS/GLW analysis.

This direct measurement of γ is compatible with the world-average indirect measurement, in accordance with the Standard Model prediction. It is also consistent with the LHCb average determined using decays of B^+ mesons. These measurements

constitute a valuable cross-check of the B^+-meson results, and will have a significant weight in the overall LHCb determination of γ from all sources when such a combination is next performed.

The results presented in this thesis are some of the many CP-violation measurements that will eventually improve the precision of the direct measurement of γ to less than a degree. This is an important test of the Standard Model, as an inconsistency between the direct and indirect measurements of γ would provide conclusive evidence for physics beyond the Standard Model.

References

[1] CKMfitter group, J. Charles *et al.*, *Current status of the standard model CKM fit and constraints on $\Delta F = 2$ new physics*, Phys. Rev. **D91** (2015) 073007, arXiv:1501.05013, updated results and plots available at http://ckmfitter.in2p3.fr/.

[2] LHCb collaboration, R. Aaij *et al.*, *Measurement of CP observables in the process $B^0 \to DK^{*0}$ with two- and four-body D decays*, JHEP **08** (2019) 041, arXiv:1906.08297.

[3] LHCb collaboration, R. Aaij *et al.*, *Observation of exotic $J/\psi\,\phi$ structures from amplitude analysis of $B^+ \to J/\psi\,\phi K^+$ decays*, Phys. Rev. Lett. **118** (2017) 022003, arXiv:1606.07895.

[4] LHCb collaboration, R. Aaij *et al.*, *Observation of $J/\psi\,p$ resonances consistent with pentaquark states in $\Lambda_b^0 \to J/\psi\,pK^-$ decays*, Phys. Rev. Lett. **115** (2015) 072001, arXiv:1507.03414.

[5] ATLAS collaboration, G. Aad *et al.*, *Observation of a new particle in the search for the Standard Model Higgs boson with the ATLAS detector at the LHC*, Phys. Lett. **B716** (2012) 1, arXiv:1207.7214.

[6] CMS collaboration, S. Chatrchyan *et al.*, *Observation of a new boson at a mass of 125 GeV with the CMS experiment at the LHC*, Phys. Lett. **B716** (2012) 30, arXiv:1207.7235.

[7] N. Cabibbo, *Unitary symmetry and leptonic decays*, Phys. Rev. Lett. **10** (1963) 531.

[8] M. Kobayashi and T. Maskawa, *CP-violation in the renormalizable theory of weak interaction*, Prog. Theor. Phys. **49** (1973) 652.

[9] L. Wolfenstein, *Parametrization of the Kobayashi–Maskawa matrix*, Phys. Rev. Lett. **51** (1983) 1945.

[10] A. D. Sakharov, *Violation of CP invariance, C asymmetry, and baryon asymmetry of the universe*, Sov. Phys. Usp. **34** (1991) 392.

[11] J. H. Christenson, J. W. Cronin, V. L. Fitch, and R. Turlay, *Evidence for the* 2π *decay of the* K_2^0 *meson*, Phys. Rev. Lett. **13** (1964) 138.

[12] KTeV Collaboration, A. Alavi-Harati *et al.*, *Observation of direct CP violation in* $K_{S,L} \to \pi\pi$ *decays*, Phys. Rev. Lett. **83** (1999) 22, `arXiv:hep-ex/9905060`.

[13] Belle Collaboration, K. Abe *et al.*, *Observation of large CP violation in the neutral B meson system*, Phys. Rev. Lett. **87** (2001) 091802, `arXiv:hep-ex/0107061`.

[14] BaBar collaboration, B. Aubert *et al.*, *Observation of CP violation in the* B^0 *meson system*, Phys. Rev. Lett. **87** (2001) 091801, `arXiv:hep-ex/0107013`.

[15] BaBar collaboration, B. Aubert *et al.*, *Observation of direct CP violation in* $B^0 \to K^+\pi^-$ *decays*, Phys. Rev. Lett. **93** (2004) 131801, `arXiv:hep-ex/0407057`.

[16] Belle collaboration, Y. Chao *et al.*, *Improved measurements of partial rate asymmetry in* $B \to hh$ *decays*, Phys. Rev. **D71** (2005) 031502, `arXiv:hep-ex/0407025`.

[17] BaBar collaboration, P. del Amo Sanchez *et al.*, *Evidence for direct CP violation in the measurement of the Cabbibo-Kobayashi-Maskawa angle γ with $B^{\mp} \to D^{(*)}K^{(*)\mp}$ decays*, Phys. Rev. Lett. **105** (2010) 121801.

[18] Belle collaboration, A. Poluektov *et al.*, *Evidence for direct CP violation in the decay $B^{\pm} \to D^{(*)}K^{\pm}$, $D \to K^0_S\pi^+\pi^-$ and measurement of the CKM phase ϕ_3*, Phys. Rev. **D81** (2010) 112002.

[19] LHCb collaboration, R. Aaij *et al.*, *Observation of CP violation in $B^{\pm} \to DK^{\pm}$ decays*, Phys. Lett. **B712** (2012) 203, Erratum ibid. **B713** (2012) 351, arXiv:1203.3662.

[20] LHCb collaboration, R. Aaij *et al.*, *First observation of CP violation in the decays of B^0_s mesons*, Phys. Rev. Lett. **110** (2013) 221601, arXiv:1304.6173.

[21] LHCb collaboration, R. Aaij *et al.*, *Observation of CP violation in charm decays*, Phys. Rev. Lett. **122** (2019) 211803, arXiv:1903.08726.

[22] T2K collaboration, K. Abe *et al.*, *Constraint on the matter–antimatter symmetry-violating phase in neutrino oscillations*, Nature **580** (2020) 339.

[23] LHCb collaboration, R. Aaij *et al.*, *Measurement of the CKM angle γ from a combination of LHCb results*, JHEP **12** (2016) 087, arXiv:1611.03076.

[24] LHCb collaboration, *Update of the LHCb combination of the CKM angle γ using $B \to DK$ decays*, LHCb-CONF-2018-002, 2018.

[25] M. Gronau and D. Wyler, *On determining a weak phase from charged B decay asymmetries*, Phys. Lett. **B265** (1991) 172.

[26] M. Gronau and D. London, *How to determine all the angles of the unitarity triangle from $B^0_d \to DK_S$ and $B^0_s \to D\phi$*, Phys. Lett. **B253** (1991) 483.

[27] D. Atwood, I. Dunietz, and A. Soni, *Enhanced CP violation with $B \to KD^0(\overline{D}^0)$ modes and extraction of the Cabibbo–Kobayashi–Maskawa angle γ*, Phys. Rev. Lett. **78** (1997) 3257, arXiv:hep-ph/9612433.

[28] D. Atwood, I. Dunietz, and A. Soni, *Improved methods for observing CP violation in $B^\pm \to KD$ and measuring the CKM phase γ*, Phys. Rev. **D63** (2001) 036005, arXiv:hep-ph/0008090.

[29] Heavy Flavor Averaging Group, Y. Amhis *et al.*, *Averages of b-hadron, c-hadron, and τ-lepton properties as of summer 2016*, Eur. Phys. J. **C77** (2017) 895, arXiv:1612.07233.

[30] M. Nayak *et al.*, *First determination of the CP content of $D \to \pi^+\pi^-\pi^0$ and $D \to K^+K^-\pi^0$*, Phys. Lett. **B740** (2015) 1, arXiv:1410.3964.

[31] S. Malde *et al.*, *First determination of the CP content of $D \to \pi^+\pi^-\pi^+\pi^-$ and updated determination of the CP contents of $D \to \pi^+\pi^-\pi^0$ and $D \to K^+K^-\pi^0$*, Phys. Lett. **B747** (2015) 9, arXiv:1504.05878.

[32] S. Harnew *et al.*, *Model-independent determination of the strong phase difference between D^0 and $\overline{D}^0 \to \pi^+\pi^-\pi^+\pi^-$ amplitudes*, JHEP **01** (2018) 144, arXiv:1709.03467.

[33] D. Atwood and A. Soni, *Role of a charm factory in extracting CKM-phase information via $B \to DK$*, Phys. Rev. **D68** (2003) 033003, arXiv:hep-ph/0304085.

[34] LHCb collaboration, R. Aaij *et al.*, *First observation of $D^0 - \overline{D}^0$ oscillations in $D^0 \to K^+\pi^+\pi^-\pi^-$ decays and a measurement of the associated coherence parameters*, Phys. Rev. Lett. **116** (2016) 241801, arXiv:1602.07224.

[35] T. Evans *et al.*, *Improved determination of the $D \to K^-\pi^+\pi^+\pi^-$ coherence factor and associated hadronic parameters from a combination of $e^+e^- \to \psi(3770) \to c\bar{c}$ and $pp \to c\bar{c}X$ data*, Phys. Lett. **B757** (2016) 520, Erratum ibid. **B765** (2017) 402, arXiv:1602.07430.

[36] T. Evans, J. Libby, S. Malde, and G. Wilkinson, *Improved sensitivity to the CKM phase γ through binning phase space in $B^- \to DK^-$, $D \to K^+\pi^-\pi^-\pi^+$ decays*, Phys. Lett. **B802** (2020) 135188.

[37] A. Giri, Y. Grossman, A. Soffer, and J. Zupan, *Determining γ using $B^\pm \to \mathrm{DK}^\pm$ with multibody D decays*, Phys. Rev. **D68** (2003) 054018.

[38] R. H. Dalitz, *On the analysis of τ-meson data and the nature of the τ-meson*, Phil. Mag. Ser. 7 **44** (1953) 1068.

[39] F. Cheung, *Measurements of the CKM angle γ at the LHCb experiment*, DPhil thesis, Univ. of Oxford, 2016, Presented 26 Aug 2016, CERN-THESIS-2016-227.

[40] BaBar and Belle collaborations, I. Adachi *et al.*, *Measurement of $\cos 2\beta$ in $B^0 \to D^{(*)}h^0$ with $D \to K^0_S\pi^+\pi^-$ decays by a combined time-dependent Dalitz plot analysis of BaBar and Belle data*, Phys. Rev. **D98** (2018) 112012, arXiv:1804.06153.

[41] BaBar collaboration, B. Aubert *et al.*, *Improved measurement of the CKM angle γ in $B^\mp \to D^{(*)}K^{(*)\mp}$ decays with a Dalitz plot analysis of D decays to $K^0_S\pi^+\pi^-$ and $K^0_S K^+K^-$*, Phys. Rev. **D78** (2008) 034023, arXiv:0804.2089.

[42] CLEO collaboration, J. Libby *et al.*, *Model-independent determination of the strong-phase difference between D^0 and $\overline{D}^0 \to K^0_{S,L}h^+h^-$ ($h = \pi, K$) and its impact on the measurement of the CKM angle γ/ϕ_3*, Phys. Rev. **D82** (2010) 112006, arXiv:1010.2817.

[43] BESIII collaboration, M. Ablikim *et al.*, *Model-independent determination of the relative strong-phase difference between D^0 and $\overline{D}^0 \to K^0_{S,L}\pi^+\pi^-$ and its impact on the measurement of the CKM angle γ/ϕ_3*, arXiv:2003.00091.

[44] LHCb collaboration, R. Aaij *et al.*, *Measurement of CP violation parameters in $B^0 \to DK^{*0}$ decays*, Phys. Rev. **D90** (2014) 112002, arXiv:1407.8136.

[45] LHCb collaboration, R. Aaij *et al.*, *Constraints on the unitarity triangle angle γ from Dalitz plot analysis of $B^0 \to DK^+\pi^-$ decays*, Phys. Rev. **D93** (2016) 112018, Erratum ibid. **D94** (2016) 079902, arXiv:1602.03455.

[46] BaBar collaboration, B. Aubert *et al.*, *Search for $b \to u$ transitions in $B^0 \to DK^{*0}$ decays*, Phys. Rev. **D80** (2009) 031102, arXiv:0904.2112.

[47] Belle collaboration, K. Negishi *et al.*, *Search for the decay $B^0 \to DK^{*0}$ followed by $D \to K^-\pi^+$*, Phys. Rev. **D86** (2012) 011101, arXiv:1205.0422.

[48] Belle collaboration, K. Negishi *et al.*, *First model-independent Dalitz analysis of $B^0 \to DK^{*0}$, $D \to K^0_S\pi^+\pi^-$ decay*, PTEP **2016** (2016) 043C01, arXiv:1509.01098.

[49] LHCb collaboration, R. Aaij *et al.*, *Measurement of the CKM angle γ using $B^0 \to DK^{*0}$ with $D \to K^0_S\pi^+\pi^-$ decays*, JHEP **08** (2016) 137, arXiv:1605.01082.

[50] LHCb collaboration, R. Aaij *et al.*, *Search for CP violation and observation of P violation in $\Lambda^0_b \to p\pi^-\pi^+\pi^-$ decays*, arXiv:1912.10741, submitted to PRL.

[51] LHCb collaboration, R. Aaij *et al.*, *Model-independent measurement of the CKM angle γ using $B^0 \to DK^{*0}$ decays with $D \to K^0_S\pi^+\pi^-$ and $K^0_S K^+K^-$*, JHEP **06** (2016) 131, arXiv:1604.01525.

[52] C. De Melis, *The CERN accelerator complex*, OPEN-PHO-ACCEL-2016-001.

[53] LHCb collaboration, R. Aaij *et al.*, *LHCb detector performance*, Int. J. Mod. Phys. **A30** (2015) 1530022, arXiv:1412.6352.

[54] LHCb collaboration, C. Elsässer, *$\bar{b}b$ production angle plots*, lhcb.web.cern.ch/lhcb/speakersbureau/html/bb_ProductionAngles.html.

[55] LHCb collaboration, A. A. Alves Jr. *et al.*, *The LHCb detector at the LHC*, JINST **3** (2008) S08005.

[56] LHCb collaboration, *LHCb reoptimized detector design and performance: Technical Design Report*, CERN-LHCC-2003-030, 2003.

[57] R. Aaij *et al.*, *Performance of the LHCb Vertex Locator*, JINST **9** (2014) P09007, arXiv:1405.7808.

[58] LHCb collaboration, R. Aaij *et al.*, *Measurement of the track reconstruction efficiency at LHCb*, JINST **10** (2015) P02007, arXiv:1408.1251.

[59] R. Frühwirth, *Application of Kalman filtering to track and vertex fitting*, Nucl. Instrum. Meth. **A262** (1987) 444 .

[60] LHCb RICH group, M. Adinolfi *et al.*, *Performance of the LHCb RICH detector at the LHC*, Eur. Phys. J. **C73** (2013) 2431, arXiv:1211.6759.

[61] LHCb RICH group, A. Papanestis and C. D'Ambrosio, *Performance of the LHCb RICH detectors during the LHC Run II*, Nucl. Instrum. Meth. **A876** (2017) 221, arXiv:1703.08152.

[62] LHCb HLT group, *Trigger schemes*, https://twiki.cern.ch/twiki/bin/view/LHCb/LHCbTriggerConferenceDiagramsPlots.

[63] V. V. Gligorov and M. Williams, *Efficient, reliable and fast high-level triggering using a bonsai boosted decision tree*, JINST **8** (2013) P02013, arXiv:1210.6861.

[64] T. Sjöstrand, S. Mrenna, and P. Skands, *A brief introduction to PYTHIA 8.1*, Comput. Phys. Commun. **178** (2008) 852, arXiv:0710.3820.

[65] I. Belyaev *et al.*, *Handling of the generation of primary events in Gauss, the LHCb simulation framework*, J. Phys. Conf. Ser. **331** (2011) 032047.

[66] D. J. Lange, *The EvtGen particle decay simulation package*, Nucl. Instrum. Meth. **A462** (2001) 152.

[67] P. Golonka and Z. Was, *PHOTOS Monte Carlo: A precision tool for QED corrections in Z and W decays*, Eur. Phys. J. **C45** (2006) 97, arXiv:hep-ph/0506026.

[68] Geant4 collaboration, J. Allison *et al.*, *Geant4 developments and applications*, IEEE Trans. Nucl. Sci. **53** (2006) 270; Geant4 collaboration, S. Agostinelli *et al.*, *Geant4: A simulation toolkit*, Nucl. Instrum. Meth. **A506** (2003) 250.

[69] M. Clemencic *et al.*, *The LHCb simulation application, Gauss: Design, evolution and experience*, J. Phys. Conf. Ser. **331** (2011) 032023.

[70] W. D. Hulsbergen, *Decay chain fitting with a Kalman filter*, Nucl. Instrum. Meth. **A552** (2005) , arXiv:physics/0503191.

[71] Particle Data Group, M. Tanabashi *et al.*, *Review of particle physics*, Phys. Rev. **D98** (2018) 030001.

[72] LHCb collaboration, R. Aaij *et al.*, *Measurement of CP observables in $B^\pm \to DK^\pm$ and $B^\pm \to D\pi^\pm$ with two- and four-body D decays*, Phys. Lett. **B760** (2016) 117, arXiv:1603.08993.

[73] G. A. Cowan, D. C. Craik, and M. D. Needham, *RapidSim: An application for the fast simulation of heavy-quark hadron decays*, Comput. Phys. Commun. **214** (2017) , arXiv:1612.07489.

[74] LHCb collaboration, R. Aaij *et al.*, *Study of $B^- \to DK^-\pi^+\pi^-$ and $B^- \to D\pi^-\pi^+\pi^-$ decays and determination of the CKM angle γ*, Phys. Rev. **D92** (2015) 112005, arXiv:1505.07044.

[75] A. Rogozhnikov, *Reweighting with boosted decision trees*, Journal of Physics: Conference Series **762** (2016) 012036.

[76] LHCb collaboration, R. Aaij *et al.*, *Measurement of B^0, B_s^0, B^+ and Λ_b^0 production asymmetries in 7 and 8* TeV *proton-proton collisions*, Phys. Lett. **B774** (2017) 139, arXiv:1703.08464.

[77] LHCb collaboration, R. Aaij *et al.*, *Measurement of CP asymmetry in $D^0 \to K^-K^+$ and $D^0 \to \pi^-\pi^+$ decays*, JHEP **07** (2014) 041, arXiv:1405.2797.

[78] S. S. Wilks, *The large-sample distribution of the likelihood ratio for testing composite hypotheses*, Ann. Math. Stat. **9** (1938) 60.

[79] LHCb collaboration, R. Aaij *et al.*, *Measurement of the CKM angle γ in $B^+ \to [K^0_S h^+ h^-]_D h'^{\pm}$ decays using the full Run 1 and Run 2 dataset*, in progress.

[80] LHCb Collaboration, R. Aaij *et al.*, *Physics case for an LHCb Upgrade II - Opportunities in flavour physics, and beyond, in the HL-LHC era*, Tech. Rep. LHCB-PUB-2018-009. LHCC-G-171, CERN, Geneva, 2018. ISBN 978-92-9083-494-6.

[81] LHCb collaboration, *LHCb Trigger and Online upgrade Technical Design Report*, Tech. Rep. CERN-LHCC-2014-016. LHCB-TDR-016, CERN, 2014.

[82] T. Gershon and A. Poluektov, *Double Dalitz plot analysis of the decay $B^0 \to DK^+\pi^-$, $D \to K^0_S\pi^+\pi^-$*, Phys. Rev. **D81** (2010) 014025, arXiv:0910.5437.